MAPPING THE RECEPTIVE FIELD STRUCTURE AND FUNCTIONAL CONNECTIVITY OF GENETICALLY IDENTIFIED AMACRINE CELLS IN MOUSE RETINA

Joseph A. Leffler

A DISSERTATION

Presented to the Neuroscience Graduate Program
Vollum Institute
Oregon Health & Science University
School of Medicine
In Partial Fulfillment of
the Requirements for the Degree of

Doctor of Philosophy

August 2021

Advisor, William Rowland Taylor, PhD

Member & Chair, Kevin Wright, PhD

Member, Henrique von Gersdorff, PhD

Member, Tianyi Mao, PhD

Member, Benjamin Sivyer, PhD

TABLE OF CONTENTS

List of Figures

List of Abbreviations

AC	amacrine cell
ACET	(*S*)-1-(2-Amino-2-carboxyethyl)-3-(2-carboxy-5-phenylthiophene-3-yl-methyl)-5-methylpyrimidine-2,4-dione
AMPA	α-amino-3-hydroxy-5- methyl-4-isoxazolepropionic acid
BC	bipolar cell
ChAT	choline acetyl transferase
ChR2	Channnelrhodopsin
CRH	corticotropin releasing hormone
D-AP5	D-(-)-2-amino-5-phophonopentanoic acid
DEGs	differentially expressed genes
DREADD	designer receptors exclusively activated by designer drugs
DSGC	direction selective ganglion cell
EPSC	excitatory postsynaptic current
FACS	fluorescence activated cell sorting
GABA	gamma-aminobutyric acid
Gbx2	gastrulation brain homeobox 2
GC	ganglion cell
GCaMP	genetically encoded calcium indicator
GCL	ganglion cell layer
GFP	green fluorescent protein
GlyT	Glycine transporter
GPCR	G-protein coupled receptor
GYKI	(1-(4-aminophenyl)-3-methylcarbamyl-4-methyl-3,4-dihydro-7,8- methylenedioxy-5H-2,3- benzodiazepine hydrochloride
HBSS	Hank's Balanced Salt Solution
HC	horizontal cell
I-V	Current-Voltage
iGluSnFR	intensity-based glutamate sensing fluorescent reporter
INL	Inner nuclear layer
IPL	Inner plexiform layer
IPSC	Inhibitory postsynaptic current
IRES	Internal ribosome entry site
L-AP4	LL-2-amino-4-phosphonobutyric acid
LMD	local motion detector
MFA	meclofenamic acid
mGluR6	Metabotropic glutamate receptor type 6
NaV	Voltage gated sodium channel
nGnG	non-GABAergic non-Glycinergic
NMDA	N-methyl-D-aspartate
nNOS	neuronal nitric oxide synthase
NO	nitric oxide
OMS	object motion sensitive
ONL	outer nuclear layer
OPL	outer plexiform layer
PBS	phosphate buffered saline
PFA	paraformaldehyde
PSP	postsynaptic potential
PSTH	peristimulus time histogram
SAC	starburst amacrine cell
scRNAseq	single cell RNA sequencing
SR	6-imino-3-(4- methoxyphenyl)-1(6H)- pyridazinebutanoic acid hydrobromide
Tac1	Tachykinin1
tdT	td-Tomato
TH	tyrosine hydroxylase
TPMPA	(1,2,5,6-tetrahydropyridin-4-yl)methylphosphinic acid
vGlut3	vesicular glutamate transporter type 3
WFAC	wide field amacrine cell
YFP	yellow fluorescent protein

Acknowledgements

This dissertation was only possible because of the help I received from the many brilliant researchers I have worked with in the Taylor and Puthussery labs at both OHSU and at UC Berkeley. I would like thank them all for their support, advice, and patience. Dr. W. Rowland Taylor has been a great mentor to me, and communicates with the right mix of sarcasm and genuine enthusiasm. I always leave his office with a renewed sense of excitement about my work. His encouragement combined with Dr. Teresa Puthussery's has generated a wonderful collaborative space. Seeing them build a lab at UC Berkeley and create a new scientific community just as supportive as the one I joined in the basement of the Casey Eye Institute, but with windows, has been a great pleasure.

When I first joined the lab, Ben Murphy-Baum, Todd Stincic, and Kumiko Percival all spent countless hours helping me get my footing and made lab somewhere I wanted want to come to every morning. Ben Sivyer was always willing to spend extra time to push my critical thinking and help me approach my research from all angles. I am incredibly grateful for the patience they showed me. Thank you to Manoj Kulkarni and Amanda McLaughlin. You made the new lab in Minor Hall feel like home. Also, thank you Jacqueline Gayet, for flying back and forth from Portland to Berkeley to keep our lab running and for being the glue that keeps our lab together.

Moving to UC Berkeley was a difficult transition, and the success I found there is a direct result of the help and encouragement I received from my dissertation committee, Dr. Kevin Wright, Dr. Henrique von Gersdorff, Dr. Tianyi Mao, and Dr. Ben Sivyer. They guided me through the transition to a new institution, always providing excellent advice and scientific expertise on my continuing education. I want to thank my collaborators in the Wright lab, my

NGP classmates, and all the core facility staff who have helped me along the way at OHSU and at UC Berkeley. I would also like to thank Dr. Chinfei Chen, for giving me my first chance to study the visual system as research assistant in her lab and for providing such a powerful example of what hard work and creativity can accomplish in academia.

Thank you to my parents and siblings, for providing a foundation of love and support on which to build my scientific career. The value placed on academics growing up continues to serve me well. Thank you to my partner, April Long, for turning everywhere we move into a home and for supporting me throughout this journey, making it far more joyful and vibrant than I could have hoped. Thank you for surprising me with our wonderful dog Ula, whose wagging tail has kept me going through this journey of a PhD almost as much as she has. Mostly, thank you for showing me what truly working hard for others looks like. Academia feel insular at times. Your passion for helping others provides the perspective I need to realize work should be for others.

Abstract

Of the over 100 types of retinal neurons, amacrine cells account for 60 types representing the bulk of this diversity, with each of the roughly 60 types receiving a different set of inputs synapsing with a different specific set of outputs. While overarching principles of how these interneurons are functioning is known, specifics as to what an individual amacrine cell (AC) type responds to in the visual scene and what cohort of presynaptic mechanisms create this selectivity are largely unknown. Much remains to be uncovered about the precise mechanisms of action for individual types. In this thesis I studied several types of genetically identified ACs that would otherwise be seldom encountered without a pre-labeling approach. This includes two AC types that can be selectively labeled due to their unique expression of the transcription factor for Gastrulation Brain Homeobox 2 (Gbx2). One is a S3 laminating Gbx2+ AC, which had been previously uncharacterized, and the other a S5 laminating Gbx2+ AC, which is likely an overlapping population with the previously characterized corticotropin releasing hormone (CRH) AC type 1. I have also studied two populations of ACs identified by their expression of neuronal nitric oxide synthase (nNOS): the S1-S5 bi-stratified, axon-bearing NOS1 cell, and the S3 laminating, non-spiking NOS2 AC. Additionally, I identified a novel connection between the NOS2 ACs and a functionally and structurally defined population of ganglion cells (GCs), the local motion detecting GCs.

In Chapter 1 I provide an introduction giving background on retinal circuitry, including the organization of broad categories of neuronal output, the diversity of AC types in mouse retina with a specific focus on the types studied in detail in later chapters, and background information and context on AC structure and function including motifs of inhibition both pre- and post-synaptically that generates AC receptive field structures. In Chapter 2 I present a study that reveals the synaptic inputs to NOS2 ACs and identifies a novel output from these cells to the local motion detecting ganglion cell circuit in mouse retina. This project focusses specifically on the role of NOS2 ACs in shaping the inhibitory suppression of local motion detector (LMD) GCs during global motion. In Chapter 3 I present a collaborative study that provides the first characterization of the Gbx2+ ACs. This project identifies the molecular and structural characteristics of these previously unidentified interneurons. It also characterizes the voltage responses of and synaptic inputs to Gbx2+ ACs which respond to the visual scene in distinct ways commensurate with their morphology. The Gbx2-S3 cell responds transiently to both increases and decreases in contrast, receives potent lateral inhibition, and shows extensive gap junction coupling to bipolar cells (BCs) that may mediate its output. S5-laminating Gbx2+ ACs respond with sustained depolarization to increases in contrast, are hyperpolarized by decreases in contrast, and receive weak lateral inhibition. Mechanisms that shape the receptive field structure of either AC type, particularly with regard to lateral GABAergic inhibition, are examined.

Chapter 1: Introduction

The retina is an ideal model system for circuit-level analysis

A major challenge in neuroscience is to understand how individual neurons, the building blocks of the nervous system, can communicate with one another to create meaningful information as a circuit. As noted by Ramón y Cajal in 1893, "The retina is an advantageous structure for the neurobiologist because of its accessibility, its orderly organization in alternate layers of cell bodies and intercellular contacts and the easy identification of the main direction of the nervous message flow." (Ramón y Cajal in *La Retine des Vertebres, 1893)***.** It remains an ideal neural system to study how circuits with only three layers of neurons are capable of complex signal computations. Additionally, the intact retina can be isolated from the rest of the eye and brain, allowing similar advantages to *in vivo* preparations—responses to its natural stimuli, no severing of endogenous connections—with the same cellular level precision as i*n vitro* studies—stably recording from individual neurons and pharmacological access.

Additionally, the retina has the advantage for researchers of being naturally transparent, which it must be to allow light to reach photoreceptors unimpeded. Central circuits are resistant to optical imaging due to their opacity caused by lipids, particularly in myelinated axons. These are largely absent in the retina, which allows researchers to more easily image fluorescent dyes including calcium or voltage indicators throughout the tissue. Given these advantages, and with recent technological advancements in cell-type specific targeting through transcriptional identification, we can sort through the many complex cell types in the retina and begin to understand how individual subtypes are contributing to circuit function both in their role in vision, and as a model system for central circuits. The rest of this introduction will be spent addressing the organization of retinal circuits, focusing specifically on key mechanisms that the amacrine cells studied in this thesis use to shape retinal output.

Neuronal organization of the retina

Visible light enters the eye and traverses the retina, at which point it is detected and converted into an electrochemical signal by photoreceptors. That signal is then processed by around 100 distinct types of neurons before it is relayed to retino-recipient central circuits in higher brain centers (Masland 2001; Wassle 2004; Macosko et al., 2015, Sanes and Masland, 2015, Shekhar et al. 2016, Tran et al., 2019; Yan et al. 2020)**.** The major classes of neuron types in the retina are informed by their organization of two synaptic regions, called plexiform layers, between three nuclear layers. The outer of which, the ONL, is positioned up against the sclera and is comprised of rod and cone photoreceptor cell bodies while the inner nuclear layer (INL) holds the somas of bipolar, amacrine, and horizontal cells. The ganglion cell layer (GCL), which is positioned more centrally in the eye towards the vitreous, contains a mixture of ACs and GCs. This layered structure supports a vertical excitatory pathway from photoreceptors to bipolar cells and then to ganglion cells, the axons of which provide output to central circuits by way of the optic nerve. The terminals of photoreceptors synapse on the dendrites of bipolar cells in the outer plexiform layer (OPL), and the terminals of bipolar cells synapse on the dendrites of amacrine and ganglion cells in the inner plexiform layer (IPL). Horizontal cells (HCs) which stratify in the OPL provide feedback inhibition to photoreceptor terminals and act as a gain control at this first synapse.

ACs which stratify in the IPL perform many functions, but largely are responsible for decorrelating signals from bipolar cell terminals by providing inhibition, as well as electrical (gap junction mediated) or recently discovered chemical (glutamatergic) excitation to bipolar cell terminals, the dendrites of ganglion cells, or even other amacrine cells (Sun et al., 2013; Morrie & Feller, 2018; Soto et al., 2019; Grimes et al., 2011; Lee et al., 2014). Before describing these inhibitory and excitatory motifs in more detail, let us briefly step back to look at the initial transformation of photons to an electrical signal in photoreceptors. The transduction of visible light into an electrical signal begins in the outer segments of rods and cones where membrane disks containing thousands of opsin molecules—photosensitive G-protein coupled receptors (GPCRs) in which photons act as the ligand for a covalently-bound chromophore within the GPCR that undergoes a conformational change from 11-cis-retinal, to all-trans-retinal initiates a

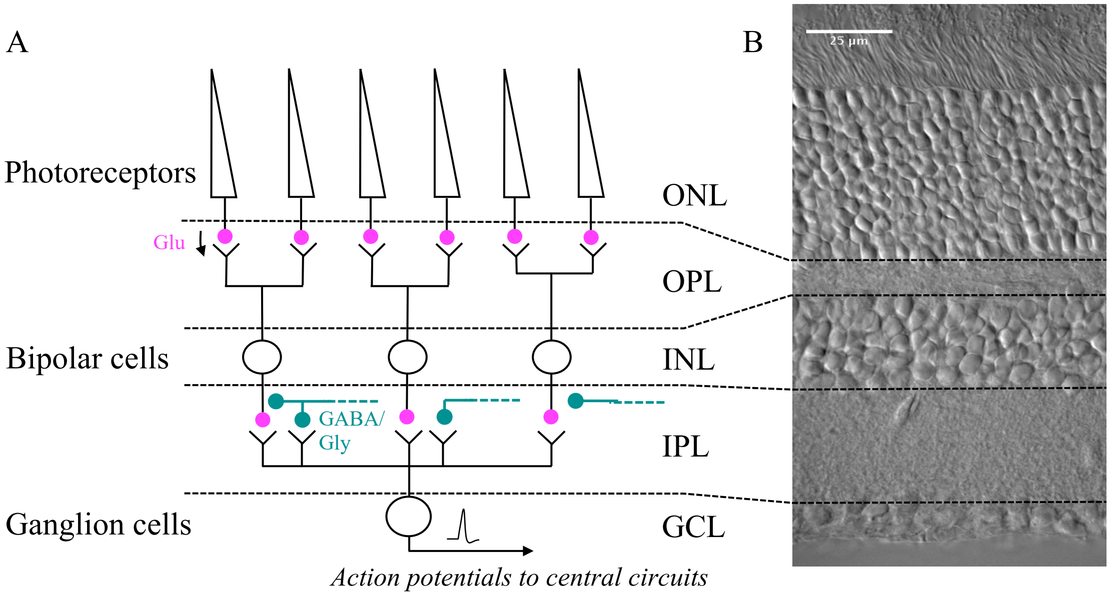

FIGURE 1.1 Genetic labeling strategy and morphological identification of NOS+ ACs and LMD GCs

Light is converted into an electrical signal in photoreceptors, which relay that signal to bipolar cells, and finally to ganglion cells via changes in glutamate (Glu) release. Glutamatergic synapses are shown in magenta. In the mouse retina, ganglion cells pool inputs from multiple bipolar cells, which combine inputs from many photoreceptors. Using the neurotransmitters GABA or glycine (Gly), amacrine cells inhibit the retinal circuit at various synaptic locations (bipolar cell axon terminals and ganglion cell dendrites). GABA/glycinergic synapses are shown in teal. Amacrine cells can also inhibit other amacrine cells (not shown). Amacrine cell somas and presynaptic circuits are not shown. For clarity, horizontal cell circuits are not shown. B. Z-projected confocal image stack from transmitted light pathway showing laminar structure of mouse retina. ONL-outer nuclear layer, OPL-outer plexiform layer, INL-inner nuclear layer, IPL-inner plexiform layer, GCL-ganglion cell layer.

signaling cascade leading to the hyperpolarization of the rod or cone, and subsequent reduction in glutamate release from its terminal.

Rods are exquisitely sensitive to light and are able to decrease glutamate release after the detection of a single photon. (Schneeweis and Schnapf, 2000, Sharpe et al. 1989). To achieve this sensitivity, they have incredibly densely packaged rod-opsin (rhodopsin) molecules with around 100 million per rod, and act as a photomultiplier tube, increasing the chances of a photon successfully encountering a molecule of 11-cis-retinal by dense packaging in ~1000 membrane disks per rod. While the conversion from 11-cis- to all trans-retinal occurs in the microsecond range, replenishing 11-cis-retinal is much slower and enzymatically contingent, leading to rapid sensitization of the rod system at moderate light intensities. At brighter light intensities, cone photoreceptors largely take over transduction. They are far less sensitive to low numbers of photons, but can signal over a wider range of intensities far beyond the saturation point of rods. Both photoreceptor types rely on graded glutamate release from highly specialized ribbon synapses which allow a steady supply of glutamate vesicles for a nearly constant release of neurotransmitter in their resting state prior to hyperpolarization by light (von Gersdorff and Matthews 1997; Jackman et al. 2009).

Glutamate from photoreceptors is released onto bipolar cell terminals where it is either excitatory via sign-conserving ionotropic receptors, or inhibitory through a sign inverting metabotropic glutamate receptor (mGluR6) coupled to the TRPM1 cation channel. (Werblin and Dowling, 1969; Kaneko, 1970; Koike et al., 2010; Morgans et al., 2009, 2010). Previous to this however, glutamate from photoreceptors is excitatory to horizontal cells, which then inhibit photoreceptors, providing a negative feedback element regulating glutamate release. Bipolar cells also release glutamate, driving excitation of both postsynaptic ganglion and amacrine cells.

It is the task of amacrine cells through graded release of GABA or glycine, or through action potential mediated release of neurotransmitters, to inhibit specific cell types, shaping the responses of 30-40 distinct types of retinal GCs which provide feature specific parallel pathways to the brain encoding different aspects of the visual scene.

Feature Selectivity and GC type overview

A major operation accomplished by the retina is to separate largely homogenous photoreceptor output into the 30-40 separate output pathways represented by individual GC types. The definition of an individual GC type used in this thesis, and in much of retinal literature, relies on a combination of elements. Cells of the same type will have shared intrinsic functional properties—similar receptor expression and ion channel composition. They will have similar morphology, in their soma size and dendritic stratification laterally—how much of the retinal surface its arbor covers—and vertically—at what depth in the IPL those dendrites stratify. They will also receive similar synaptic inputs from a particular cohort of excitatory and inhibitory bipolar and amacrine cells. Lastly, for image-forming cells (those that are signaling about the visual scene and not about general luminance levels or other non-image forming components) will cover the entire surface area of the retina with minimal overlap in dendritic arbors. This has some variability depending on cell type, where some GCs have a higher density or higher overlap in particular quadrants or hemispheres, or higher overlap in general (DeVries and Baylor, 1997; Rockhill et al., 2000).

How a distinct output channel represented by an individual GC type achieves specificity to a particular visual scene element largely arises at the level of the inner plexiform. It is here where the specific set of bipolar and amacrine cell inputs combine with the cell intrinsic properties of that GC to generate a unique set of responses optimally tuned to certain elements in the visual scene. This feature selectivity can be quite narrowly tuned in a particular dimension of the visual scene. Take for example, the ON-OFF direction selective GCs (ooDSGCs), which have been studied extensively in mouse and rabbit retina (Yoshida et al., 2001; Briggman et al., 2011; Hoggarth et al., 2015; Huang et al., 2019; Barlow and Levick 1964; Taylor and Vaney 2002; Fried et al., 2002; Vaney et al., 2012). They respond to both increases and decreases in contrast, each type preferring a particular direction of motion, remaining largely silent during the opposite direction of motion. These cells, while selective for direction of motion, may show more broad tuning in other aspects of the visual scene like contrast and speed tuning (Rosa et al., 2015; Ravello et al., 2019). The exact combination of preferred and non-preferred stimuli that build the receptive field of a light-responsive cell leads to a functional identity of its particular type. In the case of the DSGCs preferential inhibition from a particular set of inhibitory amacrine cells, in this case, the starburst amacrine cells (SACs), form more synapses on the non-preferred direction of motion side of the DSGC such that excitation from bipolar cells is cancelled out when objects move in the null direction, but are not suppressed during preferred direction of motion. (Figure 1.2)

Pre- and postsynaptic inhibition

The above example of ooDSGCs by no means represents the full extent of the literature on direction selectivity, but it highlights a key mechanism ACs leverage to help generate feature selectivity in GCs. ACs can preferentially form synapses directly with dendrites of a certain individual or small cohort of GC types. This postsynaptic inhibition creates a negative filter that subtracts some element of the visual scene that a particular AC prefers. In the case of SACs, their own feature selectivity is to objects moving in a centrifugal manner (center out) relative to the SAC soma, and they are weakly activated by centripetal motion (distal to central) relative to the soma. The mechanism by which centrifugal preference is generated is still a matter of active study, but centrifugal motion combined with the synapse specificity onto the null side of ooDSGCs is thought to generate the specific output of this cell type (Wei, 2018).

While it is useful to use the SAC-DSGC circuit as a model to describe feature selectivity generation in the retina, for most GC types the exact mechanism of feature selectivity generation is unknown. We can, however, take the ooDSGCs as a model to help identify a key feature of AC function that is a common motif across other GC circuits. The above mechanism is one of postsynaptic inhibition and is thought to generate specific blind-spots, or inhibitory regions within a particular GC receptive field under certain contexts. The postsynaptic nature of this signal means it can be highly selective, in the case of the SAC-DSGC connection, it is eclusive to ooDSGCs. A postsynaptic inhibitory mechanism is the motif identified in Chapter 2 of this

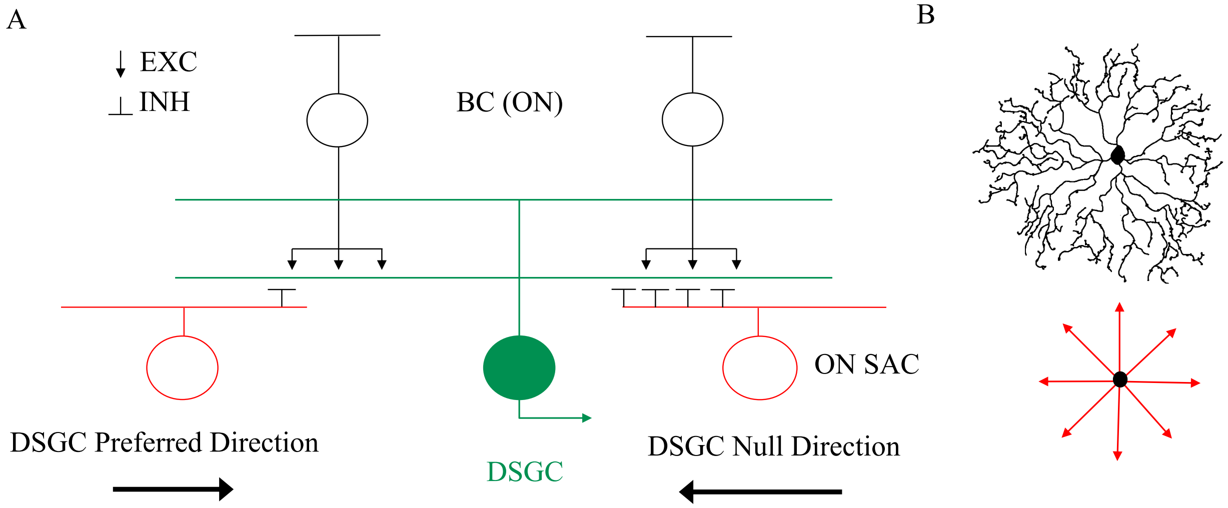

FIGURE 1.2 Illustration of SAC-DSGC postsynaptic inhibition

A. Cross-section of the direction selective circuit. Only inputs to DSGCs from the On layer are illustrated for simplicity. Off layer inputs are generally thought to be mirror images of On pathway inputs. DSGCs receive excitatory inputs (↓) from bipolar cells and inhibitory inputs (⊥) from SACs. SACs on the null side form stronger inhibitory connections than SACs on the preferred side. B. (top) Outline of SAC arbor, top view. (lower) Centrifugal motion preference illustration. SAC processes respond with greater depolarization to centrifugal motion, which when combined with preferential inhibition on the DSGC null side, generating direction selectivity.

thesis regarding NOS2 wide-field amacrine cells that were found to provide inhibition to a specific subset of GCs that show a preference for local over global motion.

Conversely, inhibition can be far less specific when it occurs one synapse upstream of GC dendrites. Pre-synaptic inhibition of BC axon terminals is a way to distribute a signal from a particular AC to a wider range of output neurons. It still generates a negative filter, as with the SAC-DSGC circuit, but in a more distributed manner in which a particular AC receptive field structure can be propagated to any number of output channels, so long as the BC type that is inhibited by the AC in question, is providing excitation to a given GC. Additionally, the net inhibition a particular GC receives will be a result of the combination of the receptive field structures of each presynaptic and postsynaptic inhibitory source that GC receives. The bipolar cell inputs will have been filtered by their intrinsic membrane properties as well as the presynaptic inhibition they receive.

To highlight and define a functional role of presynaptic inhibition from an AC to a BC, let's look at a well-studied AC in the retina, the AII cell. The AII AC, originally identified by Kolb and Famiglietti in 1974, among other roles, is a key interneuron in coupling the scotopic (low light) pathway onto the photopic (high background light) mediated pathway. One way it does this, is by receiving excitatory glutamatergic input from rod-BCs in the ON sublamina of the IPL, and then providing glycinergic inhibitory input to OFF cone-BCs in the OFF sublamina of the IPL. This allows rod-driven signals to cross over from ON sublamina—where light increments depolarize and light decrements hyperpolarize rod-BCs–to OFF sublamina in a sign inverting glycinergic synapse. The AII AC has been shown to synapse with a range of OFF cone-BCs, distributing this low-light ON signal to any number of OFF-responsive ganglion cells, so long as they receive input from the subset of OFF cone-BCs that are inhibited by AII ACs[*] (McGuire et al., 1984; van Wyk et al., 2009; Tsukamoto and Omi 2017; Graydon et al., 2018; McLaughlin, et al., 2021).

Gap-junction mediated transmission

In addition to crossover glycinergic inhibition from rod-BCs to some OFF cone-BCs, AII ACs contribute to a signal transduction that is atypical of the dogmatic idea that ACs are only inhibitory. AII ACs drive excitation in the ON pathway from rod-BCs to ON cone BCs through gap-junction mediated transmission at their distal dendrites in the ON sublamina of the IPL. In this way, AII ACs serve to couple a single photoreceptor type, rods, to both the ON and OFF cone-BCs by way of the intermediary rod-BC. Similar to the glycinergic transmission from their OFF lamina lobular appendages, though in the opposite polarity, AII ACs distribute their input from the rod pathway to multiple ON cone-BCs[†] (Tsukamoto and Omi 2017).

Gap junction mediated transmission poses a complicated question in terms of signal specificity in the retina. The example of the AII to ON cone-BC connection highlights the fact that electrical transmission at gap junctions can be bi-directional. Under photopic conditions where cones provide input to cone-BCs, ON cone BCs are able to activate AII ACs through the

---

[*] The AII-AC also has been shown o provide glycinergic input to different cohorts of BC types in different species. In mouse there is a strong preference for cone BP type 2, though other connections exist. In cat, type a1 and a4, but not a2 and a3 receive glycinergic inhibition. In primate, FMB and DB1 BCs receive glycinergic inhibition. Additionally, AII ACs make direct glycinergic inputs to the dendrites of a few OFF GC types (Manookin et al., 2008, Murphy and Rieke, 2008).

[†] Similar to chemical synapses with OFF cone BCs, gap-j synapses with ON cone BCs differ among species (Demb and Singer, 2012). Additionally AII ACs are homotypically coupled to a network of other AII ACs, which is modulated by DA under different background conditions (Veruki and Hartveit 2002).

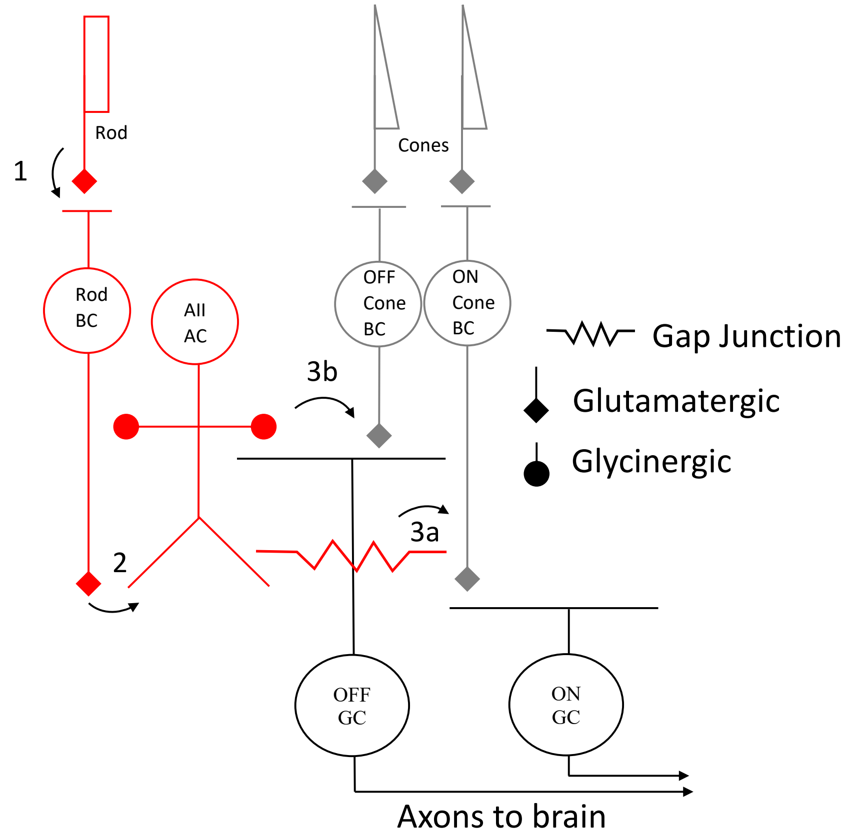

FIGURE 1.3 Illustration of AII AC circuit

(1) Rods provide input to Rod-BCs. (2) Rod-BCs provide input to AII ACs. (3a) AII ACs provide gap-junction mediated input to ON Cone BCs and (3b) Glycinergic inhibition to OFF Cone BCs. Many circuit elements have been left out, like Rod-Cone gap junctions, AII-AII gap junctions, feedback inhibition from A17 ACs to AII ACs as well as inhibitory input from AII ACs directly to OFF GCs. Red outlines represent the rod pathway. Gray outlines show cone pathways. Notice how the rod pathway piggybacks onto the existing cone system.

same gap junctions that in scotopic conditions drive signal flow in the opposite direction (Szikra et al., 2014; Tikidji-Hamburyan et al., 2017**).** Many AC cell types, as well as horizontal cells have been shown to be gap junction coupled either homotypically—to cells of the same type—or heterotypically—to other cell types. The functional relevance of these gap junctions remains largely unexplored, and presents a wide range of possibilities as to what role ACs may have apart from their traditional GABAergic or glycinergic inhibitory mechanisms (Kenyon and Marshak 1998, Bloomfield and Völgyi 2009; Hu and Bloomfield 2003; Roy et al., 2017). One potential role of gap junction mediated transmission is proposed in Chapter 3 of this thesis regarding S3-laminating Gbx2+ ACs. We found that a gap junction permeable dye (neurobiotin) spread from these S3 cells into many bipolar cells, but did so with the spatial pattern of never extending into the distal third of the S3 cell's dendritic arbor, raising the possibility that the specific population of bipolar cells providing glutamatergic input to the S3-Gbx2+ AC may be propagated in a narrow spatial manner to peri-somatic bipolar cells of the same, or different types, but in the same polarity as the input to the AC, suggesting S3-Gbx2+ ACs may be excitatory.

Amacrine cell roles in feature selectivity

ACs represent the most diverse cell type in the retina. Morphology alone predicts there are at least 40 subtypes, and a recent set of heroic single cell transcriptomic studies could separate over 60 individual AC types through transcriptional identifying factors alone. If we consider the task of ACs as largely that of distinguishing one GC type's responses from another, then this abundance of ACs is expected. As will be discussed in this dissertation, individual AC types work in concert with excitatory bipolar cells and other AC types to craft a GC's specific feature selectivity. While the above two examples of AII AC to cone-BC and SAC to DSGC are well studied connections, the bulk of the remaining roles of ACs in shaping GC feature selectivity remains obscure. The remainder of this introduction will be spent identifying some of the known mechanisms ACs leverage to generate different aspects of GC output specificity. This will help us understand what tools ACs at their disposal to shape the signal being sent to central circuits, and to place the findings of the remainder of this dissertation in a broader context.

Center-surround antagonism

Center-surround antagonism is commonly found in neural circuits, particularly in sensory systems. This is thought to be due to its ability to permit more accurate discrimination of sensory information (Bastian et al., 2002; Hubel and Wiesel, 1962; Knudsen and Konishi, 1978; Yokoi et al., 1995). In the visual system in particular, center-surround organization is observed at many levels of information processing. Visual cortex and thalamus as well as multiple levels within the retina itself all use this key mechanism to enhance edge detection as well as establish color opponent vision (Dacey, 1999; Marr and Hilderth, 1980; Usrey and Alitto, 2015). In its simplest form from the perspective of an ON preferring cell, ON-center cells depolarize to light increases in the center of their receptive field, but are inhibited by light increases in their surround. In the retina this organization occurs both in the inner and outer regions. In the OPL, HCs feed back onto cone terminals impacting their depolarization or hyperpolarization in the opposite direction when the surrounding region of that cone is activated. This generates an initial center-surround structure at the first synapse in the retina and this signal is inherited by downstream neurons (BCs, ACs, GCs) and is then fine-tuned in the inner retina. If this were the only component of center-surround antagonism in the retina, all GCs would have similarly tuned spatial receptive fields. However, this is far from the case. There is a wide range in the spatial output properties of GCs, ranging from more simplistic concentric center-surround structures to more complex orientation-tuned GCs and other highly asymmetric GC responses. The context under which these inner retinal circuits are activated can determine the degree and extent to which center-surround antagonism ultimately impacts a GC's output. The specific tuning of these inner retinal components are in large part due to the cell types that provide lateral inhibition. A major group that is well suited for generating spatially complex receptive field features are the under-studied wide-field ACs (WFACs).

Axon bearing and axon-less ACs

The lack of understanding for how individual WFACs impact the receptive field structure of GCs is in large part due to how neurons that detect elements of the visual scene tile the surface of the retina. A cell with a larger receptive field will require far fewer total neurons to cover the surface area of the retina than their smaller narrow or medium field counterparts. This makes repeatedly finding the same type of WFAC by chance less likely. To get around this difficulty, we used genetic labeling to target nNOS+ ACs in Chapter 2, which had been shown to label just two populations of neurons, both of which fall under the wide-field category. Cells like these are well suited to establish fine-tuned complex spatial receptive field structures through surround antagonism based on their wide-field morphology. In the case of NOS+ ACs, each is able to receive information over a wide region and through GABAergic transmission, inhibit specific postsynaptic partners. NOS1 ACs fire action potentials which mediate GABA release, while NOS2 ACs release GABA in a graded fashion, with stronger depolarization leading to more neurotransmitter release (Park et al., 2020, Jacoby and Schwartz 2018). Morphologically WFACs fall into two categories, those with separate axonal and dendritic fields, the poly-axonal cells, and those with exclusively dendritic processes. The original nomenclature for amacrine cell originates from the Greek for not *(a)* long (*makrós*) meaning a cell without long processes, as a way to distinguish amacrine cells from projection neurons like GCs which have long axons reaching to central regions. However, the axon bearing poly-axonal amacrine cells have the property of being able to spike, allowing them to receive information over their dendritic field, which is usually a narrower region than their axonal arbor, which can project across the full width of the retina with high signal fidelity. This organization allows them the ability to distribute local signals, potentially about motion in one region of the visual field, to many distal targets along their axonal, or projective field, subtracting that local signal from global regions. However, cell specific examples of this function have been difficult to demonstrate given the complexity of studying an individual WFAC's role in a particular circuit (de Vries et al., 2011).

Exclusively dendritic WFACs—those lacking an axon—provide an intriguing model cell to study how an individual neuron can have functionally isolated inputs and outputs across its neurites. How can a single WFAC act in different manners at different locations along its dendritic arbor? One well-studied example of an axon-less AC are SACs that have been found to receive bipolar cell input along the entirety of their dendritic arbor, but release GABA only from the distal third of their arbor. How this functional division arises is still an open question, but demonstrates a degree of functional separation along a single dendritic arbor. Other cells may similarly have independent regions serving different functions, as has recently been shown for the atypical vGlut3+ AC, which releases glycine under certain contexts onto specific GCs, and releases glutamate onto other GCs under other circumstances (Park et al., 2018). An extreme example of this multiplexing within a single cell exists in the A17 AC, which provides reciprocal GABAergic feedback at the rod-BC to AII synapse, which has been shown to function in an electrically isolated manner in which one A17 AC can multiplex at hundreds of separate rod-BC to AII synapses without the activity at one dendritic terminal impacting a neighboring region on the same A17 AC (Grimes et al., 2010).

Object motion sensitivity

WFACs have the potential to generate complex negative spatial filters in downstream GCs based on their far-reaching axonal arbors. An example of this in their proposed role in generating orientation tuning by providing inhibition preferentially along their own elongated axis which generates an oppositely tuned orientation preference in the connected postsynaptic GC (Murphy-Baum and Taylor, 2015). In simpler terms, a wide-field cell has the potential to subtract global information from a smaller postsynaptic GC, helping to restrict its responses during global stimuli. This is of particular importance with regard to object motion sensitivity, which we show in Chapter 2 is partially originating from NOS2 AC inhibition of ganglion cells that show preference for local motion, the LMD GCs.

Retinal literature on the subject of object motion sensitivity demonstrates a key concept in understanding AC function. The literature on this feature-detecting circuit has identified several AC types that contribute to these object motion sensitive (OMS) GCs in distinct and partially overlapping ways. OMS GCs were first described in salamander and rabbit retina when a subset of ganglion cells were identified that fired robust trains of action potentials when objects moved over the receptive field of that cell, but when the surrounding area also moved in the same direction, these cells were silent (Barlow et al., 1964, van Wyk et al., 2006, Olveczky et al., 2003, 2007, Baccus et al., 2008). This is thought to signal evolutionarily salient features like predator movement against a static or moving background. More recently, in 2012, in the BAC transgenic mouse line TYW3, a subset of labeled cells—the W3 cells—were found to also be sensitive to small objects moving on a static background (Zhang et al., 2012) that may represent a comparable population in mammalian retina. That study found that blocking voltage gated sodium channels (Na_V) which blocked the activity of poly-axonal WFACs reduced local motion preference significantly. The salamander studies by Olveczky and colleagues used visual stimuli that alternated motion in the center alone (local motion), in the center and surround coherently (global motion), and in the center and surround in different directions (differential motion), studying the underlying excitatory and inhibitory mechanisms that led to the observed preference for local and differential motion as well as the lack of responses during global motion. They found multiple mechanisms including both pre and postsynaptic inhibition as well as spike dependent and spike independent mechanism. This highlights the convergence of AC inputs each providing some of the pre and postsynaptic inhibition responsible for generating OMS.

Recent advances in mouse genetics have allowed identification of some of these AC inputs to OMS GCs. These new studies have in some ways clarified and in other ways further obscured the mechanisms behind OMS. An anatomical study in 2014 by Brüggen et al found synaptic contacts between a tyrosine hydroxylase (TH)::green fluorescent protein (GFP) positive GABAergic WFACs and the W3 in a BAC transgenic line (Brüggen et al., 2014). A following study conditionally rendered these TH+ ACs unable to package GABA in vesicles and observed a significant reduction in inhibitory input to W3 GCs, demonstrating weaker motion preference for small moving objects against a static background (Kim et al., 2017). TH+ cells were shown to respond with longer latency to small objects than global ones, suggesting a kinetic mechanism generating their own preference for global motion, but differential motion preference is still unclear in TH+ ACs and W3 GCs. Furthermore, a detailed study examining the functional heterogeneity in similar morphological cell types, dubbed "high-definition" GCs, that may be grouped under the W3 GC penumbra, found up to four different cell types with various responses to local, global, and differential motion (Jacoby and Schwartz, 2018). This highlights some of the difficulties of using a single factor (anatomy, function, or genetics) to identify a cell type. What was clear from the high-definition GC study is that the generation of motion sensitivity may be the net result of multiple inhibitory and excitatory mechanisms and different cell types may display OMS under different circumstances (at different contrasts, speed of motion etc.)

One of the surprising findings in the pursuit of OMS generating mechanisms was establishing the role of an atypical AC, the vGlut3+ AC, which had been shown to release glutamate in some strata of the IPL, and glycine at other strata (Lee et al., 2014; Tien et al., 2016; Tien et al., 2017). A facile chemo-genetic ablation study was done to remove vGlut3 cells conditionally with diphtheria toxin, in which the diphtheria toxin receptor is only expressed in vGlut3+ ACs, leading to reduced OMS in W3 GCs. (Kim et al., 2020) All together the OMS literature leads to an overarching picture showing multiple ACs leveraging different mechanisms to generate a highly restrictive feature selective response in OMS GCs. Considering the evolutionary advantage in being able to detect aerial predators, the high degree of selectivity and restrictive nature of multiple tiers of inhibitory and excitatory mechanisms may not be unexpected. However, that convergence of inputs also leaves room for further study of the participating cell types, and in the example of the NOS2 ACs studied in Chapter 2, demonstrates how additional cell types may be participating in object motion sensitivity under specific motion contexts.

Co-transmission and neuropeptides

As was mentioned in the example of the vGlut3 ACs, which release glutamate and glycine to distinct output cells, ACs tend to run counter to Dale's principle. Dale's principle states that a given neuron contains and releases only one neurotransmitter and exerts the same functional effects at all of its termination sites (Eccles et al., 1954). This may be the case in many central circuits, though exceptions do exist, particularly in the retina. One of the benefits of working in model neural circuits like the retina, is that it allows precise control over many cell types and can reveal details that may otherwise be missed when studying more difficult to access brain regions. The single cell transcriptomic study that established over 60 clusters of distinct AC types found almost all had at least one secondary, and sometimes a tertiary neurotransmitter or neuropeptide present at the transcriptional level (Macosko et al., 2015, Yan et al., 2020). It remains true that most ACs release either GABA or glycine, but the exceptions to Dale's principle show it is far from universal and cannot be assumed, particularly for retinal interneurons. Even the two Gbx2+ ACs studied in Chapter 3, one of which was shown to express neither GABA nor glycine, were revealed to express genes that encode neuropeptides. S3 laminating Gbx2+ cells expressed *Tachykinin1* (*Tac1*) and S5 laminating cells expressed corticotrophin releasing hormone (CRH). As the genetic marker suggests, NOS+ ACs also release nitric oxide (NO), whose role in AC responses to visual stimuli has only recently been studied.* It was found that 1-2 minute long visual stimuli of increasing intensity evoked NO release from NOS2 ACs. This freely diffusible gaseous neurotransmitter was shown to close gap junctions among the homotypically coupled NOS2 AC population, leading to an increase in membrane resistance under bright light conditions (Jacoby and Schwartz 2019).

Understanding the full capacity of an individual AC's function in visual processing will require updated definitions and a rethinking of prior ideas of what a cell type's possible mechanisms of action and functions may be. For example, the idea of an AC being solely inhibitory, or that ACs lack axons both should be rethought. As is the case in other model systems, what we can uncover in the retina will have profound impacts in not only our understanding of vision, but of what tools and capacity microcircuits have across the central nervous system.

---

[*] NO serves many functions in the retina, and its precursor NOS is expressed in photoreceptors, BCs and muller glia as well as ACs. It can increase cGMP which can increase rod signaling, though as a freely diffusible gaseous neurotransmitter its role on specific circuits in feature detection and other image forming visual modalities has been difficult to study (Goldstein et al., 1996).

Chapter 2: A Wide-field nNOS-Expressing Amacrine Cell Provides Global Inhibitory Input to Local Motion Detecting Ganglion Cells of the Mouse Retina

Joseph Leffler[1,3], Rowland Taylor[2]

1 Neuroscience Graduate Program, Oregon Health & Science University, Portland, OR 97239; 2 School of Optometry & Helen Wills Neuroscience Institute, University of California-Berkeley, Berkeley, CA 94720

This manuscript is presented as prepared for submission to the Journal of Neuroscience (2021)

PREFACE

This chapter characterizes a newly identified inhibitory input to a functionally distinct ganglion cell type in the mouse retina. I conducted this study under the mentorship and guidance of Dr. W. Rowland Taylor. I designed and performed the experiments, analyzed the data, and wrote the manuscript. Dr. Taylor provided guidance with experimental design, assisted in the data analysis, and preparation of the manuscript.

This study builds on the work of many researchers who have studied object motion sensitive circuits. Object motion sensitivity is a known feature-selective aspect of vision that has been studied both in visual cortex and the retina. How can a perceptual system discern motion in the world from self-generated motion? There are likely distinct mechanisms generating this feature selection at both levels, and how the motion sensitivity of the retina is transmitted and used by central circuits is an open question. Early work in primate visual cortex concluded self-generated motion and object motion could not be distinguished (Wurtz 1968, 1969a, 1969b). However, subsequent studies found more ambiguous results using different visual stimuli and recording techniques (Bridgeman 1972; Galletti et al. 1984; Fischer et al., 1981; Battanglini et al., 1986; Ilg and Thier 1996).

Identification of retinal cell types that could discern object motion from self-generated or global motion did not occur until 2003 when Olvezky and colleagues identified object motion sensitive cells in both salamander and rabbit retina (Olveczky et al.,2003, 2007, Baccus et al., 2008). Subsequent studies in mouse leveraged cell specific targeting techniques and have honed in on several mechanisms of inhibition and excitation from distinct cell types. This includes the TH-2 AC, the vGlut3 AC, and an as yet unidentified spiking AC (Zhang et al., 2012; Brüggen et al., 2014; Kim et al., 2017; Lee et al., 2014; Tien et al., 2016; Tien et al., 2017). The study presented in this chapter provides evidence for the NOS2 AC's inhibition of a motion detecting circuit in mouse retina during global motion.

ABSTRACT

Local motion detecting (LMD) ganglion cells (GCs) in mice respond to local movements in the environment, but stay silent during global motion generated during eye movements or self-generated motion. Some presynaptic excitatory and inhibitory inputs to these cells have been characterized recently, but to what degree these inputs are impacting the specificity of the LMD GC response and how those inputs themselves compute local and global motion is not fully understood. Here we show that a genetically targetable inhibitory interneuron, the NOS2 amacrine cell (AC), receives strong inhibition and is weakly depolarized during local motion and receives weak inhibition and is strongly depolarized during global motion. Optogenetic activation shows NOS2 ACs provide $GABA_A$ receptor mediated inhibitory input to LMD GCs, that receive strong inhibition during global motion absent during local motion. This study illustrates a novel source of inhibitory input to a motion detecting ganglion cell circuit.

INTRODUCTION

The nervous system leverages a wide array of inhibitory interneurons to transform excitatory projection neuron's output from one brain region to another or within a single area. One outcome of this diversity of cell types, far outnumbering their excitatory counterparts, is that many of their functions are unknown or poorly understood. The diversity of amacrine cells in the retina is quite large, the latest data putting the estimate at around 60 molecularly distinct types (Zeng & Sanes, 2017, Yan et al., 2020), and around 45 morphologically unique types (MacNeil *et al.*, 1999;

Badea & Nathans, 2004; Lin & Masland, 2006; Helmstaedter *et al.*, 2013). This diversity of ACs is thought to generate the retina's ability to encode diverse visual features through the output of around 40 output neurons, retinal ganglion cells (RGCs) which send trains of action potentials to retino-recipient zones in the brain. ACs influence RGCs either directly through input to their dendrites (postsynaptic inhibition), or presynaptically through the axons of bipolar cells or other ACs (Eggers et al 2007)**.** Most ACs have unknown roles in shaping retinal output. It is still unclear if individual ACs preferentially provide pre or postsynaptic inhibition to a single GC type, or if they contribute to multiple components within one or across multiple circuits.

Object motion detection of predator or prey movement is an evolutionarily conserved and essential function of the visual system. It requires cohorts of neurons to signal presence of the moving object with great fidelity in comparison to globally moving objects generated by eye movements or other self-generated motion (Olveczky et al., 2003; Baccus et al., 2003). LMD GCs in the mouse retina are activated through dendritic excitation from bipolar cells, and a recently studied glutamatergic AC (Lee et al., 2014; Jia et al., 2020; Tien et al., 2015, Tien et al. 2016, Krishnaswamy et al., 2015). However, during global motion and during differential motion—when an object moves in a direction that does not cohere with the background movement—LMD GCs are silent. (Kim and Kerschensteiner 2015; Zhang et al., 2012). This silencing comes both from inhibition of pre-synaptic bipolar inputs during global and differential motion as well as an excitatory AC providing that input during local motion. Additionally, direct inhibition of the LMD GCs dendrites has been demonstrated. (Kim and Kerschensteiner 2015; Krishnaswamy et al., 2015; Lee et al.,2014). Which AC types provide inhibition to presynaptic bipolar cells, and which ACs inhibit the LMD GC directly is not fully understood. Recent genetic targeting of wide-field AC types observed that the NOS2 AC stratifies in the same area as LMD GCs in the inner plexiform layer (IPL) (Jacoby 2018, Jacoby 2017, Zhu 2014). Here using optogenetic circuit mapping and targeted patch-clamp recordings, we identify that the NOS2 AC responds strongly to global motion, is strongly suppressed during local motion, and provides direct, GABAergic inhibition to LMD GC dendrites.

RESULTS

Genetic labeling strategy and morphological cell type identification

We crossed mice in which the neuronal nitric oxide synthase (nNOS) promoter drives expression of Cre recombinase (*NOS-Cre)* with a fluorescent reporter strain (*Ai9)*, and found expression of tdTomato (tdT) in a population of axon bearing, dendritically bi-stratified poly-axonal amacrine cells (NOS1) with cell bodies in both the INL and GCL and in a population of axon-less monostratified sublamina 3 (SL3) stratifying ACs (NOS2) with cell bodies also both the INL and GCL. Under two-photon guidance, in a dark-adapted whole-mount preparation of the mouse retina, placed photoreceptor-side down in a recording chamber on a translating stage microscope, we targeted these populations for patch-clamp recordings. We filled individual cells with Alexa Fluor 488 revealing wide-field neurite arborizations at distinct IPL depths relative to tdT reporter expression. We also included neurobiotin (NB) in the recording pipet to better recover wide-field morphology and visualize the gap junction coupling pattern of either cell type as well as image the relative stratification depth of NOS1 and NOS2 cells to starburst amacrine cell arbors by co-staining for choline acetyl transferase (ChAT). An example NOS2 AC cell fill is shown in figure 2.1 A-B with the initial cell filled indicated by an arrow. NB fills the arbor of that starter cell and also permeates to other NOS2 tdT+ somas and arbors in the vicinity (NB in yellow, tdT in magenta, and overlapping areas shown in

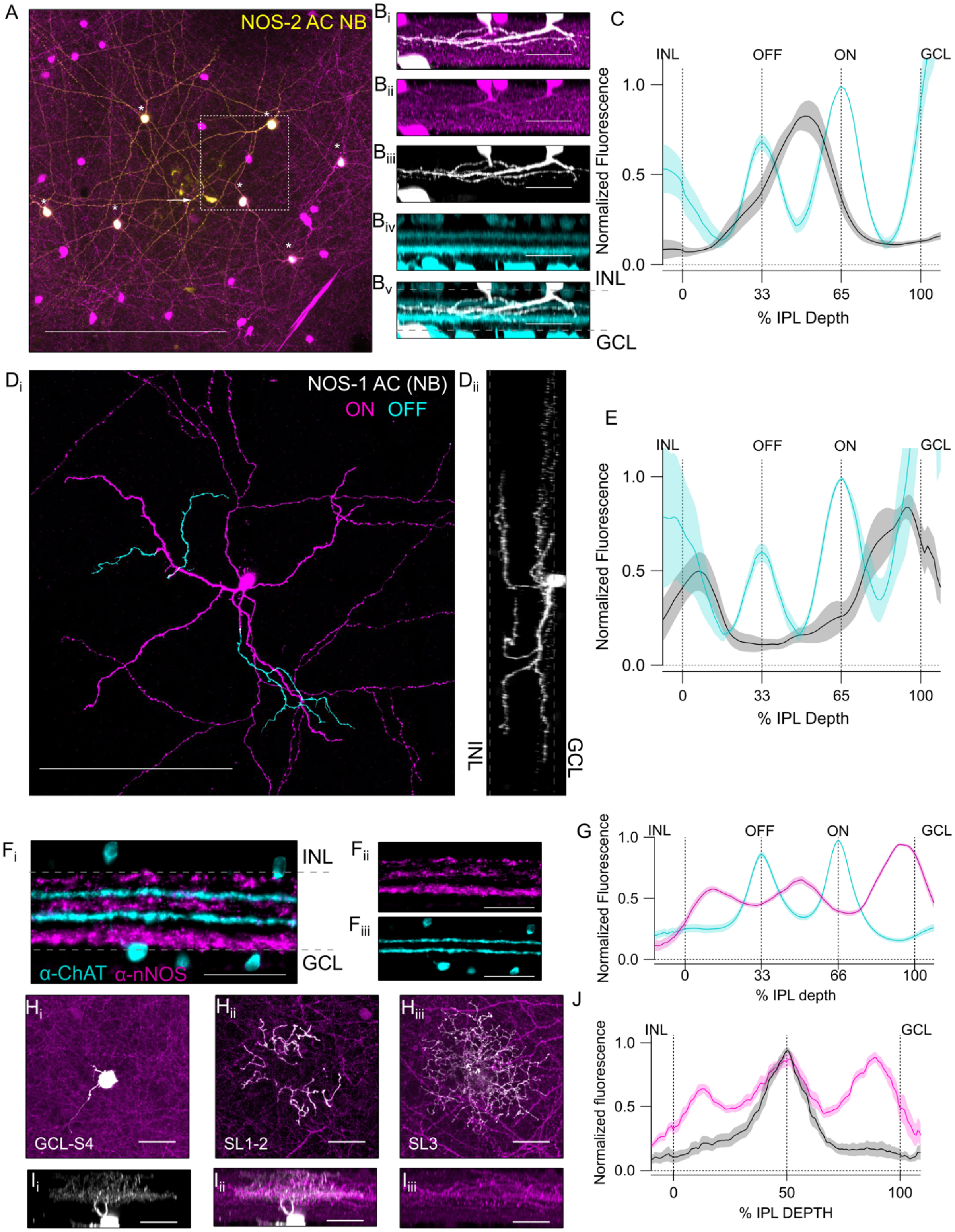

FIGURE 2.1 Genetic labeling strategy and morphological identification of NOS+ ACs and LMD GCs

(A) Z-projection through inner retina in a top-down view of NB fill (yellow) of a single NOS2 AC starter cell (arrow) and dye-spread to neighboring NOS2 ACs (*s) Continued on next page→

white). Looking at the side view of the confocal image stack from a subregion of Figure 2.1 A indicated by a dotted line reveals the stratification pattern of these dye-coupled NOS2 cells in the middle of the inner plexiform layer. $B_{i\text{-}iii}$ shows NB in white and tdT in magenta merged (B_i) or in separate channels (B_{ii}, B_{iii}). To quantify the stratification depth and normalize across tissue samples which varied in thickness, we co-stained for ChAT (shown in cyan in panels B_{iv} and B_v) which is a known marker in the inner retina to plot relative stratification depth to the OFF and ON ChAT bands at ⅓ and ⅔ through the IPL. The summary across n = 8 cell fills is shown in Figure 2.1 C where a clear peak of NOS2 AC stratification at 50% IPL depth is shown.

NOS1 ACs show a different pattern of neurite stratification with a bi-stratified arbor including a narrow OFF band in SL1 that comes off of 1-3 principle descending dendrites from the primary ON arbor that laminates in S5. This is also where the thinner diameter axonal processes of the NOS1 cell laminate. A projection through a confocal image stack of a NB filled cell is shown in Figure 2.1 D_i, with the full depth of the inner retina collapsed into one projection in panel D_i, but with ON sublamina (SL4 and SL5) pseudo-colored magenta and OFF sublamina

---

FIGURE 2.1 CONTINUED→White label indicates overlap of tdT and NB. SB=250 µm (B) Cross sections through dotted region in A showing Neurobiotin (white) from NOS2 cell fill and overlap with tdT (magenta) or ChAT (cyan). SB=25 µm. (C) Fluorescence profiles of NOS2 ACs (black) normalized to the positions of peak fluorescence of the ON ChAT bands (cyan). Filled region indicates +/- SEM of normalized fluorescence across cells. n = 8 (D) Z-projection through inner retina in plan view of NOS1 AC filled with neurobiotin. (Dii) Cross section of Di. (Ei) Z-projection through SL1-2 of the IPL. (Eii) Z-projection from GCL to IPL SL4. SB D-F=250 µm (F) Fluorescence profiles of NOS1 ACs (black) normalized to the positions of peak fluorescence of the ON ChAT bands (cyan). Filled region indicates +/- SEM of normalized fluorescence across cells. n = 7. G) Vertical retinal sections from WT tissue stained for anti-nNOS (magenta) or anti-ChAT (cyan) SB=25 µm. (H) Fluorescence profiles of nNOS AB (black) normalized to the positions of peak fluorescence of the ON ChAT bands (cyan). Filled region indicates +/- SEM of normalized fluorescence across cells. N=7. (I-J) LMD GC fill in NosCreER;ChR2-YFP tissue. Ii shows z-projection through GCL-SL5, Iii shows SL1-2 z-projection, and Iiii shows z-projection through SL3. Ji-iii show cross sections through same cell as in I with and without overlap of NOS-YFP signal. (E) Fluorescence profile of LMD GCs (black) normalized to the position of the of the SL3 band of NOS-YFP fluorescence. N=8

(SL1 and SL2) in cyan. D_{ii} shows the side view of this confocal image stack demonstrating the bi-stratified morphology of a NOS1 AC. Viewed as an average normalized intensity profile of individual NOS1 cell fills, the extremities of these two stratification depths are more easily visualized. The % IPL depth of OFF and ON arbors from single NOS1 cell fills was 10% and 90%, respectively (Figure 2.1 E). We compared the stratification depth locations of NOS1 and NOS2 cell fills to nNOS antibody staining in vertically sectioned wildtype tissue. A representative merged ChAT (cyan) and nNOS (magenta) stained section is shown in figure 2.1 F_i, separate channels in $F_{ii\text{-}iii}$. Averaging across the normalized fluorescence intensity profile of 25 sections of retina from four mice allowed us to identify the relative peaks of nNOS antibody staining to that of ChAT antibody staining (12%--NOS1 OFF band, 53%--NOS2 band and 91%--NOS1 ON band) (Figure 2.1 G). We compared those locations to the single cell fill stratification depths and found the nNOS antibody recapitulated single cell fills of nNOS;tdT tissue well. This demonstrates the location of nNOS-CreER;tdT fluorescence in our genetically labeled tissue recapitulates the wildtype expression of nNOS.

We then compared the stratification depth of local motion detector ganglion cells (LMD GCs) to that of both NOS+ AC types in NOS-CreER; ChR2-YFP tissue to hypothesize which group of ACs were more likely to be connected to these LMD GCs. Figure 1 $H_{i\text{-}iii}$ show sub-stacks of an image series taken on a 2-photon microscope through the three nNOS peak regions that the different arbors of NOS+ ACs stratify. H_i shows the region from GCL to SL5 where NOS1 ON arbors stratify in which we see little overlap between LMD GC fill and NOS YFP signal. SL4-5 is shown in H_{ii} in which a small degree of overlap is observed between GC and the NOS1 OFF band, and H_{iii} shows a large degree of overlap between SL3 NOS2 arbors and the bulk of the LMD GC dendritic arbor. $I_{i\text{-}iii}$ show side views of this same image stack with and without overlap between the Alexa Fluor 588 cell fill in white, and magenta NOS-YFP signal. An average of 8 LMD GC fills are shown in Figure 2.1 K to more clearly show the overlap between the S3 NOS2 peak (magenta) and the LMD GC arbor.

ChR2 expression allows selective activation of NOS+ACs

Given the co-stratification between NOS2 ACs and LMD GCs we used optogenetics to test if NOS2 ACs provide input to LMD GCs and to analyze what neurotransmitters and receptors mediate any potential communication. We first recorded from NOS+ ACs expressing ChR2 fused to YFP to identify stimulus parameters that could activate NOS+ ACs to a similar

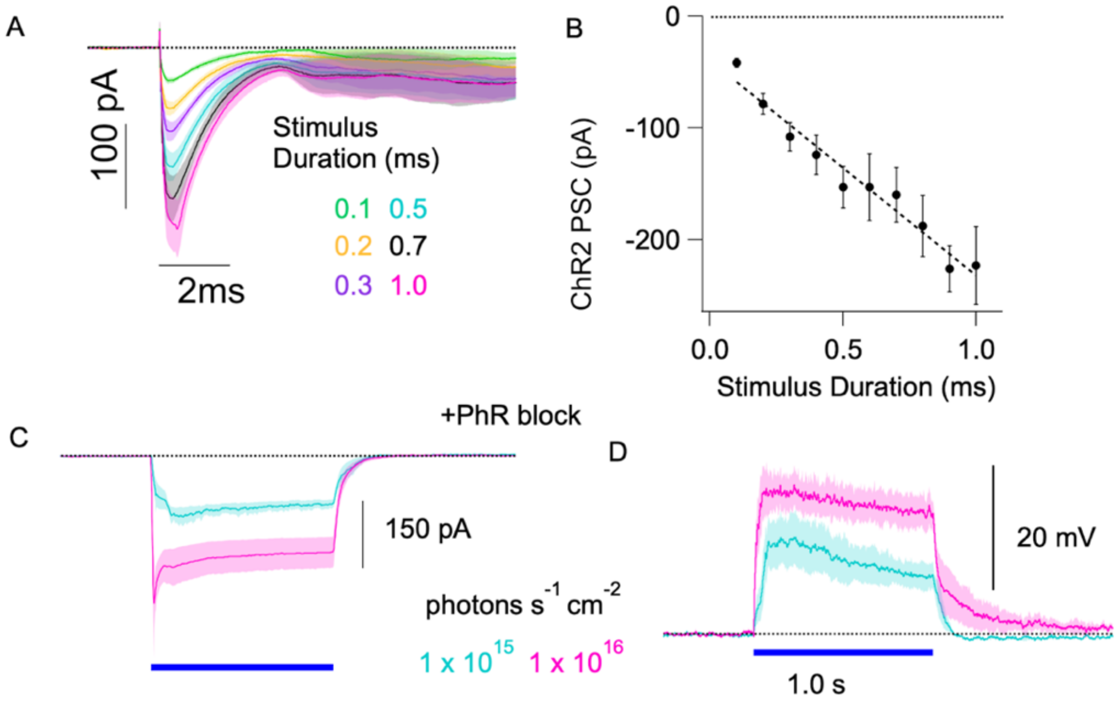

FIGURE 2.2 ChR2 expression allows selective activation of NOS+ACs

(A) Blue light-evoked EPSCs in NOS+ ACs in NOS-ChR2 tissue at a range of stimulus durations. (B) Amplitude of brief blue-light evoked EPSC at a range of stimulus durations. (C) Average PSCs at indicated blue light intensities during a 1s stimulus with cocktail of drugs applied to block photoreceptor responses. (D) ChR2 mediated PSPs in response to 1s blue light stimulus (N=5) degree as visible light. We found a linear relationship between peak optogenetic, light-evoked currents and duration of blue light (470 nm LED) from 0.1 ms to 1 ms (5 x 10^{15} photons s^{-1} cm^{-1}). These brief flashes were performed with photoreceptor responses intact and used the short latency of ChR2 activation to distinguish between optogenetic and PhR driven EPSCs (Figure 2.2 A-B). We also blocked PhR transmission to bipolar cells with a cocktail of L-AP4 (20 µM), ACET (2 µM), D-AP5 (50 µM) and GYKI-53655 (50 µM) in the extracellular solution and presented longer flashes (1s) of the same intensity blue light as well as an order of magnitude attenuated blue light and saw a reduction in both depolarizations and EPSCs in NOS+ ACs (Figure 2.2 C-D).

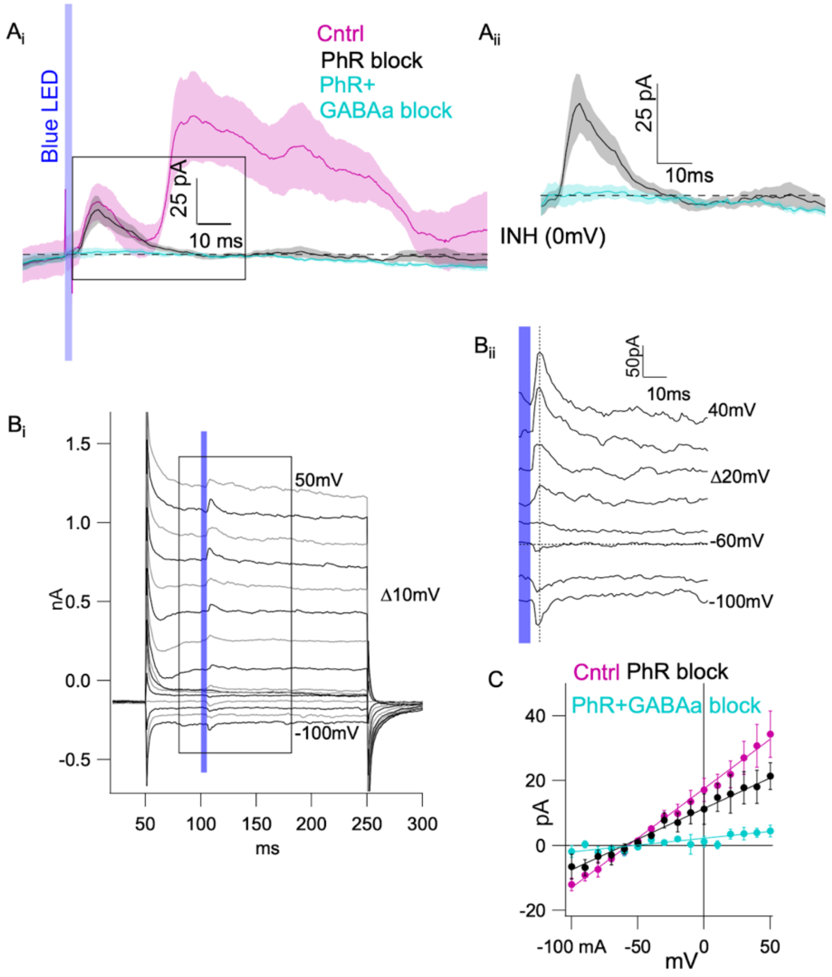

FIGURE 2.3 Optogenetic inhibition from NOS2 ACs to LMD GCs

(A) Blue-light evoked IPSCs in LMD GCs in control (magenta), photoreceptor blocking cocktail (black) and cocktail plus GABAa antagonist (cyan) (n=8). (B) Representative traces at holding potentials between -+100 and 50mV. Bii shows expanded x/y axis in region indicated in Bi. (c) Average IV of blue-light driven inputs to LMD GCs with and without PhR block and GABAa antagonists. (n=8)

Optogenetic inhibition from NOS2 ACs to LMD GCs.

We obtained patch-clamp recordings from LMD GCs in retinas in which NOS+ ACs express ChR2-YFP (Figure 2.3). Holding LMD GCs at 0mV (the reversal potential of excitatory inputs) allowed us to isolate inhibitory synaptic inputs. Brief (2-5 ms) stimulation reliably elicited short latency ChR2 evoked IPSCs in LMD GCs followed by longer latency photoreceptor driven IPSCs. When photoreceptor transmission was blocked as in Figure 2.2 C-D, the slow IPSC portion was occluded and the short-latency ChR2 mediated IPSC remained (black trace in Figure 2.3 A_{i-ii}). These ChR2 mediated IPSCs were blocked by application of the $GABA_A$ receptor antagonist SR-95531 (gabazine) (Figure 2.3 A_{i-ii} cyan traces). We also held the LMD GCs across a range of potentials and found the ChR2 mediated input reversed near the inhibitory reversal potential This confirms that GABAergic input from NOS2 ACs to LMD GC dendrites is indeed inhibitory.

NOS2 output matches the spatial extent of LMD postsynaptic inhibition

Given this optogenetic driven inhibitory input to LMD GCs, we wanted to measure the photoreceptor driven inhibitory input to LMD GCs and compare it to the receptive field size of the NOS2 AC. Under two-photon guidance, we targeted the NOS2 population of ACs in the GCL for patch-camp recordings and measured their visually evoked membrane potentials across a range of stimulus sizes (EG PSPs in Figure 2.3 A, averages in 2.3 B). A previous report of NOS2 AC responses showed that at a photopic background, and at 100% Weber contrast, which we also used here, NOS2 ACs responded with depolarization at light onset and offset. However, that study only reported a single diameter size, and the exact diameter was not reported (Jacoby and Schwartz, 2018). We observed a similar ON-OFF depolarization response in NOS2 ACs across a wide range of stimulus diameters and fit the ON and OFF responses each with a single

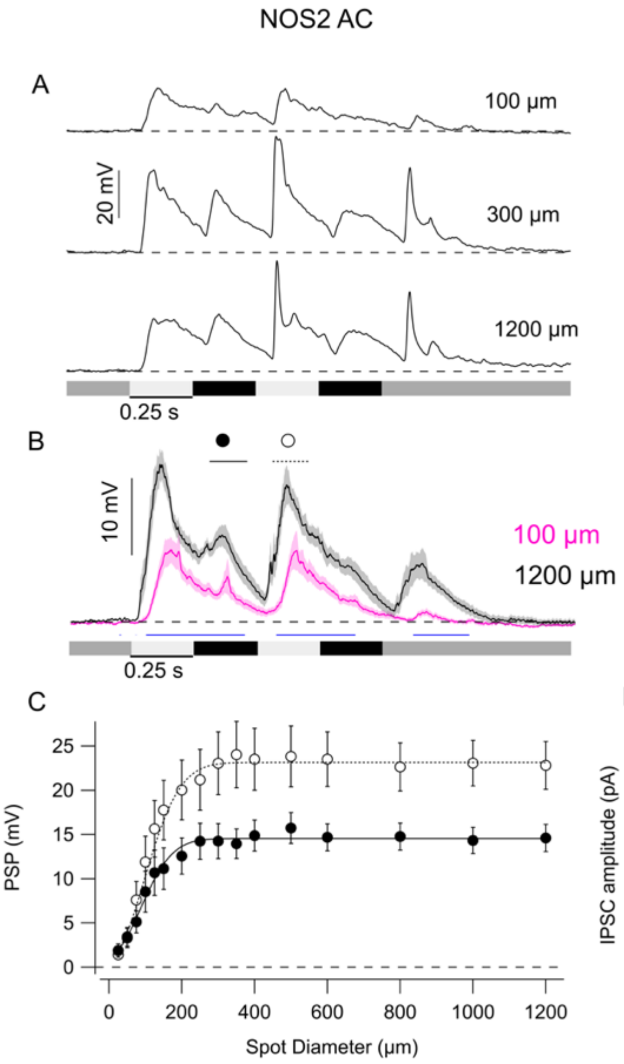

G

NOS2-AC	Center (in µm)	LMD-GC	Center (in µm)
ON ○	137 ± 5	ON △	143 ± 8
OFF ●	122 ± 6	OFF ▲	121 ± 10

FIGURE 2.4 NOS2 AC output matches the spatial extent of LMD GC postsynaptic inhibition

Example (A) Example and (B) average PSPs at indicated spot sizes in response to 2 Hz square-wave flicker in NOS2 ACs. N=18. (C) Area response function from NOS2 AC PSPs measured at the indicated timepoint in B fit by a single Gaussian with center amplitudes of 17 ± .07 mV (ON) and 8 ± .05 mV (OFF). Example (D) and average (E) IPSCs at indicated spot sizes in LMD GCs. N=17. (F) Area response function from LMD GC IPSCs measured at the indicated timepoint in E fit by a single Gaussian with center amplitude of 190 ± 17 pA (ON) and 170 ± 9 pA (OFF). (G) Center Gaussian widths ± one standard deviation from C,F. Blue lines in B and E indicate $p < 0.05$, Student's t test

Gaussian (dashed and solid lines in Figure 2.4 C) with a center size of 137 ± 5 (ON), and 122 ± 6 µm (OFF), respectively. By holding LMD GCs at 0mV to isolate inhibitory inputs (example IPSCs in Figure 2.4 D and averages in E) and presenting the same range of spot sizes as for NOS2 ACs, we calculated the fits for their inhibitory inputs and found similar Gaussian widths (143 ± 8 µm for ON, and 121 ± 10 µm for OFF inputs, Figure 2.4 F). This means that a stimulus size that maximally activates the NOS2 AC is the same size as a stimulus that drives maximal inhibition to the LMD GC.

LMD output is shaped by wide-field presynaptic and narrower postsynaptic inhibition

The presence of inhibitory input from NOS2 ACs does not necessarily mean that NOS2 ACs are responsible for generating the LMD GC surround, which has been shown in the literature to receive strong surround suppression from multiple sources (Zhang et al., 2012; Jacoby et al., 2017, Kim and Kerschensteiner, 2017). Though its source is debated, it is likely true that multiple inhibitory contributions from different populations occur. Another complicating factor are the different methods used to target these LMD GC by different labs. Notably, use of the W3-GFP transgenic reporter line, used by Zhang et al., 2012 and Kim and Kerschensteiner in 2017 likely result in a different population of LMD GCs being studied as compared to studies using morphology or light responses alone or in concert. One study, Jacoby and Schwartz 2017, identified four different populations of small receptive field GCs stratifying in the same sublamina of the IPL as those identified by the W3 transgenic line. Here we based our identification on morphology and function, and potentially have a heterogeneous population of several similar functional and morphological types. To test if the IPSCs originating from NOS2 AC are shaping the LMD GCs' surround inhibition and spike suppression, we measured their photoreceptor driven spiking in cell-attached mode (Figure 2.5 A-B). When presented

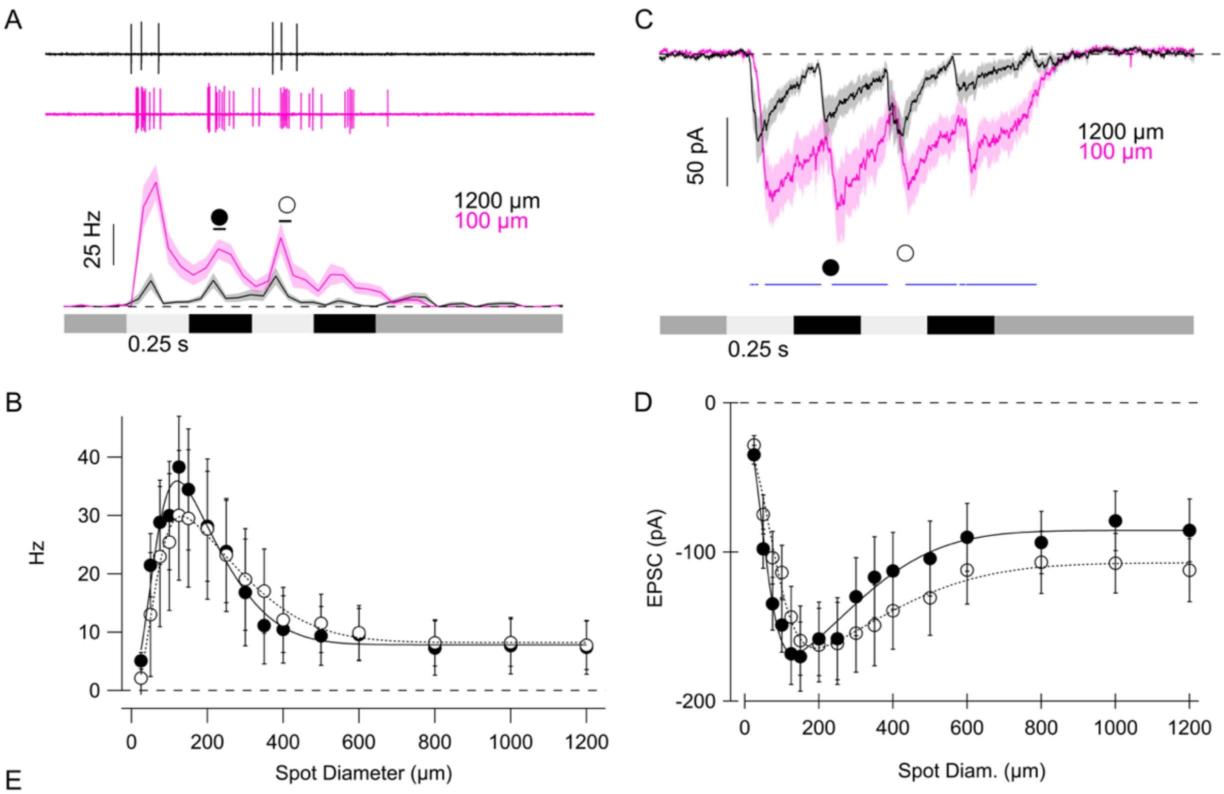

E

	Action Potentials Center	Action Potentials Surround	EPSCs Center	EPSCs Surround
ON ○	70.7 ± 8	321 ± 18	96.0 ± 7	443 ± 63
OFF ●	63.0 ± 10	251 ± 22	65.4 ± 5	362 ± 32

FIGURE 2.5 LMD GC output is shaped by wide-field presynaptic and narrower post synaptic inhibition

(A) Example light-evoked action potentials (upper) and spike-time histograms (lower) at indicated spot diameters in response to 2 Hz square-wave flicker in LMD GCs. n=21. (B) Area response function from LMD GC spike time histograms measured at the indicated time window in A fit by a Difference of Gaussians function with center amplitudes of 37 ± 1.7 (ON) and 44 ± 4.2 (OFF) and surround amplitudes of -38.7 ± 4 (ON) and -27 ± 1.5 (OFF). (C) Average EPSCs at indicated spot sizes in LMD GCs. n=17. (D) Area response function from maximum LMD GC EPSCs measured at the indicated time window in C (horizontal lines over filled (OFF) and white (ON) markers) fit by a Difference of Gaussian with center and surround amplitudes of -151 ± 10 pA and 72 ± 9 (ON) and -166 ± 10 pA and 98 ± 7 pA (OFF). (E) Center Gaussian widths ± one standard deviation from B,D. Blue lines in C indicate $p < 0.05$, Student's t test with small diameter stimuli flickering at 2 Hz, LMD GCs fire robustly at each contrast transition, but only respond weakly at larger stimulus sizes. Peri-stimulus spike-histograms in the bottom traces of Figure 2.5 A show a significant reduction in spike output at a large stimulus diameter. We plotted spike rate vs diameter size taken at the indicated time points by horizontal bars in Figure 2.5 A, revealing a strong and narrow surround suppression fit by a difference of Gaussians function with a surround size of 321 ± 18 μm (ON) and 251 ± 22μm (OFF). This is considerably wider than the center Gaussian for NOS2 ACs from Figure 2.4 B and the LMD IPSCs from Figure 2.4 D. However, if we compare that surround width to the surround Gaussian fitted to EPSC amplitudes taken at time points indicated in Figure 2.5 C, which shows average EPSCs at two stimulus diameters, we see the EPSC surround, generated pre-synaptically, is wider than inhibitory input to or extracellular output from LMD GCs. This leads us to consider NOS2 ACs may be fine-tuning the output of LMD GCs by further narrowing its receptive field size from the wider presynaptic mechanism observed in EPSCs to that of the intermediate width of surround suppression observed through extracellular recordings.

Inhibition but not excitation of NOS2 ACs is suppressed by wide-field stimuli

We then asked how NOS2 AC receptive fields might be structured such that they could filter out small field stimuli. Their wide-field morphology suggests they may be integrating excitatory inputs over a large area adding to increased responses at larger stimulus sizes, but there could equally likely be an inhibitory mechanism present at smaller spot sizes to reduce NOS2 depolarization during local stimuli. To test these two possibilities, we recorded excitatory and inhibitory postsynaptic currents (EPSCs and IPSCs) from NOS2 ACs across a range of stimulus diameters to isolate excitatory and inhibitory inputs to NOS2 ACs and compared the center and surround widths of these inputs to that of the voltage response observed in Figure 2.4

A-C. NOS2 ACs display ON pathway IPSCs shown in Figure 2.6 A, upper traces and positive polarity markers in B, recorded at 0mV with a maximum of 63.9 ± 20 pA at 150 µm that is suppressed by 76.6% to a minimum at 1200 µm of 14.9 ± 8.7 pA. This initial rise and subsequent decay is described by a Difference of Gaussians (DOG) function with a center width of 116 ± 18 µm and a surround width of 439 ± 74 µm. This pattern may reflect a local inhibitory input from an amacrine cell with a center diameter of around 250 µm (suggested by 2x the center Gaussian width), and a wider inhibitory input with a receptive field diameter around 1mm that subsequently suppresses that initial inhibitory input at larger spot sizes. OFF inhibitory outward currents showed a similar spatial pattern but with smaller overall amplitudes (27.4 ± 10 pA center at 150 µm and 14.5 ± 8 pA at 1200 µm).

Excitation, here displayed as inward currents in the bottom traces of Figure 2.6 A and negative polarity markers in B were recorded at -70 mV and display a different spatial arrangement to that of inhibition. NOS2 ACs reach a center maxima at 200 µm for both (84.6 ± 9.6 pA) ON and (43.3 ± 5.9 pA) OFF with weak surround suppression of 27.2% and 24.9% for ON and OFF pathways, respectively. However, OFF pathway EPSCs showed a similar pattern of amplitude to that of IPSCs and voltage responses in that the OFF pathway was always about half the size of the ON pathway, likely reflecting a weaker OFF pathway input both for excitation and inhibition.

To further investigate these differences in inhibition and excitation we isolated the underlying conductance driving these inputs by holding NOS2 ACs at a range of potentials between -90 and +50 mV. At each step, light evoked currents were recorded in response to the same 2hz flashing spot stimulus used in Figure 2.6 A-B, but at two diameters. We used a centered spot covering a peri-somatic region tuned to the peak of the NOS2 AC's IPSCs (magenta traces/markers) or a full-field 1200 μm diameter spot extending out past this RF center (black traces/markers). Example PSCs at the indicated potentials from NOS2 ACs are shown in Figure 2.6 D. Current-voltage relationships were calculated at 10 ms intervals during voltage steps, and at each time point, the linear excitatory and inhibitory conductance was calculated from best-fit I-V curves (see methods/citations). Current-voltage relations at indicated time points for both cell types are shown in Figure 2.6 E with filled markers for OFF responses, and open markers for ON responses. It is initially apparent that there is a reduction in the outward current measured at positive potentials, particularly in the ON pathway, which can be quantified by looking at the underlying conductance across the stimulus time course. Additionally, there is a small shift in I-V relationship to the right when comparing between center and full-field spot sizes, suggest that there is a similar suppression of inhibitory conductance, in line with what we observed from recording 0 mV across a range of stimulus sizes.

Both linear ($G_{A/K}$) and non-linear (G_{NMDA} mediated) excitatory conductance as well as inhibitory conductance (G_{INH}) are observed during the ON and OFF phase of the stimulus when narrow field stimuli are presented, (magenta traces, labeled center) though at roughly twice the amplitude for ON responses as OFF. At larger spot sizes, inhibition is reduced in the ON pathway while G_{NMDA} increases, potentially providing an offsetting mechanism to maintain the same net drive to the cell at these smaller diameter stimuli. Notably, linear excitation remains largely unchanged. From what we viewed previously from IPSC recordings at 0 mV, it appears that there is recruitment of added inhibition at smaller spot sizes that is suppressed by full-field stimuli, however, there may be compensatory non-linear excitation from NMDA receptors to offset this addition of inhibition at small spot sizes. Future studies could examine the spatial distribution of AMPA/Kainate compared to NMDA receptors along the dendritic arbor of NOS2

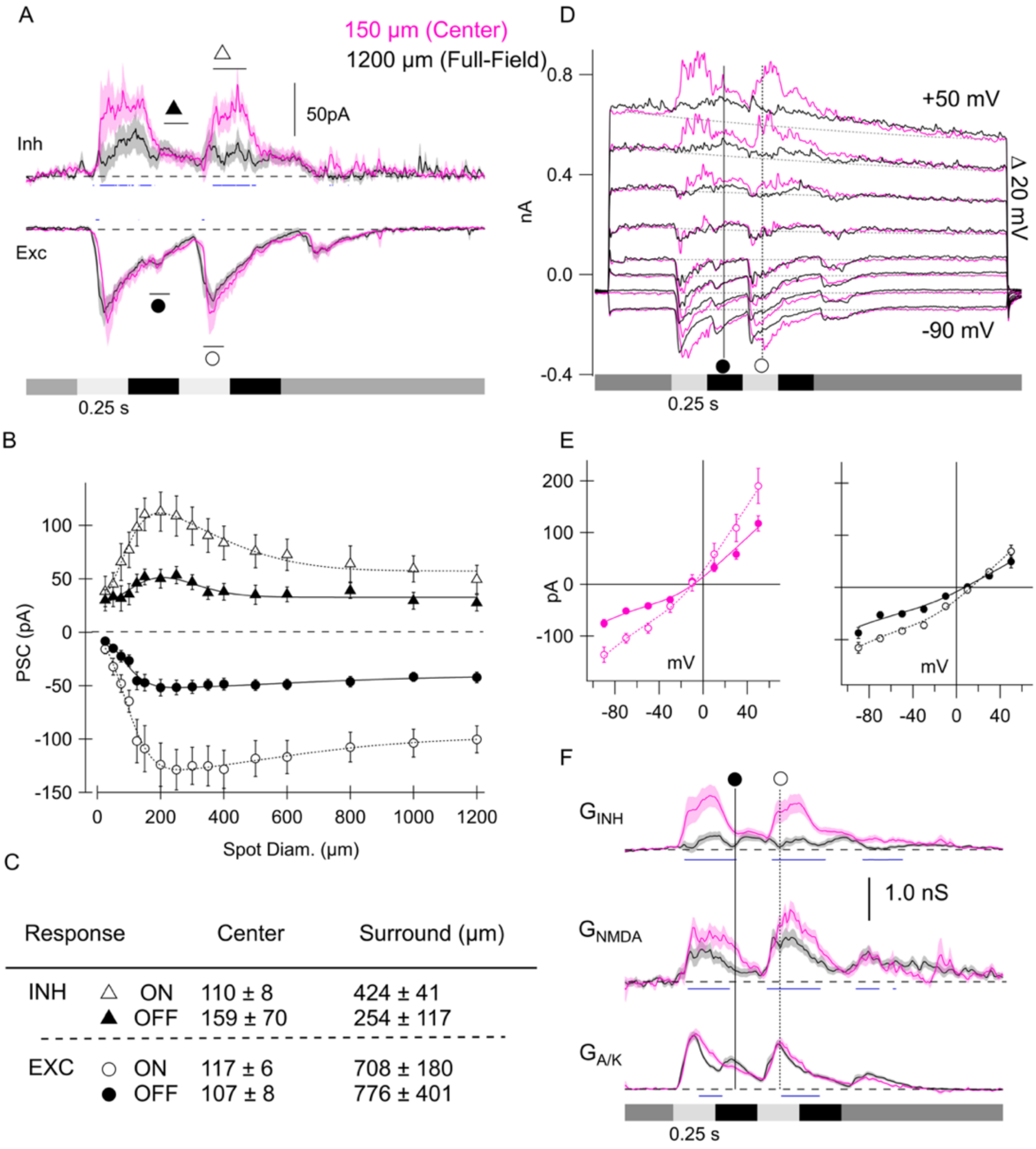

Response			Center	Surround (µm)
INH	△	ON	110 ± 8	424 ± 41
	▲	OFF	159 ± 70	254 ± 117
EXC	○	ON	117 ± 6	708 ± 180
	●	OFF	107 ± 8	776 ± 401

FIGURE 2.6 Inhibition, but not excitation of NOS2 ACs is suppressed by wide-field stimuli

(A) Average light-evoked inhibitory (upper) and excitatory (lower) PSCs at indicated center and full-field spot diameters in response to 2 Hz square-wave flicker in NOS2 ACs. N=17. (B) Area response function from min/max NOS2 ACs e/iPSCs measured over the time windows in A indicated by horizontal lines and corresponding ON and OFF markers fit by a DOG function with the following center and surround amplitudes. Inhibition: 99 ± 7 and (ON); 65 ± 11 pA and (OFF) and surround amplitudes of -72 ± 7 (ON) and -60 ± 11 pA (OFF). Excitation: -125 ± 5 and (ON); -48 ± 3 pA and (OFF) and surround amplitudes of 36 ± 5 (ON) and 12 ± 4 pA (OFF) Center and surround Gaussian widths ± one standard deviation from B. Continued on next page→

ACs that may reveal a structural component behind this observed functional difference of linear to non-linear inputs. The apparent lack of difference in excitatory conductance between center and full-field stimulus diameters here is likely due to the method used to select center sizes for these NOS2 ACs. We opted for spot sizes that drove maximal IPSCs (150-250 µm) which overlapped considerably with the initial peak of EPSCs (at 200 µm). Using smaller stimulus diameters that are more tuned to the receptive field center size of LMD GCs (75-125 µm) may result in a weaker excitatory conductance, as is suggested by the -70 mV recordings of EPSCs in NOS2 ACs. However, the overall arrangement of inhibitory inputs displaying strong surround suppression while excitation displays weak surround suppression together build the voltage response we see in Figure 2.4 in which NOS2 ACs are able to respond to medium and wide-field stimuli without signal attenuation providing a mechanism to continue responding to larger stimuli with consistent voltage responses. It additionally led us to ask if the inhibitory input we observed at smaller spot sizes may be functioning under a different stimulus context more pertinent to the LMD GC feature selectivity of local motion

NOS2 ACs receive separate ON and OFF bipolar cell inputs

Before further exploring the receptive field of NOS2 ACs and LMD GCs, we first asked if NOS2 ACs were truly receiving separate input from ON and OFF bipolar cell populations. While they laminate at the ON-OFF border of the IPL (in SL3) it is possible they are receiving all their input through one pathway or the other. For example, rebound excitation driven by

---

FIGURE 2.6 Continued→ Average EPSCs at indicated spot sizes in LMD GCs. N=17. (D) Example currents resulting from the same stimulus as in A-B, while holding NOS2 ACs at a range of voltages from -90 to +50 mV at center (magenta) and full-field (black) spot diameters. (E) Resulting I-V relations at indicated time points in D from N=40 NOS2 ACs with center (magenta) on the left, and full-field (black) on the right. (F) Inhibitory (G_{INH}), non-linear excitatory (G_{NMDA}), and linear excitatory ($G_{A/K}$) conductance derived from I-V relationships at all time-points during stimuli used in A-E. Blue lines in A,F indicate $p < 0.05$, Student's t test

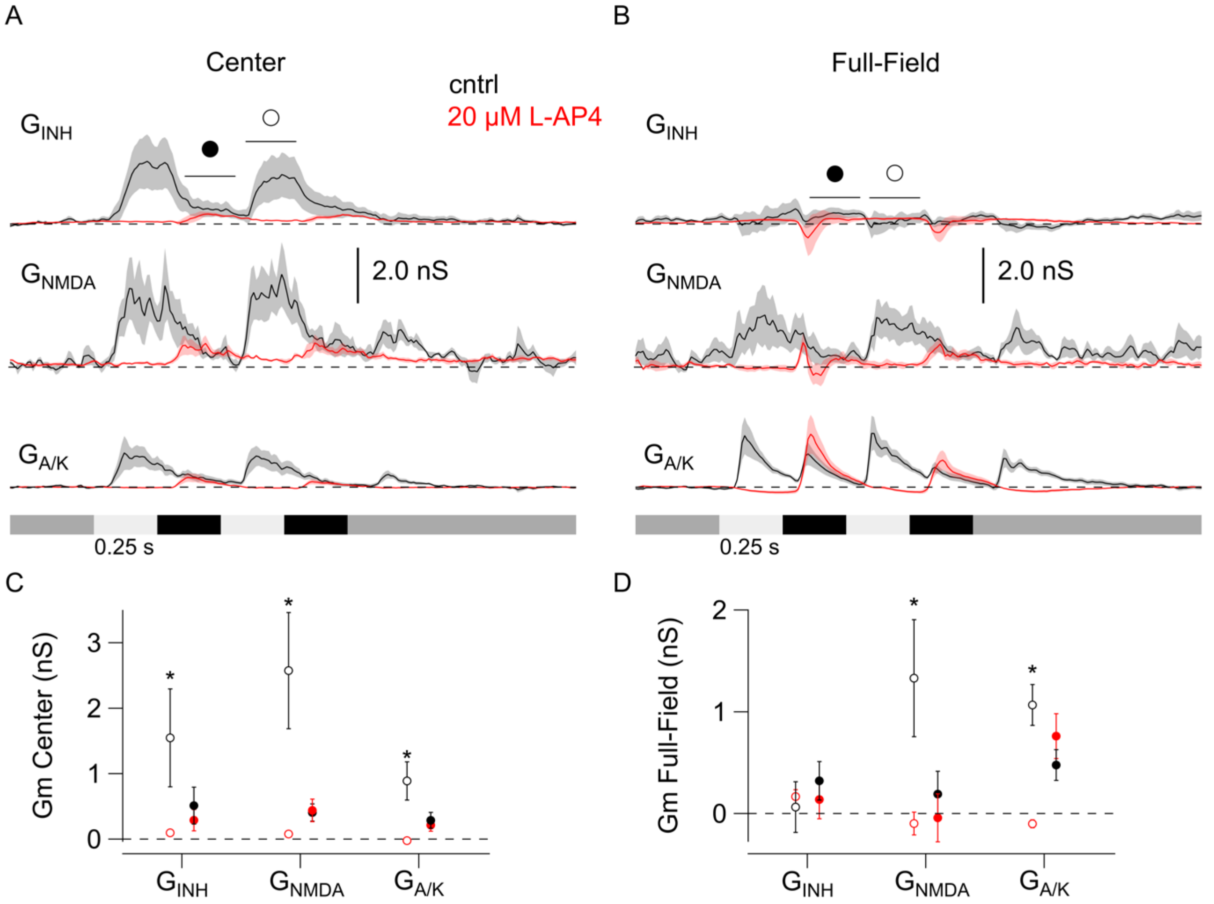

FIGURE 2.7 NOS2 ACs receive separate ON and OFF bipolar cell inputs

(A) Inhibitory (G_{INH}), non-linear excitatory (G_{NMDA}), and linear excitatory ($G_{A/K}$) conductance derived from I-V relationships during a 2 Hz flickering 150 µm diameter (A) or 1200 µm diameter (B) spot stimulus over the receptive field of n=5 NOS2 ACs in the presence (red) or absence (black) of mGluR6 receptor agonist 20 µM L-AP4. Average amplitude measurements were taken over the indicated time windows in A and B--solid lines and open (ON) or filled (OFF) markers and plotted in C (center) and D (full-field). Asterisks indicate significant differences ($p < 0.05$ Student's t test) between drug and control conditions.

release of inhibition. To distinguish between these possibilities, we recorded visually evoked light responses at two stimulus diameters isolating linear/non-linear excitatory conductance as well as inhibitory conductance as in Figure 2.6 D-F, and 20 applied 20 µM of the mGluR6 agonist L-AP4 to block responses from photoreceptors to ON Cone BCs. This resulted in a complete block of ON responses during both stimulus diameters. (Red traces, L-AP4, black traces, control). This also gives us a clearer view of the small amplitude of the OFF responses present during both stimulus sizes, and reveals a potential for a small degree of crossover inhibition that is relieved upon ON pathway block. Note the slight increase in OFF amplitude $G_{A/K}$ during full-field stimulus presentation in (Figure 2.7 B).

NOS2 ACs and LMD GCs are tuned to low temporal frequencies

To determine the speed of motion to use in probing the receptive field structure of LMD GCs and NOS2 ACs, we presented flickering spot stimuli at a range of frequencies from 1 to 30 Hz at 100% Weber contrast on a photopic background. Because we were interested in the inhibitory input from NOS2 ACs to LMD GCs, from our observed ChR2 mediated input between these two cell types, we recorded inhibitory input to LMD GCs and membrane responses of NOS2 ACs to determine the active range of frequencies to which they were both responding. Figure 2.8 A and C show average IPSCs and PSPs in either cell type, respectively at 2, 7.5, and 30 Hz. Clearly by 30 Hz both cell types fail to respond to the stimulus frequency. To better characterize this frequency response profile we calculated the Fourier transform function and focused on the fundamental (F1) present in the IPSCs and PSCs shown in Figure 8 A and C because it was by far the largest and represented most of the signal power. We found that both the LMD GC and NOS2 AC were best able to respond to low frequencies in both their F1 responses of both cell types. response. This result led us to use a low frequency drifting stimulus to probe the motion

LMD GCs show strong a strong preference for local motion

One of the key defining features of LMD GCs is their strong preference for local over global motion. We used this feature selectivity to initially target these cells using a modified version of stimuli other studies have used in the past (see methods and discussion for description and rationale for what stimuli were used). In brief, and graphically represented in Figure 2.9 A, gratings were initially presented to LMD GCs in a static manner for 1.0 s and then for a subsequent 5.0 s while drifting at a frequency of 1 Hz. We recorded action potentials resulting from these gratings that were masked off outside of 150 µm (local), or extended out to 1200 µm, (global). A third stimulus in which the center component of the grating was rotated 90° so it was orthogonal to the surrounding grating orientation was also presented (differential). PSTHs for each stimulus is shown in Figure 2.9 B. Note the rapidly adapting spike response to static stimuli followed by the more sustained spiking response during object drift. Under all three stimulus

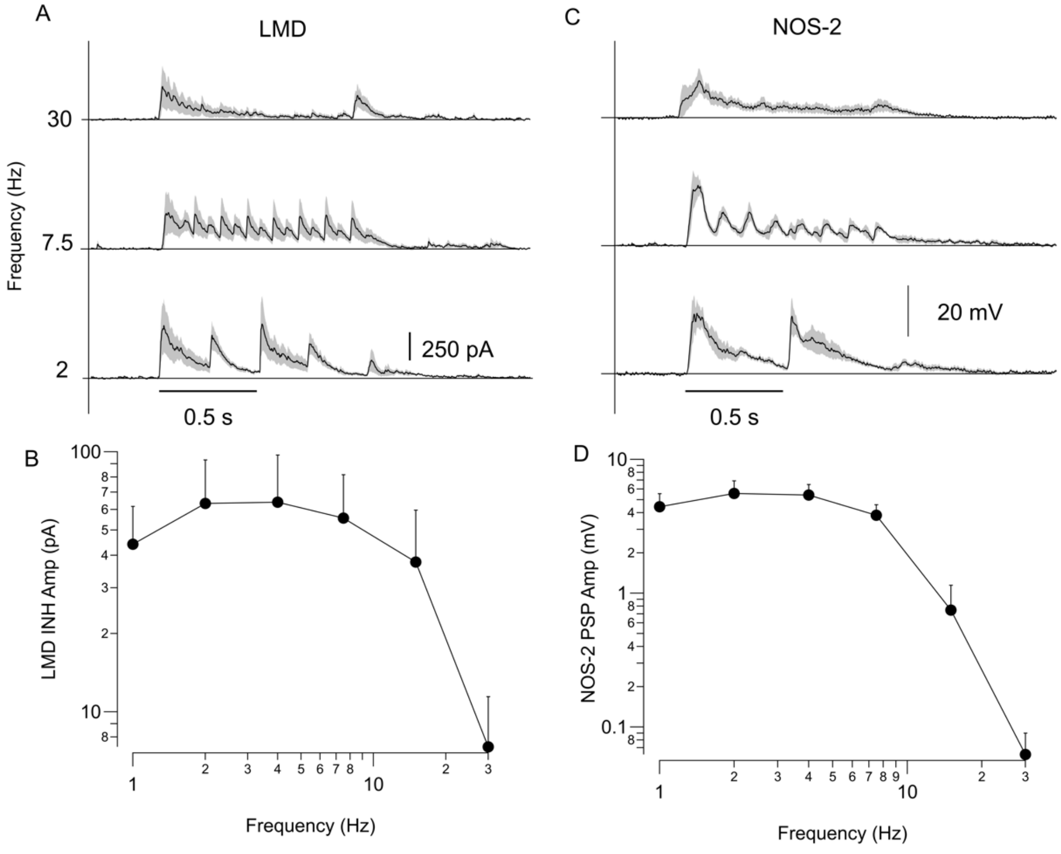

FIGURE 2.8 NOS2 ACs and LMD GCs are tuned to low temporal frequencies

(A) Average LMD GC IPSCs and (C) NOS2 AC PSPs at 2, 7.5, and 30 Hz. (B) Amplitudes of Fourier transform function for LMD GC IPSCs across a range of stimulus frequencies from 1 to 30 Hz. (D) Fourier transform amplitudes for NOS2 AC PSPs. Error bars and shaded regions display SEM mean. n = 5 LMD GCs and n = 6 NOS2 ACs.

conditions we observed a strong initial spike response when the object began to drift that reached a steady spike rate after ~1s of motion. This initial higher spike rate reflects an adaptation effect after the initial static grating presentation and the decay in spike rate over time is a desensitizing effect over the course of the five seconds of drifting stimulus.

We observed a significant decrease in spike rate in n = 12 LMD GCs during global relative to local or differential motion and no difference in the response to static stimuli. For drifting component: mean ± SEM in Hz: Local = 192 ± 47, Global = 62 ± 10, Differential = 127 ± 21 $p < 0.05$ *Global vs Local and Differential.* For the static component: Center = 16 ± 2.9, Global = 13 ± 2.5, Differential = 11 ± 3.0. Means ± SEM are plotted in Figure 2.9 C. We then patched LMD GCs and isolated excitatory and inhibitory conductance to determine what pre- and postsynaptic mechanisms were responsible for the observed local motion selectivity. We found in n = 9 LMD GCs the static portion of the stimulus drove a similar amplitude of inhibitory input (Mean ± SEM in nS: Local = 2.5 ± 0.57, Global = 1.9 ± 0.33, Differential = 2.0 ± 0.22, $p > 0.05$). The drifting portion of the stimulus however yielded a two-fold increase in inhibition during global motion relative to center motion alone (in nS: Global = 2.9 ± 0.45, Center = 1.5 ± 0.42 $p < 0.01$). Differential motion drove an intermediate level of inhibition (2.0 ± .48 nS,) which was significantly larger than center motion ($p < 0.05$), but did not differ Local compared to Global and Differential). This is consistent with some degree of a presynaptic mechanism of surround suppression that we saw in the area response profile in Figure 2.6, and a similarly small increase in excitatory input during local grating drift. It is notable that there was a smaller increase in excitation here as compared to Figure 2.6, which is likely due to the receptive field center and surround being subdivided into 75 µm bar widths. This tells us that the input

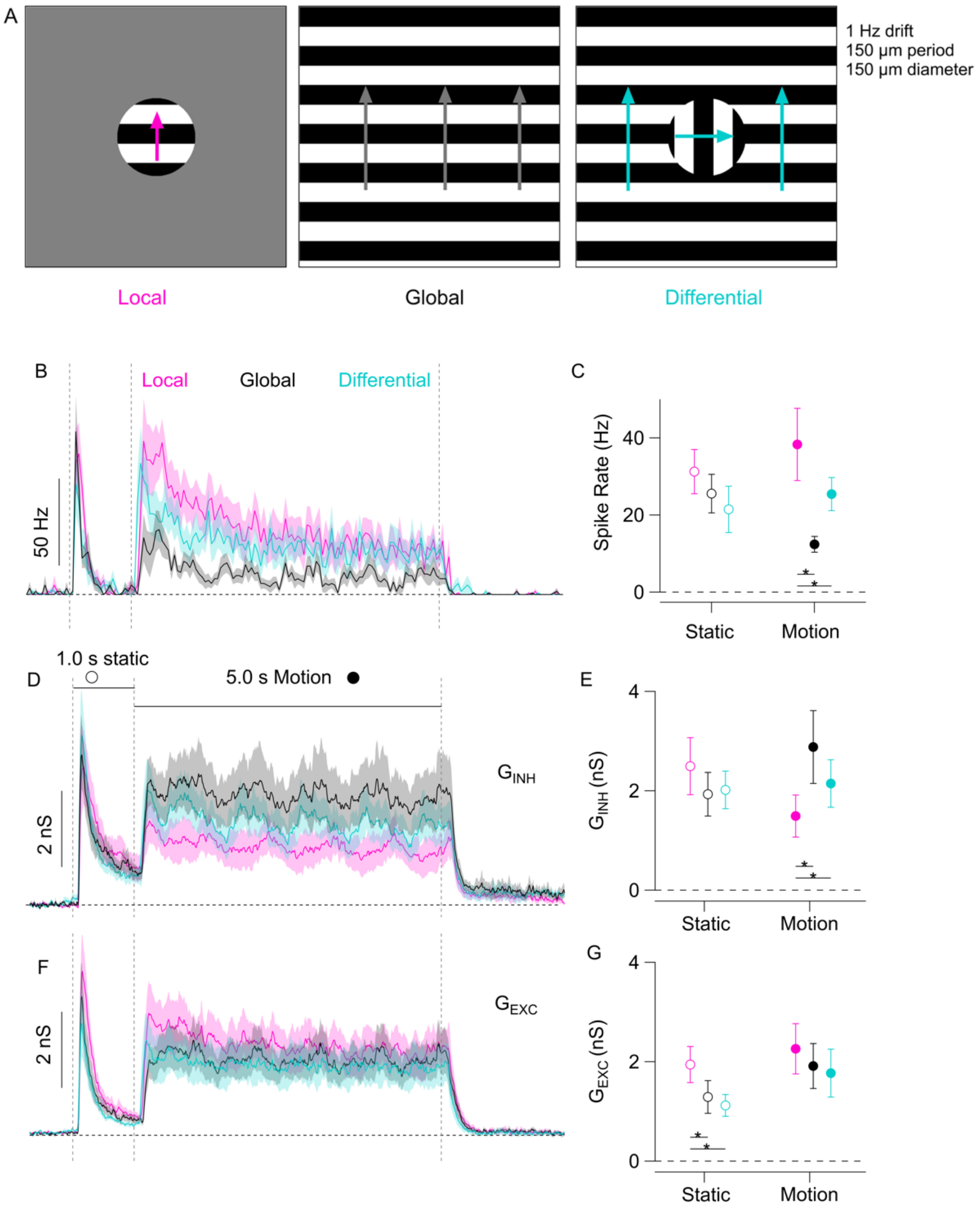

FIGURE 2.9 LMD GCs show strong a strong preference for local motion

(A) Schematic illustration of local, global, and differential motion stimuli used. Arrow and text color format maintained in B-G. The receptive field is divided into 150 μm period gratings (bar width 75 μm). For local stimuli motion outside of 150 μm is set to gray adaptive background level. Arrows indicate direction of motion. (B) PSTH from n=12 LMD GCs during initial 1s static gratings and subsequent 5s drifting gratings in color-matched regions. (C) Average spike rate over static (unfilled markers) or drifting (filled makers) portion of grating stimulus. (D) Average and (E) summary plot of inhibitory conductance during static and drifting grating presentation. (F) Average and (G) summary plot of excitatory conductance during static and drifting grating presentation from the same n = 12 LMD GCs. * = $p < 0.05$ Student's t test driving the pre-synaptic mechanism providing the bulk of the LMD GC's inhibitory surround when presented with a stimulus of a single contrast value, is poorly activated when divided into ON and OFF portions. This indicates surround input is likely signaling in a linear manner such that ON and OFF inputs cancel out when gratings that activate both polarity inputs are presented at the same time. The drifting portion of the stimulus did not lead to significant differences in excitatory conductance under any of the three motion stimuli used here. This is somewhat surprising given the initial result in the W3 genetic line demonstrating a strong spike-dependent presynaptic mechanism. (Zhang et al., 2012) However, given the differences in cell-type targeting used here as well as differences in visual stimuli, this may actually be a demonstration of the heterogeneity in presynaptic mechanisms that help drive motion sensitivity depending on cell type and specific visual stimuli context.

NOS2 ACs are depolarized by global and differential, but not local motion

To help answer the outstanding question of what role NOS2 ACs are playing in shaping LMD GC selectivity for local over global motion, and to a lesser extent, over differential motion, we recorded light evoked membrane responses in n = 6 NOS2 ACs. Figure 2.10 A shows that the NOS2 AC has a rapidly adapting response to all three static stimuli and showed no significant difference in average response over the 1.0 s of static stimuli (mean ± SEM in mV: Local = 7.8 ± 1.1, Global = 6.8 ± 0.9, Differential = 6.9 ± 0.48). However, they respond in a much more sustained manner during global and differential drift. We found a significant reduction in response amplitude during Local motion relative to global and differential motion. (mean ± SEM in mV: Local = 4.3 ± 1.0, Differential = 10.4 ± 1.8, Global = 12.6 ± 1.8; *$p < 0.05$ between Local vs Global and Local vs Differential.*) This corresponds well with the observed increase in inhibition of LMD GCs during global motion, but the fact that NOS2 cells responded similarly to global and differential motion suggests that there are other sources of inhibition that may be selectively providing differential-motion specific input to the LMD GC. Membrane depolarization was averaged over the static and drifting stimulus portions to directly compare the degree of activation that either component of the stimulus evoked (Figure 2.10 B).

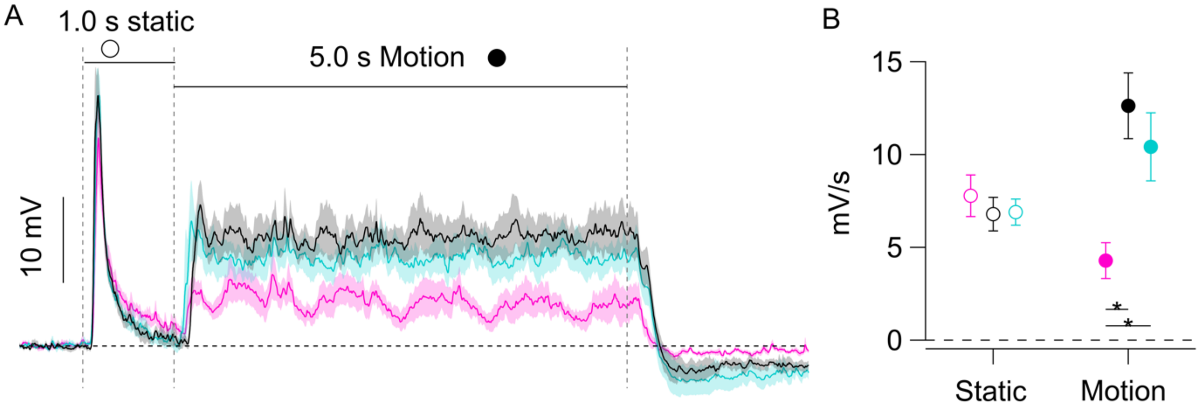

FIGURE 2.10 NOS2 ACs are depolarized by global and differential, but not local motion

A) Voltage response of n = 6 NOS2 ACs to Local (magenta) Global (black) or Differential (cyan) static (open markers, first 1s of stimulus) or drifting (filled marker, subsequent 5s of stimulus) gratings. (B) Average voltage response over corresponding portion of static or drifting stimulus. * indicate $p < 0.05$ Student's t test

DISCUSSION

NOS2 ACs are an understudied population of retinal interneurons

The results demonstrate that LMD GC global motion suppression in part arises from NOS2 AC inhibitory input. We found that activating NOS+ ACs with a ChR2 approach drove inhibitory input directly to LMD GC dendrites, and LMD GCs received stronger postsynaptic inhibitory input during global motion than during local or differential motion. Retinal amacrine cells are known to play important roles in generating ganglion cell feature selectivity, but most of the ~60 types of ACs have poorly characterized receptive fields and connections with output channels (Macosko et al., 2015; Yan et al., 2020). This is in large part due to the difficulty in targeting individual types for repeated study of their presynaptic inputs and synaptic outputs. With new tools in genetic labeling, one can target and activate specific cell types. We targeted NOS2 ACs, a genetically identified wide-field AC (Zhu et al., 2012; Jacoby and Schwartz 2018) in which Cre recombinase is expressed in nNOS+ interneurons for functional analysis.

We found NOS2 ACs discriminate between global and local motion by responding to global objects with stronger depolarization than to narrow-field objects. However, they fail to distinguish between differential global motion, responding with similar amplitude to both of these wide-field stimuli (Figure 2.10). NOS2 AC preference for wide-field stimuli which was also observed in responses to static spot stimuli (Figure 2.4) likely is due to the recruitment of local inhibition that is itself suppressed at large spatial frequencies, and the summation of excitatory inputs at medium to wide-field diameters (Figure 2.6), which fail to depolarize the NOS2 cell at small stimulus diameters (Figure 2.4).

Given the observed colocalization of NOS2 AC dendritic arbors and the bulk of LMD GC arbors in SL3 of the IPL (Figure 2.1 and Zhu et al., 2014; Zhang et al. 2012), as well as the lack of overlap between the NOS1 AC dendritic and axonal arbors in SL1/SL5 (Figure 2.1 and Zhu et al, 2014; Park et al. 2020), we tested for any input from NOS2 ACs to LMD GCs with a NOS-CreER; ChR2-YFP genetic activation strategy and found a blue light evoked IPSC in LMD GCs. (Figure 2.3) Previous studies of the NOS2 AC either only looked at sparse labeling of nNOS-Cre expressing cells (Zhu et atl. 2014) or looked at the role of nitric oxide (NO) in coupling and uncoupling NOS2 ACs from one another (Jacoby et al. 2018). This study is the first to identify a GABAergic input from NOS2 ACs to an output neuron in the retina.

Receptive field structure comparison of LMD GCs and NOS2 ACs

Other studies targeting a similar group of GCs, the W3-RGCs, which are genetically identified by a BAC transgenic strategy in the THW3-GFP reporter line, which likely overlap considerably with the LMD GCs studied here, receive both pre and postsynaptic inhibition (Zhang et al., 2012; Kim and Kerschensteiner 2017). Kim and Kerschensteiner 2017 identified the TH-2 AC as a source of 40-60% of postsynaptic inhibition under certain conditions in this circuit. Specifically, the motion stimulus used in the TH-2 study did not include differential motion, and the local and global motion stimuli tested were brief translations (500 ms) of narrow gratings, separated by long adapting intervals (2-5s) of static grating presentation. We found that static adapting grating presentation for just 1s led to pronounced rebound spiking during the first 500ms of our drifting stimulus, which led us to use a longer time window of motion. This does not discredit the finding that removing TH-2 AC's ability to package GABA into vesicles impacts inhibition of W3-RGCs, but it does warrant the caveat that it was only tested under brief motion after a long adapting window. Additionally, the anatomical and functional identification strategy used in this study to target LMD GCs may not lead to the same group of GCs studied, so LMD and W3 GCs may not be directly comparable. However, there is likely a large degree of overlap between the populations based on similar light responses and anatomy of the two groups.

A study conducted by Jacoby and Schwartz in 2018 used a similar functional-anatomical strategy to study narrow-field SL3 laminating GCs and found four similar types with slightly different RF properties, suggesting that a transgenic approach may oversimplify the cell type identification of GCs. Of the four populations of GCs studied by Jacoby and Schwartz, two had similar patterns of pre and postsynaptic inhibition to the LMD GCs studied here. (Figure 2.4, Figure 2.5) The UHD, and HD 1 GCs showed narrow ON-OFF excitation with strong presynaptic suppression during static flicker stimulus. They also displayed postsynatpic inhibition that had a similar spatial arrangement to the LMD GCs studied here, with ON-OFF IPSCs displaying no surround suppression. Anatomically both the UHD and HD1 GCs have strong similarities to the LMD GCs studied here, but the z-axis resolution used in both studies leaves some ambiguity to what cell type they align with from higher resolution structural studies using serial block-face electron microscopy studies (SBEM) (Helmstaedter et al., 2013, Eyewire dataset, museum.eyewire.org).

The LMD GCs we studied likely represent a mixed population of the UHD and HD1 GCs from the Jacoby and Schwartz study. That study looked at normalized spiking output during a white noise stimulus drifting in different directions in the center and surround region of the UHD and HD1 GC's receptive field. They found the UHD GCs were poorly activated by differential motion, whereas the HD1 GCs responded equally well to center only and differential motion. This presents an interesting interpretation of the differential motion response we found in Figure 2.9. LMD GCs displayed an intermediate preference for differential motion. If the population of LMD GCs was split between UHD and HD1 GCs, an intermediate spiking response would be expected. Further studies should be done to further divide the inhibitory input from NOS2 ACs and any other AC input to local motion sensitive GCs to determine if there are clear cell type differences among connected GCs.

The postsynaptic inhibition during static flicker stimulus observed in Figure 2.4 could in some part be driven by the NOS2 AC is providing some of this postsynaptic inhibition, but based on the spatial tuning of the LMD GC spiking response shown in Figure 2.5, presynaptic mechanisms of surround suppression appear to dominate the output of the LMD GC. With that in mind, we asked what might the inhibitory input we observed from ChR2 driven activation of

NOS+ ACs in Figure 2.3 be doing to shape the receptive field structure of the LMD GC? We presented static and moving grating stimuli to LMD GCs and recording their spiking output as well as excitatory and inhibitory conductance and found that postsynaptic inhibition drove the motion selective response in LMD GCs.

Postsynaptic inhibition dominates LMD GC response to global motion

We found a much stronger postsynaptic inhibitory mechanism present during global motion than local motion. This is clear when comparing the similar G_{EXC} during the drifting portion of the grating stimulus to the strong potentiation of G_{INH} during global motion. This suggests that whatever is driving this increased global motion inhibition is not the same mechanism as was observed to generate the largely pre-synaptic surround driven by static full field stimuli. This suggests the pre-synaptic inhibitory input is poorly activated by a textured surround, whereas the postsynaptic mechanism is able to provide strong lateral inhibition during contrast reversing drifting gratings. Indeed, when global and local motion stimuli were used to activate NOS2 ACs, we found they were more strongly activated during global than local motion (Figure 2.10). Of note is the failure of NOS2 ACs to distinguish between differential and global motion, suggesting that these wide-field ACs are integrating full-field stimuli over a large area independent of stimulus orientation. The fact that LMD GCs receive less postsynaptic inhibition during differential motion than global motion suggests there are other sources of postsynaptic inhibition that are less well activated by differential motion, and the total inhibitory conductance is a mixture of these populations of inhibitory inputs. As mentioned earlier, Jacoby and Schwartz showed that the UHD GCs were poorly activated by differential motion while the HD1 GCs were strongly activated by it. Their motion stimuli were slightly different than the ones used here (drifting textures instead of drifting gratings were used), but the result in Figure 2.9 of an intermediate level of spike suppression during differential motion is commensurate with the LMD GCs studied here being a mixture of these two types of similar anatomical cell types. This tells us that a single AC (the NOS2 AC) can inhibit multiple groups of GCs, and may be important in generating global motion suppression, but a different source of inhibition lends the HD1 GCs their ability to respond to differential motion.

MATERIALS AND METHODS

Electrophysiology

Adult mice of either sex were dark adapted for 1–2 h. Animals were anesthetized with isoflurane before being euthanized via cervical dislocation. Subsequent to enucleation, all procedures were performed under infrared illumination. The retina and attached pigment epithelium were dissected free from the sclera and placed in a recording chamber under a microscope and continuously perfused (5ml/min) with Ames medium maintained at 34C. Cells were visualized through a 40X water-immersion objective and Dodt contrast illumination. Fluorescent nNOS+ ACs were targeted under 2-photon guidance (excitation wavelength: 920 nm) with a Ti:sapphire laser (Chameleon ultra II; Coherent). Cell type identities were confirmed by characteristic neurite arbor morphologies visualized by 2-photon imaging of Alexa 488 or 594 (1 mM) included in the intracellular solution at the end of each recording. LMD GCs were also delineated from other small arbor GCs by their preference to small diameter spot stimuli and longer response latency to small spots of light (Jacoby and Schwartz, 2017). Patch electrodes were pulled from borosilicate glass to a final resistance of 8-12 MΩ. For voltage-clamp recordings, pipettes were filled with an intracellular solution containing the following (in mM): 125 Cs-methanesulphonate, 7 CsCl, 10 Na-HEPES, 3 phospho- creatine-Na2, 1 EGTA, 2 Mg-ATP, 1 Na-GTP, 0.1 Alexa Fluor 488 hydrazide, and 3 QX-314 chloride. The solution was adjusted to pH 7.35 using CsOH. Cesium was included in place of potassium to block voltage-gated potassium currents, thereby improving the voltage clamp at positive potentials. QX-314 was included to block voltage-gated sodium channels. For current-clamp recordings, all solution components were the same except potassium was used in place of cesium, and QX-314 was not included. Currents were sampled at 10 kHz and filtered at 2 kHz through the four-pole Bessel filter in an EPC-10 patch clamp amplifier (HEKA). Voltages were corrected for a liquid junction potential of -10mV.

Visual stimulation

Visual stimuli were produced using custom software based on PsychoPy routines (Peirce, 2007). The stimuli, generated on a Texas Instruments digital light projector (DLP; Lightcrafter 4500), or a modified iPad monitor (product number) were projected onto the photoreceptor layer through a 10x water immersion objective (0.3 NA, Olympus). The DLP or iPad monitor intensity was linearized using a calibrated lookup table. DLP intensity was attenuated using neutral density filters to produce a gray adapting background flux of ~3.4 X 10^5 photons/μm^2/s. Stimuli were first aligned to the receptive field center of each cell using a series of 100 x 1000 μm vertical and horizontal bars to locate the cell's maximal response. All subsequent stimuli were centered on the coordinate of maximum response. Receptive field sizes were estimated from area- response data and fit to a difference of Gaussians function:

$$\boxed{\sqrt{R = K_c e^{-(d/\sigma_c)^2} - K_s e^{-(d/\sigma_c)^2}}}$$

where R is the peak response evoked by a stimulus of diameter d, K_c and K_s are the amplitudes of the excitatory and inhibitory components, respectively, and σc and σs are their space constants. Drifting gratings were set to a spatial period of 150 μm at a 1 hz drift rate and the center diameter for local motion was set to 150 μm. Differential motion stimuli were identical to global motion stimuli apart from the rotation of the center window by 90^o.

Pharmacological Agents

Drugs were added to the perfusion solution. The following agents were used: L-(+)-2-amino-4-phophonobutyric acid (L-AP4; 20 mM; Tocris Bioscience, catalog #0103), 1-(4-aminophenyl)-3-methylcarbamyl-4-methyl-3,4-dihydro-7,8-meth- ylenedioxy-5H-2,3-benzodiazepine hydrochloride [GYKI-53655 (GYKI); 50 mM;Tocris Bioscience catalog #2555), (*S*)-1-(2-Amino-2-carboxyethyl)-3-(2-carboxy-5-phenylthiophene-3- yl-methyl)-5-methylpyrimidine-2,4-dione (ACET; 1 mM; Tocris Bioscience, catalog #2728). 6- imino-3-(4-methoxyphenyl)-1(6H)-pyridazinebutanoic acid hydrobromide (SR-95531 (SR; 20 μM)) Tocris Bioscience catalog #1262.

Data Analysis

Light-evoked synaptic conductance was calculated as described previously (Taylor and Vaney, 2002). Briefly, current–voltage (I–V) relations were measured at 10 ms intervals over a range of voltage steps from 90 +50 mV in 20mV increments. The total light-evoked conductance was calculated as the difference between the I–V relation at each time point and the ‘‘leak’’ I–V relation measured just before the onset of the light stimulus. To avoid errors in calculating the net light-evoked currents due to a sloping baseline during positive voltage steps, a single exponential trend was subtracted from the current traces for each voltage step before the leak sub- traction. The excitatory and inhibitory conductance could then be calculated at each time point using the observed I–V reversal potential along with the cation and chloride reversal potentials. For frequency tuning data, the discrete Fourier transform was calculated at the stimulus frequency to obtain the magnitude of the fundamental component (F1). Error bars in figures represent +/- the standard error of the mean, as do the shaded areas on the current and voltage traces. Normally distributed data sets were compared using two-tailed Student’s *t* tests.

Results were considered significant for $p < 0.05$. For vertical sections fluorescent intensity profiles were acquired from 14 µm thick cryo-sectioned retinal slices**.** For whole mount single cell fill fluorescent intensity profiles z-stacks with 0.25 to 2 µm thick optical sections were taken through the inner retina (INL-GCL) and orthogonal projections were used for analysis in image j's z-axis profile tool before being imported into igor for normalization to ChAT and nNOS signal peaks.

Immunohistochemistry

After electrophysiology recordings, retinas were immersion-fixed for 20 minutes in 4% paraformaldehyde in 0.1M phosphate buffered saline (PBS), rinsed, pre-incubated in PBS with 5% normal horse (or is it donkey?) serum and 0.5% triton (blocking solution) for 1h at room temperature, then incubated in modified blocking solution (1% normal horse serum and 0.1% triton) for 24 hours at room temperature. Antibodies were used against goat anti-ChAT (1:500) (Millipore AB144P), and goat anti-nNOS (1:1000) (abcam 1376). Secondary antibodies were Alexa Fluor conjugates (1:800) (Alexa 488-Molecular Probes A-11055, and Alexa 594-abcam ab96933). For single cell fill recoveries 0.4% neurobiotin (Vector Laboratories SP-11020) was included in the recording pipet and 10 µg/mL Streptavidin Alexa Fluor 488 (Molecular Probes S-32354) conjugate was added to the primary AB incubating solution. Before imaging, stained retinas were washed three times in 1 x PBS before being mounted on a glass coverslip. For vertical sections, enucleated retinas were fixed in the same manner as tissue for whole-mount staining, but was first sucrose protected in a 30% Sucrose solution in PBS before freezing and sectioning into 14 µm thick cryosections and subsequent staining.

Chapter 3: Gbx2 Identifies two Amacrine Cell Subtypes with Distinct Molecular, Morphological, and Physiological Properties

Patrick C. Kerstein[1], Joseph Leffler[2,3], Benjamin Sivyer[4,5], W. Rowland Taylor[2], Kevin M. Wright[1,4]

1 Vollum Institute, Oregon Health & Science University, Portland, OR 97239; 2 School of Optometry & Helen Wills Neuroscience Institute, University of California-Berkeley, Berkeley, CA 94720; 3 Neuroscience Graduate Program, Oregon Health & Science University, Portland, OR 97239; 4 Department of Ophthalmology, Casey Eye Institute, Oregon Health & Science University, Portland, OR 97239; 5 Department of Chemical Physiology and Biochemistry, Oregon Health & Science University, Portland, OR 97239

This manuscript is presented as published in:

Kerstein PC, Leffler J, Sivyer B, Taylor WR, Wright KM. "Gbx2 Identifies Two Amacrine Cell Subtypes with Distinct Molecular, Morphological, and Physiological Properties." Cell Reports 2020 Nov 17;33(7):108382.

PREFACE

How do interneurons contribute to a circuit's transformation of an input into an emergent property of a larger circuit? This is not a trivial question to address in most central circuits. The massive interconnectivity of different brain regions rules out a sharp definition of a given circuit's input and/or output. Additionally, identifying individual interneurons or principal cell types for analysis has been a major challenge until recent advancements in cell-specific identification and targeting. Single-cell transcriptomic studies and deeper RNA sequencing of central circuits has revealed a greater diversity of interneurons than previously thought. Given the abundance of interneuron types in the retina and its isolation from central circuit feedback, the retina provides a tractable model system to understand what computations microcircuits are capable of. What we learn from dissecting microcircuits in the retina, particularly regarding diverse interneuron function, will be invaluable to our understanding of the brain.

Our model system of the retina combined with genetic tools, particularly the Gbx2$^{CreERT2-IRES-EGFP}$ mouse line, allow us to study two specific interneuron populations, the S3 and S5-laminating Gbx2+ ACs. There has been almost no previous study of these populations and this study presents the first detailed characterization using the Gbx2^{CreER} labeling strategy to study the structure and function of these interneurons. This study was conducted a collaborative project under the mentorship and guidance of Dr. W. Rowland Taylor (W.R.T.), Dr. Kevin M. Wright (K.M.W), and Dr. Benjamin Sivyer (B.S). The study was designed and the manuscript was written as a group by Dr. Patrick C. Kerstein (P.C.K), myself, B.S, W.R.T., and K.M.W. P.C.K performed and analyzed the morphological and molecular components of the study, B.S., provided the tracer coupling data and analysis, and I performed the functional experiments and analysis. Not every experiment I performed on these two populations of AC was not included in the manuscript published in Cell Reports in 2020. Some of the unpublished data have been included in the addendum to this chapter following the methods section.

ABSTRACT

Our understanding of nervous system function is limited by our ability to identify and manipulate neuronal subtypes within intact circuits. We show that the *Gbx2*$^{CreERT2\text{-}IRES\text{-}EGFP}$ mouse line labels two amacrine cell (AC) subtypes in the mouse retina that have distinct morphological, physiological, and molecular properties. Using a combination of RNAseq, genetic labeling, and patch clamp recordings, we show that one subtype is GABAergic that receives excitatory input from On bipolar cells. The other population is a non-GABAergic, non-Glycinergic (nGnG) AC subtype that lacks expression of standard neurotransmitter markers. Gbx2+ nGnG ACs have smaller, asymmetric dendritic arbors that receive excitatory input from both On and Off bipolar cells. Gbx2+ nGnG ACs also exhibit spatially restricted tracer coupling to bipolar cells (BCs) through gap junctions. This study identifies a genetic tool for investigating a two distinct AC subtypes, and provides a model for studying synaptic communication and visual circuit function.

INTRODUCTION

The mammalian nervous system is comprised of hundreds of distinct neuronal subtypes that form precise connections with one another. Neuronal subtypes can be defined by a combination of their morphological, physiological, and molecular properties (Zeng and Sanes, 2017). Recent single cell RNA sequencing (scRNAseq) approaches have greatly expanded the catalogue of neuronal subtypes based on transcriptional profiles (Macosko et al., 2015; Saunders et al., 2018; Tasic et al., 2018). However, linking the morphological and physiological properties of neuronal subtypes to their molecular profile and identifying their function within neural circuits remains a major challenge.

The retina is an ideal system to address such questions. It contains a complete neural circuit organized in a highly stereotyped manner within a compact space. Three classes of excitatory neurons—photoreceptors, bipolar cells (BCs), and retinal ganglion cells (RGCs) — connect in sequence to sense light and transmit this sensory information to the brain. Two classes of inhibitory neurons—horizontal cells and amacrine cells — increase the feature selectivity of these sensory signals by providing spatial and temporal regulation of excitatory cell activity (Diamond, 2017). Within these 5 classes, there are over 120 distinct neuronal subtypes (Macosko et al., 2015; Rheaume et al., 2018; Sanes and Masland, 2015; Shekhar et al., 2016; Tran et al., 2019; Yan et al., 2020). This high level of diversity reflects the enormous amount of computation necessary to encode up to 40 distinct representations of the visual field (Baden et al., 2016).

Amacrine cells (ACs) exhibit the greatest diversity in number and variance between subtypes. Morphological analysis of ACs predicts there are ~45 AC subtypes (Badea and Nathans, 2004; Helmstaedter et al., 2013; Lin and Masland, 2006; MacNeil et al., 1999) while recent single cell transcriptomic analysis predicts more than 60 distinct AC types (Peng et al., 2019; Yan et al., 2020). The data from these scRNAseq studies can provide potential markers for identifying neuronal subtypes in mouse (Macosko et al., 2015; Rheaume et al., 2018; Shekhar et al., 2016; Tran et al., 2019) and primate retinas (Peng et al., 2019). AC subtypes display characteristic specializations evident in their selective synaptic connectivity and neurotransmitter release. The dendritic morphology and stratification of an AC subtype determines its receptive field size and dictates the potential pre- and postsynaptic partners within the inner plexiform layer (Diamond, 2017; MacNeil and Masland, 1998). Two broad groups of AC subtypes are defined by their expression of either glycine or GABA. In addition to the inhibitory neurotransmitter, some AC subtypes co-release an excitatory neurotransmitter, for example, glycine and glutamate (Haverkamp and Wassle, 2004; Johnson et al., 2004; Lee et al., 2014) or GABA and acetylcholine (Brecha et al., 1988; Vaney and Young, 1988). Other ACs also release neuromodulators like dopamine (Newkirk et al., 2013) or neuropeptides (Zalutsky and Miller, 1990). Furthermore, in addition to neurochemical signaling, AC subtypes can form electrical synapses via gap junctions with BCs, RGCs, and other ACs (Bloomfield and Volgyi, 2009; Vaney and Weiler, 2000). Despite this broad functional and morphological diversity, most AC subtypes have not been thoroughly characterized due to a lack of genetic tools to prospectively identify and manipulate them.

Here we identify two AC subtypes that are genetically labeled by a mouse line expressing tamoxifen-inducible *Cre* recombinase from the endogenous locus of the transcription factor *Gbx2* (*Gbx2*$^{CreERT2\text{-}IRES\text{-}EGFP}$). We use this genetic tool to define the distinct morphological, physiological, and molecular properties of the two AC subtypes. S5-Gbx2+ ACs have larger dendritic arbors that stratify in S5, receive inputs exclusively from On type BCs, and are GABAergic. In contrast, S3-Gbx2+ ACs have smaller, dense, asymmetric dendritic arbors that stratify in S3, receive input from both On and Off BCs, and are non-GABAergic non-Glycinergic (nGnG) ACs. S3-Gbx2+ AC subtypes also exhibit exclusively heterotypic tracer coupling to BCs, suggesting they communicate in part through electrical synapses.

RESULTS

Gbx2$^{CreERT2\text{-}IRES\text{-}EGFP}$ marks two distinct amacrine cell subtypes

To begin unraveling the neuronal subtype complexity in the retina, we sought to identify *Cre* or *CreERT2* mouse lines that could be used as genetic tools to selectively label and manipulate single neuronal subtypes in the retina. Using scRNAseq datasets and transgenic mouse databases as a guide (Macosko et al., 2015; Siegert et al., 2009), we identified *Gbx2*$^{CreERT2\text{-}IRES\text{-}EGFP}$ as a mouse line predicted to label a sparse population of neurons in the retina (Chen et al., 2009). Since the *CreERT2-IRES-EGFP* cassette is knocked into the *Gbx2* locus, labeled neurons are expected to faithfully recapitulate its endogenous expression pattern. Crossing the *Gbx2*$^{CreERT2\text{-}IRES\text{-}EGFP}$ line to multiple Cre-dependent reporter lines labeled neurons in the inner nuclear layer (INL, Figure 3.1A) and the ganglion cell layer (GCL, Figure 3.1B). Low doses of tamoxifen (<0.02mg) labeled neurons in both the INL and GCL with dendrites that selectively stratify in sublamina 3 (S3) of the inner plexiform layer (IPL). When we used a saturating dose of tamoxifen (2.0 mg/day for 2 days, Figure 3.S1D-I), we labeled a second neuronal subtype with dendrites that stratify in sublamina 5 (S5) of the IPL (Figure 3.1C, G). Importantly, the same two neuronal populations were labeled whether tamoxifen was administered at embryonic (E16), postnatal (P0-2), or adult (P28) ages (Figure 3.S1A-C), demonstrating that the *Gbx2*$^{CreERT2\text{-}IRES\text{-}EGFP}$ line provides a consistent and stable tool for genetically labeling the same neuronal populations from embryonic to adult stages.

Both the S3- and S5-stratifying Gbx2+ populations co-localized with pan-amacrine cell markers TFAP2 and Pax6 (Figure 3.1D, H, Figure 3.S2A), and lacked expression of the retinal ganglion cell marker RBPMS and bipolar cell marker Chx10 (Figure 3.1H, Figure 3.S2B-C). GFP expression could be detected in 55.3% of the total Gbx2/tdTomato+ population (Figure

3.1E, I). A second marker, calretinin, labeled 53.6% of the total Gbx2+ ACs (Figure 3.1F, I) and nearly all (94.9%) of the GFP+ Gbx2+ ACs were co-labeled by calretinin (Figure 3.1J). Both GFP and calretinin label the S3 sublamina of the IPL, whereas S5 is negative for both GFP and calretinin (Figure 3.1E-G). Some retinal neuron subtypes, such as starburst amacrine cells, organize in regularly spaced mosaics, while many others do not (Keeley et al., 2020). Both S3- and S5-stratifying Gbx2+ populations fall into this latter category, forming irregular mosaics in the INL and GCL (Figure 3.S3A-K). The GFP+/Calretinin+ S3-stratifying subtype was present at a slightly higher density than the GFP-/Calretinin- S5-stratifying subtype (Figure 3.S3I). The cell density of both subtypes was consistent across the different areas of the retina (Figure 3.S3L-N). These data suggest that *Gbx2*$^{CreERT2\text{-}IRES\text{-}GFP}$ labels two distinct AC subtypes: a GFP+/Calretinin+ population that stratifies in S3 and a GFP-/Calretinin- population that stratifies in S5 of the IPL.

S3- and S5-Gbx2+ amacrine cells have distinct molecular profiles

The transcriptomic profiles of related neuronal subtypes can provide clues into the molecular basis of the morphology, development, and function, as well as identify markers for distinguishing individual subtypes. We used genetic labeling with the *Gbx2*$^{CreERT2\text{-}IRES\text{-}EGFP}$ line to identify the molecular differences between S3- and S5-Gbx2+ ACs by performing bulk RNA-seq on Gbx2+ ACs isolated from P8 retinas of *Gbx2*$^{CreERT2\text{-}IRES\text{-}EGFP}$; *R26*$^{LSL\text{-}tdTomato}$ mice administered 25µg tamoxifen at P1. We used fluorescence activated cell sorting (FACS) to separate the S3-Gbx2+ AC (GFP+/tdTomato+) and S5-Gbx2+ AC (GFP-/tdTomato+) populations (Figure 3.S4). RNAseq was performed on these isolated populations and identified 18 and 67 differentially expressed genes (DEGs) enriched in S3- and S5-Gbx2+ ACs, respectively (Figure 3.2A, (GEO GSE157271). *Gbx2* was expressed 13-fold higher in the S3-Gbx2+ ACs versus the S5-Gbx2+

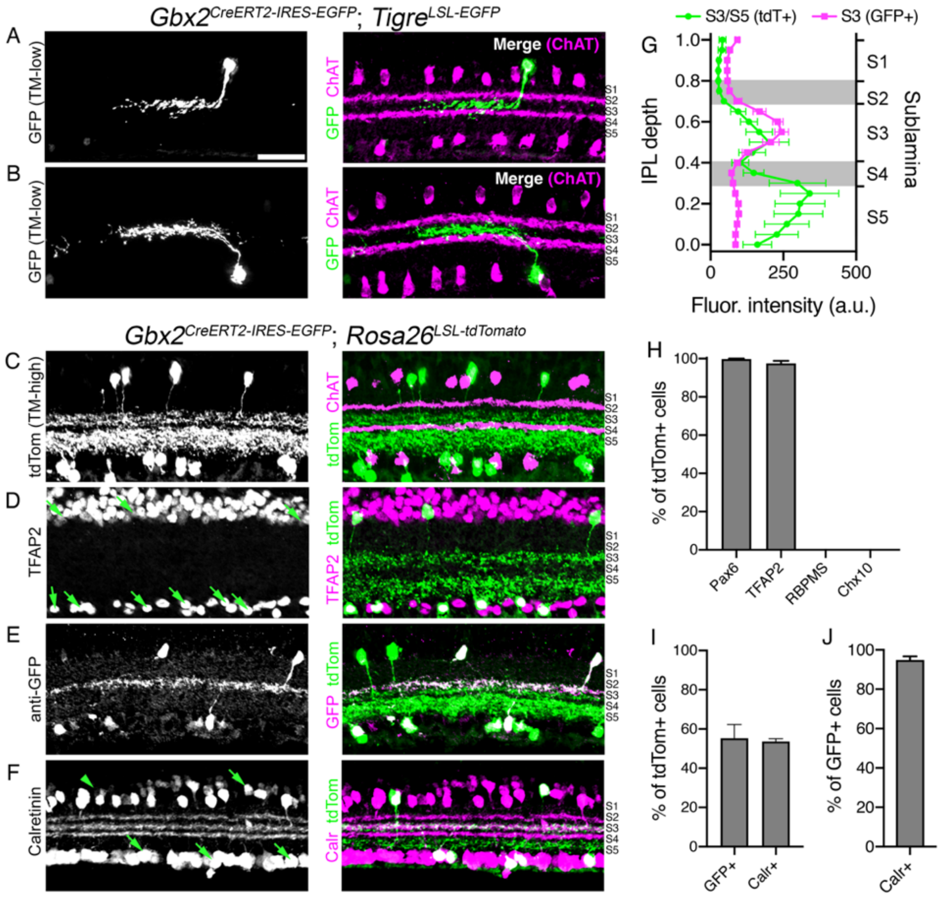

FIGURE 3.1 Gbx2$^{CreERT2-IRES-EGFP}$ Selectively Labels a Subtype of ACs in the Mouse Retina

(A and B) Left: cross-sections of adult retinas from a *Gbx2*$^{CreERT2-IRES-EGFP}$; *TIGRE*$^{TIT2L-GFP-ICL-tTA2}$ mouse labeling single Gbx2^{+} ACs (low-TM, 0.02 mg tamoxifen) in the (A) INL and (B) GCL. Right: merged image, choline acetyltransferase (ChAT; magenta, S2, S4), Gbx2-GFP (green, S3). (C) Cross-sections of an adult retina from a *Gbx2*^{CreERT2}; *Rosa26*$^{LSL-tdTomato}$ mouse labeling the total Gbx2^{+} AC population (high-TM, 2.0 mg tamoxifen). Right: merged image, ChAT (magenta) and Gbx2-tdTom (green, S3 and S5). (D–F) Left, retinal sections from a *Gbx2*$^{CreERT2-IRES-EGFP}$; *Rosa26*$^{LSL-tdTomato}$ mouse immunolabeled with (D) an AC marker TFAP2, (E) GFP, and (F) calretinin co- labeled with Gbx2^{+} tdTomato^{+} retinal neurons (green, right). (G) Fluorescent intensity plotted in IPL depth using ChAT bands in S2 and S4 as reference points. Magenta: Gbx2^{+} ACs detected by EGFP immunohistochemistry (n = 6 measurements, 3 retinas); green: Gbx2^{+} ACs detected by tdTomato labeling (n = 6 measurements, 3 retinas). (H) Quantification of the percentage of tdTomato^{+} cell co-labeling with AC markers Pax6 and TFAP2, retinal ganglion cell marker RBPMS, and bipolar cell maker Chx10. (I) Percentage of tdTomato^{+} cells co-labeling with GFP or calretinin. (J) Percentage of GFP^{+} cells co-labeling with calretinin. n = 4 measurements, 3 animals for each experiment in (H)–(J). Data represented as means ± SEMs. Scale bar, 25 µm. See also Figures 3.S1–S3

ACs (Figure 3.2B). Consistent with this result, *GFP* (driven from the endogenous *Gbx2* locus) was expressed at 10-fold higher in the S3-Gbx2+ ACs compared to the S5 subtype (Figure 3.2B).

Calretinin (*Calb2*), which distinguishes S3- and S5-Gbx2+ ACs by immunohistochemistry (Figure 3.1F-J), was expressed 19-fold higher in S3-Gbx2+ ACs (Figure 3.2B).

The majority of AC subtypes are categorized by their neurotransmitter profile as either GABAergic or glycinergic (Kay et al., 2011). Based on the RNAseq results, the GABAergic enzymes *Gad1* and *Gad2* are highly expressed in S5-Gbx2+ ACs (Figure 3.2C). In contrast, S3-Gbx2+ ACs were negative for all the standard neurotransmitter markers, including the GABAergic markers *Gad1*, *Gad2*, and the glycinergic markers *Slc6a9* and *Slc6a5* (Figure 3.2C). Both S3 and S5 subtypes expressed low levels of the glutamatergic marker, *Slc17a7*, however this is likely due to photoreceptor contamination. The neuropeptides *Tachykinin1* (*Tac1*) and *Corticotropin-releasing hormone* (*Crh*) were highly expressed in the S3- and S5-Gbx2+ subtypes, respectively (Figure 3.2C). To gain additional insight into the differences between S3- and S5-Gbx2+ ACs, we expanded our analysis to include transcription factors (Figure 3.2D), cell adhesion and axon guidance receptors (Figure 3.2E), and neurotransmitter receptors and ion channels (Figure 3.2F). The S3-Gbx2+ AC subtype expressed the transcription factors *Gbx2* and *Zfhx3* significantly higher than in the S5 subtype, whereas the S5 subtype selectively expressed *Id4*, *Lmo4*, *Tfap2c*, *Eomes*, and *Maf* (Figure 3.2D). Both S3 and S5-Gbx2+ AC subtypes expressed high levels of the transcription factors *Pax6*, *Meis2*, *Cux1*, and *Lhx9* (Figure 3.2D). The cell adhesion molecule *Pcdh8* was expressed significantly higher in the S3-Gbx2+ ACs, whereas *Pcdh19*, *Alcam*, *Lrrtm1*, and *Tenm1* were higher in the S5 subtype (Figure 3.2E). Both shared high expression of the adhesion receptor genes *Clstn1*, *Cadm1*, *Ncam1*, *Ptprs*, *Nrxn3*, and *Robo2* (Figure 3.2E). Unlike transcription factors and adhesion receptors, neurotransmitter receptors and ion channels showed little difference in expression between the two subtypes, with the exception of *Cacng3*, *Grm8*, and *Chrna2* genes showing significant enrichment in the S5 subtype (Figure 3.2F). These differentially expressed genes identify markers to distinguish the two Gbx2+ AC subtypes, and provide insight into the function of these cells, particularly with respect to neurotransmitter release.

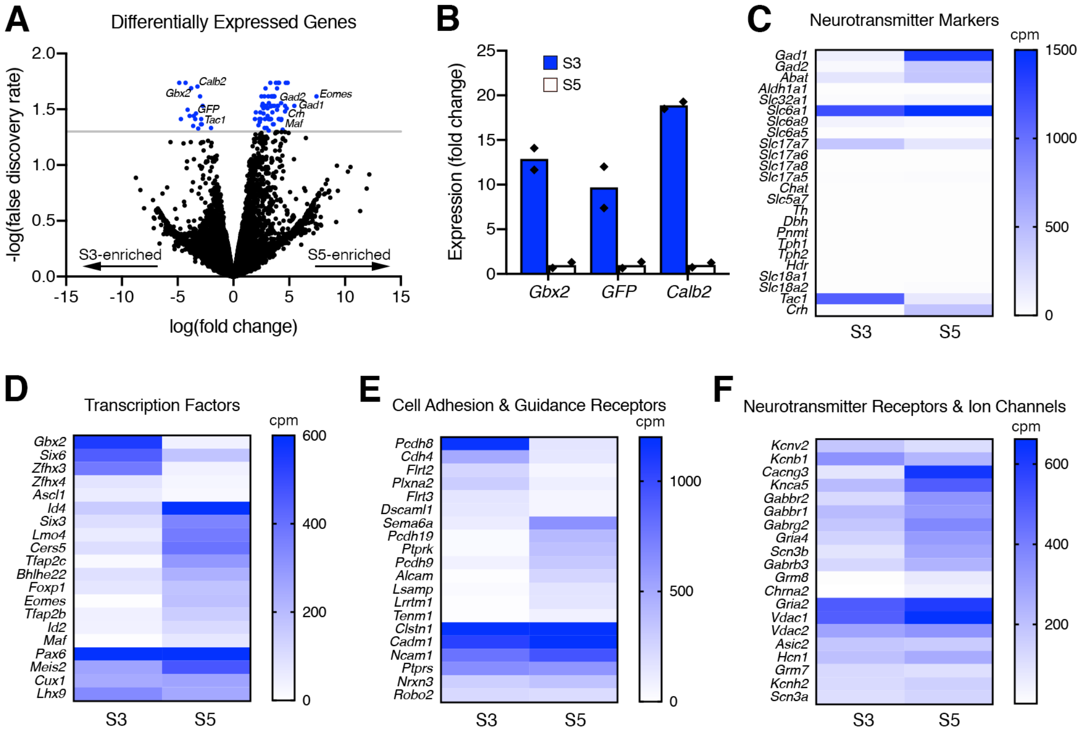

FIGURE 3.2 Transcriptomic Profiling of S3- and S5-Stratifying Gbx2$^+$ AC Subtypes Identifies Molecular Differences (A) Differentially expressed genes (DEGs) identified by RNA-seq between S3- and S5-Gbx2$^+$ ACs are displayed in a volcano plot (negative fold change, S3 enriched; positive fold change, S5 enriched). The blue points represent genes that have significant differences in between the S3- and S5- Gbx2$^+$ AC subtypes ($p < 0.05$, false discovery rate [FDR], gray line). (B) Fold change in expression determined by RNA-seq for known S3-specific markers in S3 (blue bars) and S5 (white bars) Gbx2$^+$ AC subtypes. Each point (black diamond) represents a single sample/animal. (C) The mean expression of neurotransmitter markers from RNA-seq between S3- and S5-Gbx2$^+$ ACs displayed in a heatmap. Neurotransmitter markers are subdivided into GABA synthesis (*Gad1*, *Gad2*, *Abat*, *Aldh1a1*), GABA transport (*Slc32a1*, *Slc6a1*), glycine transport (*Slc6a9*, *Slc6a5*), glutamate transport (*Slc17a7*, *Slc17a6*, *Slc17a8*, *Slc17a5*), cholinergic synthesis and transport (*Chat*, *Slc5a7*), catecholamine synthesis (*Th*, *Dbh*, *Pnmt*), serotonin synthesis (*Tph1*, *Tph2*), histamine synthesis (*Hdc*), monoamine transport (*Slc18a1*, *Slc18a2*), and neuropeptides (*Tac1*, *Crh*). (D and E) Heatmaps comparing the mean expression of highly and differentially expressed (D) transcription factors, (E) cell adhesion and axon guidance receptors, and (F) neurotransmitter receptors and ion channels. Cpm, counts per million reads. The data are represented as means. See also Figure 3.S4.

S3-Gbx2+ amacrine cells are non-GABAergic, non-Glycinergic (nGnG)

The majority of ACs (~85%) release either GABA or glycine to inhibit downstream postsynaptic neurons (Kay et al. 2011). Based on the RNAseq results, S5-Gbx2+ ACs express both *Gad1* and *Gad2* and are therefore GABAergic (Figure 3.2C). We confirmed this with immunohistochemistry, which showed that 28.4% of Gbx2+ ACs in the INL co-labeled with the GABAergic marker GAD67, while the remaining Gbx2+ ACs were negative for GAD67 (Figure 3.3A-C, H). The GAD67+/Gbx2+ ACs are likely S5-Gbx2+ ACs, as ~37% of all Gbx2+ ACs in the INL are the S5 subtype (Calretinin-/GFP-) (Figure 3.S3). Neither Gbx2+ AC subtype co-localized with the glycinergic marker, GlyT1/2 (Figure 3.3D-E, H). Therefore, S3-Gbx2+ ACs are a subtype of non-Glycinergic, non-GABAergic (nGnG) AC. These results are consistent with previous scRNAseq analysis that showed a cluster of ACs identified by their expression of Gbx2 lacked expression of *Slc6a9* or *Gad1/2* (Macosko et al., 2015; Yan et al., 2020). When we examined other neurotransmitter markers known to be expressed in specific AC subtypes, we found little (<1%) or no co-localization with Gbx2+ ACs (Figure 3.3H, Figure 3.S5), consistent with our RNAseq results (Figure 3.2C).

Previous studies have hinted at the presence of at least two nGnG AC subtypes (Cherry et al., 2009; Macosko et al., 2015; Yan et al., 2020). One nGnG AC subtype is defined by expression of the transcription factor *NeuroD6* (Kay et al., 2011). *NeuroD6*+ nGnG ACs have a narrow dendritic arbor that stratifies diffusely through multiple layers of the IPL, in contrast to the dendritic arbors of S3-Gbx2+ ACs, which have a medium sized arbor that is mono-stratified. To confirm that *Gbx2* and *NeuroD6* label different populations of nGnG ACs, we generated a *NeuroD6*^{Cre}; *Gbx2*$^{CreERT2\text{-}IRES\text{-}EGFP}$; *R26*$^{LSL\text{-}tdTomato}$ mice and found no overlap between the

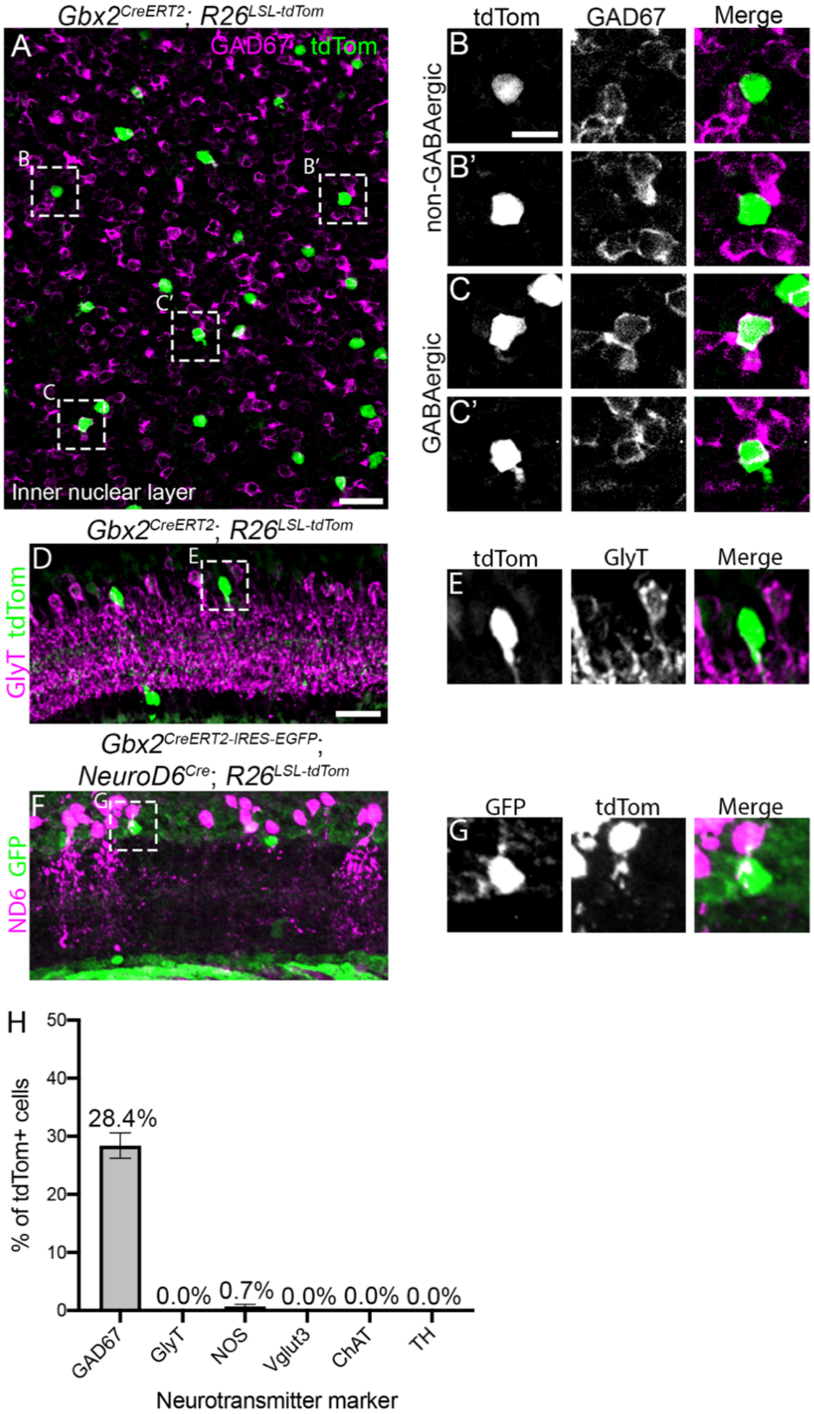

FIGURE 3.3 S3-Gbx2$^+$ Neurons Are a Subtype of non-GABAergic Non-glycinergic ACs

(A) Inner nuclear layer of an adult retina *en face* from a *Gbx2*^{CreERT2}; *R26*$^{LSL-tdTom}$ mouse immunolabeled for tdTomato (green) and GAD67 (magenta). (B and C) Magnified images of Gbx2$^+$ ACs from (A) that do not colocalize with GAD67 (B–B') and GABAergic Gbx2$^+$ ACs that colocalize with GAD67 (C–C'). (D and E) A retinal cross-section from a *Gbx2*^{CreERT2}; *R26*$^{LSL-tdTom}$ mouse shows no colocalization between Gbx2$^+$ ACs with GlyT1/2. (F) Gbx2$^+$ ACs (GFP, green) do not colocalize with NeuroD6$^+$ nGnG ACs (tdTom, magenta) in retinal sections from a *Gbx2*$^{CreER-ires-EGFP}$; *NeuroD6*^{Cre}; *Rosa26*$^{LSL-tdTomto}$ mouse. (G) Magnified image from (F) labeled with GFP (*Gbx2*, left), tdTomato (*NeuroD6*, center), and a merge image (right). (H) Quantification of the percentage of tdTomato$^+$ cells that colocalize with neurotransmitter markers. GAD67 quantification was performed in INL only. n > 125 neurons and 3 mice for each condition. The data represented are as means ± SEMs. Scale bar, 25 mm in (A), (D), and (F), 10 mm in (B), (C), (E), and (G). See also Figure 3.S5.

NeuroD6+ (tdTomato+) and Gbx2+ (GFP+) AC subtypes (Figure 3.3F-G). Therefore, S3-Gbx2+ ACs are a distinct subtype of nGnG AC

S3- and S5-Gbx2 ACs have distinct morphological properties

The dendritic morphology of a neuronal subtype is directly related to its function (Lefebvre et al., 2015). Dendritic shape and size are particularly important for the computations performed by AC subtypes, as dendrites contain both pre- and postsynaptic sites. We used the *Gbx2*$^{CreERT2\text{-}IRES\text{-}EGFP}$ line to define the morphological properties of S3- and S5-stratifying Gbx2+ ACs by two different sparse-labeling techniques: a genetic approach using low dose tamoxifen (0.05mg), or single-cell fills of Gbx2+ ACs with Neurobiotin (Figure 3.4A-D). S3-Gbx2+ ACs had an average dendritic arbor area of 10,331±629 μm^2 and total dendrite length of 1766±109 µm. S5-Gbx2+ ACs had significantly larger dendritic arbors, with an area of 44,643±11,699 μm^2 and length of 2800±401 µm (Figure 3.4E, Figure 3.S6A). S3-Gbx2 ACs had a significantly higher average dendrite and branch density of 117.8±16.9 branches/100 μm^2, compared to 34.3±12.9 in S5-Gbx2+ ACs (Figure 3.4F-G). We did not observe any difference between S3- and S5-Gbx2+ ACs in total number of branches (Figure 3.S6B), branch crossovers (Figure 3.S6C), or coverage factor (Figure 3.S6D).

Sparse labeling revealed that the dendritic arbors of S3-Gbx2+ ACs exhibited a clear asymmetry, with the arbor rarely exceeding 180 degrees (Figure 3.4H). As a population, S3-Gbx2+ ACs had a significantly lower symmetry index than S5-Gbx2+ ACs (Figure 3.4I). We analyzed the dendrite orientation of S3-Gbx2+ ACs at a population level and found that their asymmetric dendrites were consistently oriented in a dorsal-temporal direction (Figure 3.4J). Both dendrite asymmetry and orientation of S3-Gbx2+ ACs were consistent across all quadrants of the retina (Figure 3.S6E-F, G-J, respectively). Overall, these data show that S3- and S5-Gbx2+ ACs exhibit significantly different morphological features, supporting the hypothesis that they are distinct subtypes.

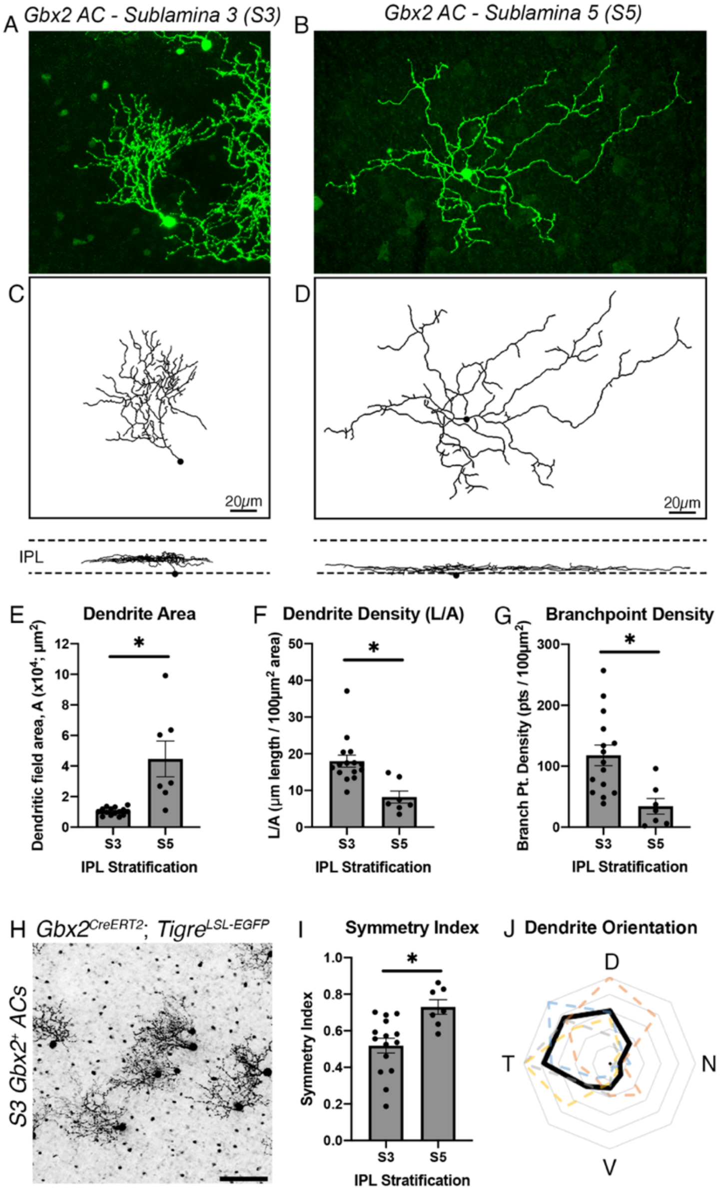

FIGURE 3.4 S3- and S5-Gbx2+ ACs distinct morphological features.

(A-B) Single cell labeling of a (A) S3 stratifying and (B) S5 stratifying Gbx2+ ACs using a $Gbx2^{CreERT2-IRES-EGFP}$; $TIGRE^{TIT2L-GFP-ICL-tTA2}$ mouse and neurobiotin-cell fill. (C-D) Dendrite morphology traces constructed using the Filaments plugin in Imaris software for the Gbx2+ ACs in (A) and (B) respectively. Below are the traces in the orthogonal view to display the stratifications of each neuron in the IPL. (E-G) S3- and S5-Gbx2+ AC morphology in (E) dendrite area (p=0.0003), (F) dendrite density (p=0.0015), (G) branchpoint density (p=0.0009). Morphological data was collected from 15 S3-Gbx2+ ACs (3 animals) and 7 S5-Gbx2+ ACs (4 animals). (H) Gbx2+ ACs sparsely labeled in a flat-mounted P21 retina in a $Gbx2^{CreERT2-IRES-EGFP}$; $TIGRE^{TIT2L-GFP-ICL-tTA2}$ mouse. (I) Quantification of dendritic arbor symmetry between S3- and S5-stratifying ACs (p=0.0039). (J) A polar plot of dendrite orientation of S3-targeting Gbx2+ ACs; black trace represents the mean and colored dashed traces represent neurons quantified from a single retina (n >20 neurons per retina, n= 4 retinas). The concentric gray rings represent the average percentage of neurons with dendrites extending in the specific orientation (outer most ring = 100%, 20% increments). Data represented as mean ± SEM. *p<0.05 by an unpaired t-test with Welch's correction. Scale bar, 20µm in (C, D), 50µm in (G). See also Figure 3.S6.

S3-Gbx2+ amacrine cells are tracer coupled to bipolar cells

Many amacrine cells show selective electrical coupling to other neurons, including bipolar cells, ganglion cells, and other amacrine cells (Bloomfield and Volgyi, 2009). Electrical synapses play a major role in the transmission of visual information in the retina (O'Brien and Bloomfield, 2018), and are typically revealed by filling cells with Neurobiotin, a small tracer molecule that is permeable through most gap-junctions (Vaney, 1991). When we filled genetically-labeled S3-Gbx2+ AC somas in the ganglion cell layer with Neurobiotin, we found that the tracer spread into a sparse number of neighboring retinal neurons with somas in the INL (Figure 3.5A-B). The coupled cells could be identified as bipolar cells based on their morphology in orthogonal optical sections (Figure 3.5G). At higher magnification we also observed tracer-filled bipolar cell axon terminals overlapping S3-Gbx2+ AC dendrites in the same optical section *en face* (Figure 3.5H). In contrast to the S3-Gbx2 ACs, S5-Gbx2+ ACs did not show consistent tracer coupling with other retinal cells (Figure 3.5J). The extent and strength of coupling in the retina is linked to the ambient light level through the release of the neuromodulator dopamine. Dopamine release increases as the background light-level increases (Hampson et al., 1992). The increased concentration of dopamine activates D1 receptors in all AII ACs, reducing their coupling to BCs. To determine whether S3-Gbx2+ AC to bipolar cell coupling is also modulated by dopamine, we measured coupling in the presence of the D1 receptor antagonist, SCH23390 (50µM). Inhibition of D1 receptors dramatically increased coupling to bipolar cells in 3 out of 8 S3-Gbx2+ ACs, while coupling in the remaining S3-Gbx2+

ACs was unaffected (Figure 3.5D-I). The specificity of tracer coupling was confirmed by bath application of the gap junction antagonist Meclofenamic acid (100µM MFA), which blocked coupling in both baseline and D1 receptor antagonist conditions (Figure 3.5I).

The coupling between S3-Gbx2+ ACs and bipolar cells show unusual spatial features. In other ACs, coupling typically occurs homotypically and spreads laterally to serve a signal averaging function (Bloomfield and Volgyi, 2009). In contrast, we never observed S3-Gbx2+ ACs coupled to neighboring S3-Gbx2+ ACs, and their coupling to BCs appeared to be spatially selective. BCs coupled to S3-Gbx2+ ACs were clustered towards the center of the dendritic arbor (Figure 3.5K). Even with addition of the D1R antagonist, bipolar cell coupling to Gbx2+ ACs never extended into the distal 20% of the dendrite arbor (Figure 3.5J). Inhibition of the D1 receptors did not unmask coupling between the S5-Gbx2+ ACs and other retinal neurons (Figure 3.5J).

Input differences between S3- and S5-Gbx2+ ACs

We next sought to characterize the intrinsic physiological properties of S3- and S5-Gbx2+ ACs. S3-Gbx2+ ACs cells stratify at the border between the On and Off sublamina of the IPL and thus potentially receive input from both On- and Off-type BCs. The S5-Gbx2+ ACs cells stratify within the On- sublamina, and are therefore likely to receive input from On-type bipolar cells. To test these predictions we recorded light evoked postsynaptic potentials (PSPs) from S3- and S5-Gbx2+ ACs. Genetically labeled Gbx2+ ACs were stimulated with light spots of 50 to 80% contrast, square-wave modulated at 2Hz, centered on the receptive field. The background intensity was set at a photopic level (10^3 photons/μm^2/s). Consistent with the stratification levels of their dendrites, S3-Gbx2+ ACs cells showed strong depolarization during both the On phase (increase in luminance) and Off phase (decrease in luminance) of the stimulus (black trace, Figure 3.6A, left). In contrast, S5-Gbx2+ ACs cells were depolarized only during the On phase, and are hyperpolarized during the Off phase (black trace, Figure 3.6A, right). Thus, the physiological inputs are consistent with the stratification level of the dendrites for both S3- and S5-Gbx2+ ACs.

S3- and S5-Gbx2+ ACs cells receive center and surround inhibition

In many retinal neurons the spatial structure of the receptive field is shaped by center/surround organization, in which illumination outside a neuron’s excitatory center receptive field elicits an antagonistic response. We presented spots with a range of diameters to test for differences between the spatial extent of the two cell types’ receptive fields. The largest spots suppressed center responses in both cell types. For S3-Gbx2+ ACs, maximal surround

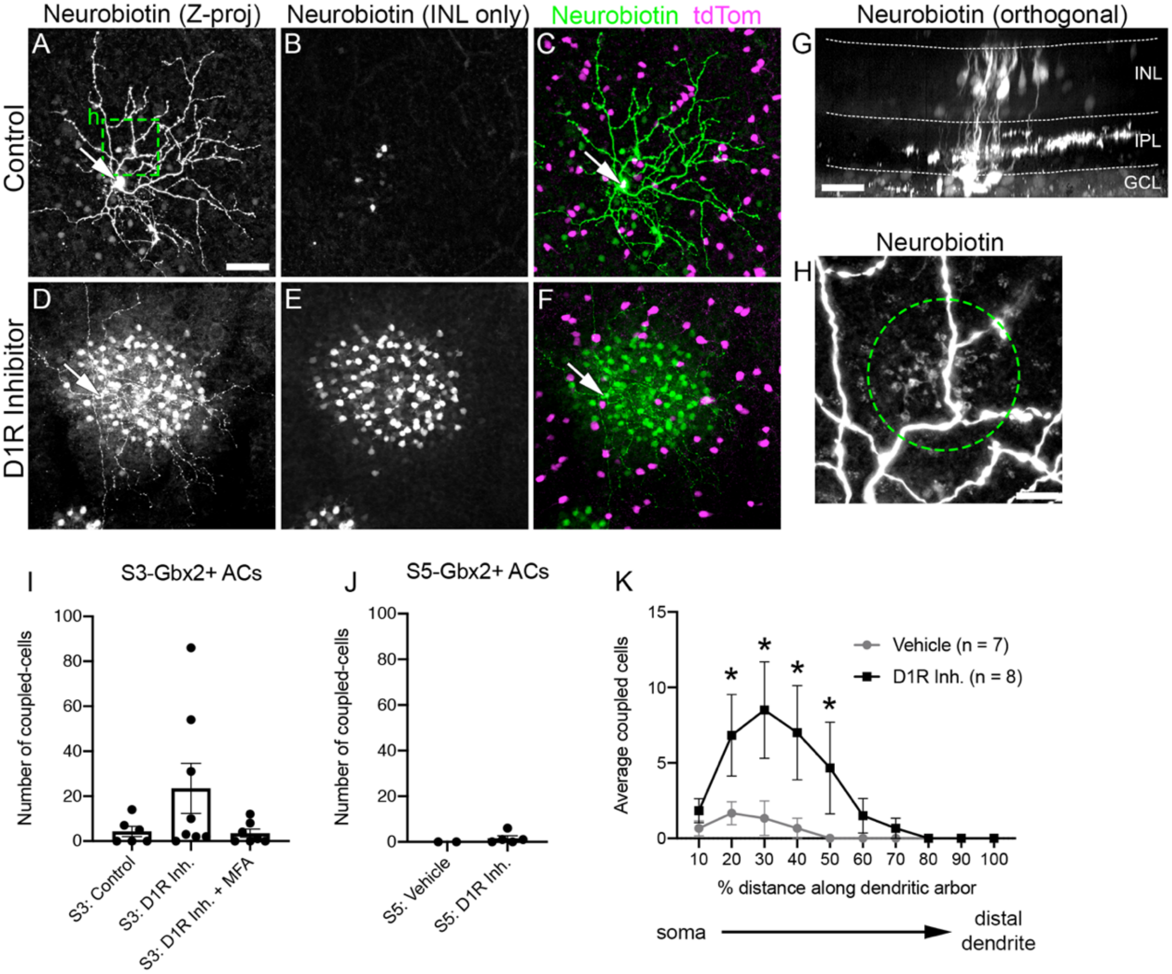

FIGURE 3.5 Gbx2+ ACs are electrically coupled to neighboring bipolar cells

Neurobiotin-filled S3-stratifying Gbx2+ AC (arrows, cell bodies) incubated in (A-C) vehicle and (D-F) D1 receptor inhibitor, 50µM SCH23390, in flat-mounted retinas. (A, D) Z-projection through the entire retina. (B, E) Z-projection through INL only. (C, F) Merged Z-projection with neurobiotin (green) and Gbx2+ ACs (magenta). (G) Orthogonal view of neurobiotin filled Gbx2+ AC (arrow) and dye-coupled bipolar cells (BCs). (H) Magnified image (box in a) of BC axon terminals (circle) co-localizing with a dendritic branch of neurobiotin-filled Gbx2+ AC. (I-J) Mean number neurons dye-coupled to a single (I) S3- and (J) S5-stratifying Gbx2+ AC (S3-Vehicle, n= 6 cell-fills; S3-D1R Inh., n=8; S3-D1R Inh. + MFA, n=7; S5-Vehicle, n=2; S5-D1R Inh., n=3; Welch's t-test). (K) The spatial distribution of dye-coupled cells to a single S3-stratifying Gbx2+ AC along its dendritic arbor. $^*p<0.05$ calculated by a Two-way ANOVA with multiple comparisons. Data represented as mean ± SEM. Scale bar, 50µm in A-G, 10µm in H.

stimulation suppressed On and Off PSPs equally by 86% (Figure 3.6A-B, left), whereas surround suppression was weaker in the S5-Gbx2+ ACs, reducing center PSPs by about 53% (Figure 3.6A-B, right). Activation of the surround had little effect on the amplitude of the hyperpolarization evoked during the OFF-phase of the stimulus (Figure 3.6B, left, filled symbols). The spatial extent of the center and surround were estimated at fixed time-points during the On and Off phase of the stimulus by fitting a difference of Gaussians (DOG) function to the amplitude of the responses. The On and Off responses of the S3 ACs showed essentially identical spatial tuning profiles, with the extent of the surround being about 2.5-fold wider than the center (Figure 3.6B, left). Maximum dendritic diameter averaged 181 ± 8 µm (n=17), as estimated from morphological analysis, which compares well with the physiological center size of ~145µm, estimated as the space constant from the DOG fit. The S5 ACs were more divergent. The maximum dendritic diameter averaged 258 ± 12 µm (n=27), while the physiological center size estimated during the On-phase was only ~110 µm (Figure 3.6B, right), and was smaller than the center size measured during the Off-phase (~180µm). A similar difference is apparent in a previous study (Park et al., 2018). To examine potential synaptic mechanisms providing surround antagonism, we recorded light evoked postsynaptic currents (PSCs) in response to center-only and full-field visual stimuli, and calculated the component excitatory and inhibitory inputs (Figure 3.6C-E). Excitation and inhibition were activated during the On and Off phase of the stimulus for S3-Gbx2+ ACs, and appeared to have very similar temporal dynamics (Figure 3.6E, left). The S5 ACs showed a similar pattern, with excitation and inhibition showing similar temporal wave-forms. However, while inhibition was slow to turn-off during the Off-phase, excitation declined more rapidly and dipped below zero (Figure 3.6E, right), presumably driving the hyperpolarization seen during the Off-phase in Figure 3. Comparison of the center-only and full-field responses provides insight into the mechanisms of surround antagonism. For the S3 ACs, excitation was suppressed and inhibition enhanced for full-field stimuli relative to center-only stimuli (Figure 3.6E, red vs black, left), suggesting that the antagonistic surround 6A.

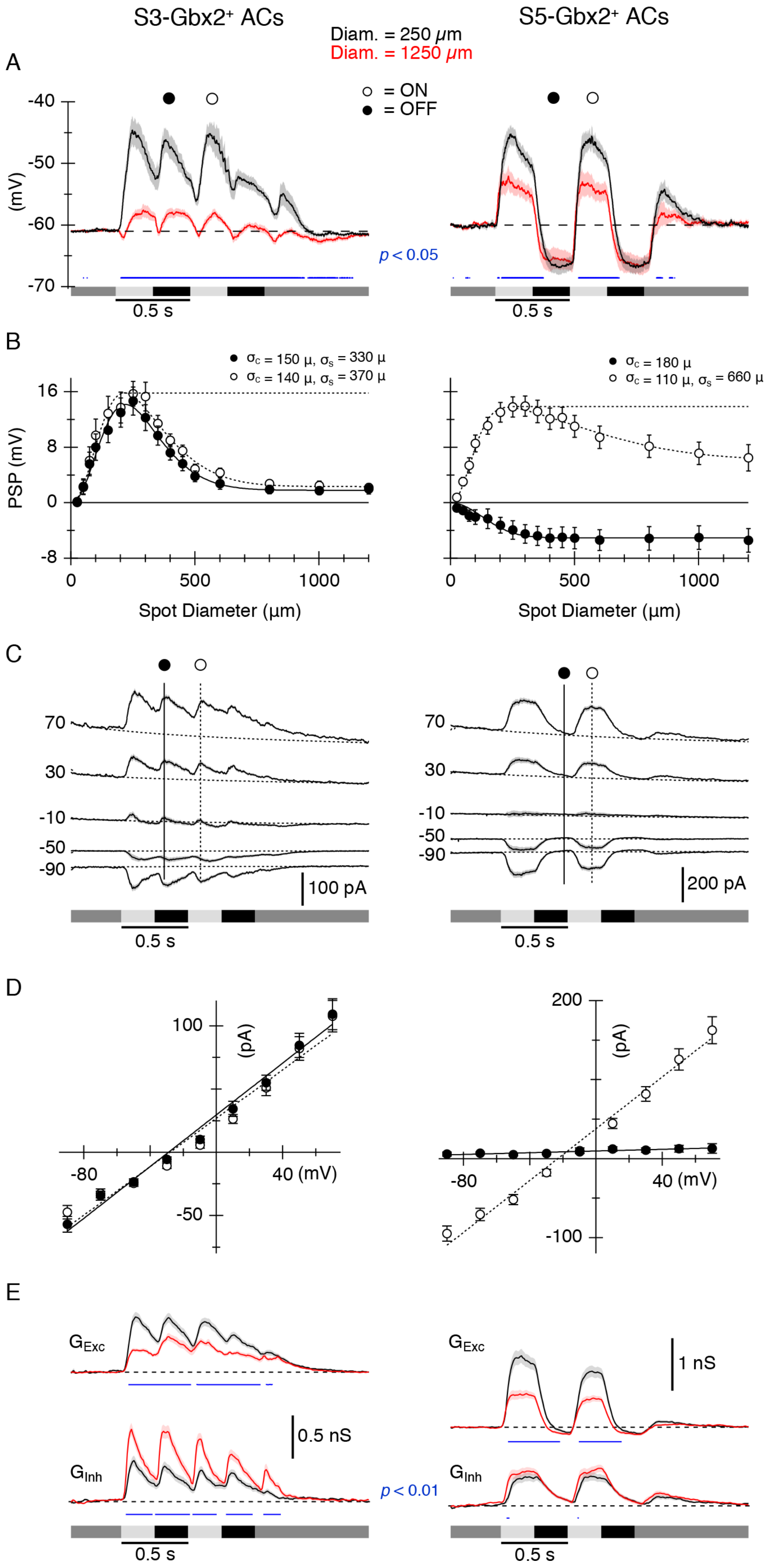

[**FIGURE 3.6** S3- and S5-Gbx2+ ACs exhibit distinct spatial receptive field properties and ON-OFF inputs]

(A) Average light-evoked postsynaptic potentials (PSPs) in S3 (n=12) (left) and S5 (n=17) (right) Gbx2+ ACs in response to a 250 μm (black) or 1200 μm (red) diameter spot stimulus. Luminance indicated by shaded bars underneath traces. (B) Area response functions from S3 (left) and S5 (right) cells measured as the amplitude of the PSPs versus stimulus diameter at indicated time points in (A). Surround suppression of PSPs was 86% for S3 and 53% for S5 cells. (C) Average light-evoked postsynaptic currents (PSCs) in (n=56) (left) S3 and (n=45) (right) S5 cells for center spot stimuli during a series of voltage steps from -90 to +70mV. (D) I-V relations for the PSCs at the time points indicated in *(C).* The dotted and solid lines show average least-squares fits to the I-V relations. (E) Average synaptic conductance traces calculated from fits to I-V relations measured every 10 ms during the light stimulus (see Methods). Traces and symbols represent average responses. Shading and error bars represent SEM. Blue traces in (A) and (E) indicate significant differences (paired t-test) between the solid and dashed data. P values indicated on panels.

shown in Figure 3.6A results from complementary changes in both excitation and inhibition. For S5 ACs, by contrast, activation of the surround suppressed only the excitation, and had no significant effect on the inhibitory input (Figure 3.6E, red vs black, right).

S3- and S5-Gbx2+ ACs receive distinct On and Off pathway excitation and inhibition

These data suggest excitation and inhibition may arise through both the On and Off pathway for S3-Gbx2+ ACs, but only the On pathway for S5-Gbx2+ ACs. Consistent with this hypothesis, when the On-pathway signaling was blocked by using a mGluR6 agonist L-AP4, to prevent depolarization of On-bipolar cells, light-evoked synaptic input to S5-Gbx2+ ACs was abolished (Figure 3.7A, right). In contrast, the light-evoked synaptic inputs to S3-Gbx2+ ACs during the On-phase of the stimulus were strongly suppressed, while the Off pathway excitation and inhibition were largely unaffected. (Figure 3.7A, left). Inhibition is in-phase with excitation during On and Off responses in S3-Gbx2+ ACs and during On responses in S5-Gbx2+ ACs suggesting that it could serve to regulate the gain of signaling by counterbalancing excitation.

The S3- and S5-Gbx2+ ACs show distinct Neurobiotin-coupling patterns to peri-somatic bipolar cells (Figure 3.5). To test whether these gap junction connections support significant, light-evoked electrical synaptic input to the ACs, we blocked glutamatergic inputs using a cocktail of antagonists, including the NMDA receptor antagonist D-AP5 (50µm), and the AMPA and Kainate receptor antagonists ACET and GYKI (1µM and 50µM). Under these conditions, mGluR6 mediated transmission in On-type bipolar cells is preserved, and if gap junctions mediate electrical transmission to S3- or S5-Gbx2+ ACs, excitatory On-responses in these cells should also be preserved.

However, light-evoked responses using stimulus spots large enough to activate all coupled bipolar cells are almost completely blocked (Figure 3.7B, magenta traces), suggesting that excitatory drive through any electrical synapses from the coupled BCs is functionally insignificant under these recording conditions. These experiments don't rule out the possible presence of functionally significant electrical synapses between Off-bipolar cells and S3-Gbx2+ ACs, because AMPA/Kainate antagonists block cone input to Off bipolar cells. However, current-voltage relations of excitatory synaptic inputs during light-off responses, recorded with inhibition blocked, were linear and reversed near zero millivolts, which is inconsistent with a major input through gap junctions (data not shown).

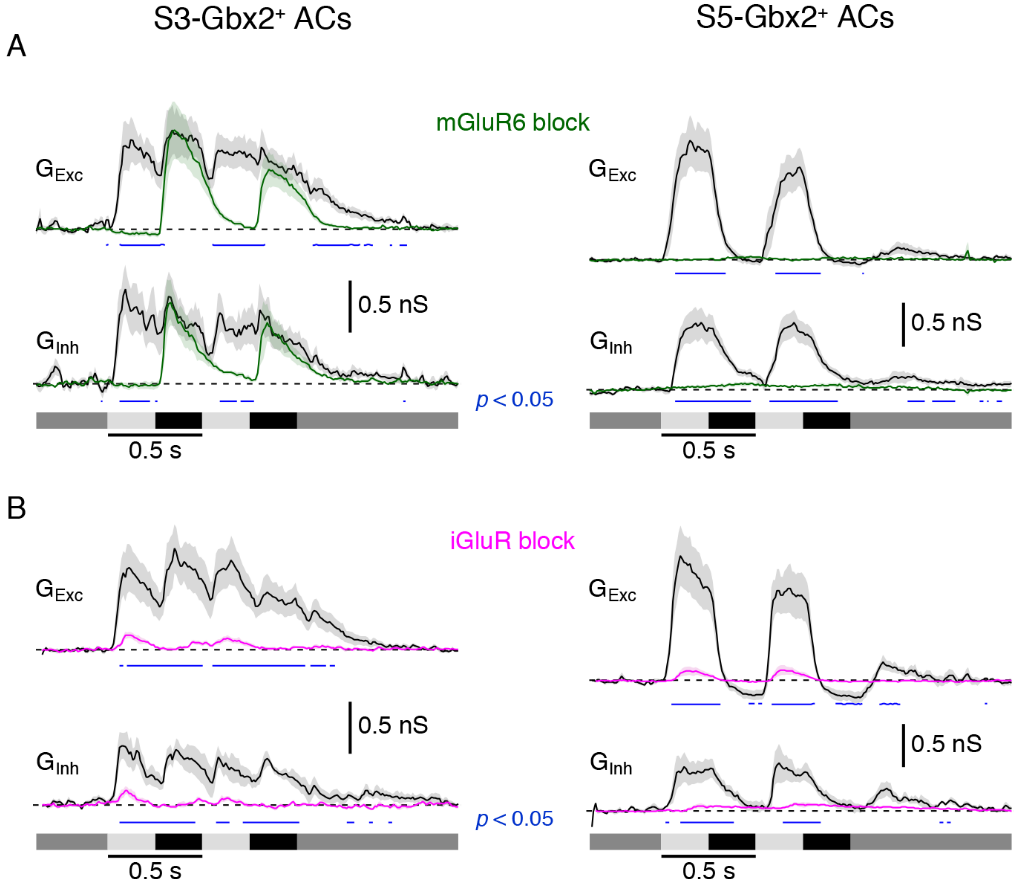

FIGURE 3.7 S3-and-S5Gbx2+ ACs have distinct excitatory and inhibitory inputs

(A) Conductance measurements from (n=7) S3 (left) and S5 (right) cells in response to a center spot stimulus in the presence (green) or absence (black) of mGluR6 receptor agonist 10 µM L-AP4 (On-pathway block). (B) Conductance measurements from (n=6) S3 and S5 cells in response to a center spot stimulus in the presence (magenta) or absence (black) of a cocktail of iGluR receptor agonists: 1 µM ACET, 20 µM GYKI, and 50 µM D-AP5. Traces represent average responses. Shading represents SEM. Blue traces indicate significant differences (paired t-test) between the drug and control conditions. p values indicated on graphs.

DISCUSSION

We have identified the *Gbx2*$^{CreERT2\text{-}IRES\text{-}EGFP}$ mouse line as a tool that can be used to genetically label two AC subtypes in the mouse retina that are morphologically, physiologically, and molecularly distinct from each other. S3-Gbx2+ ACs are On-Off type cells (Figure 3.5), have smaller, asymmetric dendrites that stratify in sublamina 3 of the IPL (Figure 3.4), and exhibit heterotypic gap junction coupling (Figure 3.6). S5-Gbx2+ ACs are On-type cells, have larger, more symmetric dendrites that stratify in sublamina 5 of the IPL, and lack consistent gap junction coupling. S3-Gbx2+ ACs lack expression of any of the standard inhibitory or excitatory neurotransmitters, identifying them as a subtype of nGnG ACs, whereas the S5-Gbx2+ ACs are GABAergic. RNAseq revealed the distinct molecular profiles of these two Gbx2+ AC subtypes, which confirms their identification as separate subtypes and informs future analyses of the cell-specific mechanisms that underlie their distinct morphology and physiological features.

Categorization of amacrine cell subtypes

Previous studies have used Golgi staining, cell fills, and sparse genetic labeling to categorize many amacrine cell subtypes based on their morphology (Badea and Nathans, 2004; Lin and Masland, 2006; MacNeil et al., 1999). Reconstruction of a 114μm x 80μm volume of mouse retina by serial-block face electron microscopy indicated the presence of >40 subtypes of amacrine cells (Helmstaedter et al., 2013). However, these approaches may undersample rare neurons, and do not provide a means to prospectively identify and manipulate individual subtypes. A recent single-cell transcriptomic study provides evidence for the existence of 63 molecularly distinct subtypes, indicating there is greater subtype diversity than previously predicted (Yan et al., 2020). One of the challenges going forward will be to match these molecularly-defined subtypes with their morphological counterparts and begin to tease out their connectivity patterns with visual circuits.

Single cell transcriptomic studies of AC subtypes initially identified two different nGnG AC subtypes, one that is molecularly similar to Glycinergic ACs and one that is similar to GABAergic ACs (Cherry et al., 2009; Macosko et al., 2015). The "Glycinergic-like" nGnG AC subtype is marked by specific expression of NeuroD6 (Kay et al., 2011). A recent study identified two additional nGnG subtypes closely related to NeuroD6+ nGnG ACs (Yan et al., 2020). In contrast, the S3-Gbx2+ AC subtype is the "GABAergic-like" nGnG subtype cluster #4 in the Macosko dataset (Macosko et al., 2015) and nGnG #4, cluster #36 in the Yan dataset (Yan et al., 2020). S3-Gbx2+ nGnG ACs appear to be conserved in primates based on cross-species analysis of single cell transcriptomics (Peng et al., 2019).

S5-Gbx2+ ACs closely resemble cluster #7 from the Macosko study based on the selective expression of *Maf*, *Cxcl14*, *Id4*, and *Lmo4* in both transcriptomic datasets (Figure 3.2A). S5-Gbx2+ ACs also share morphological, molecular, and physiological properties with the previously described CRH-1 AC (Jacoby et al., 2015; Park et al., 2018; Zhu et al., 2014). S5-Gbx2+ ACs and CRH-1 ACs have dendritic arbors of a similar size and shape that stratify in S5 of the IPL, they both express the neuropeptide *Crh* (*corticotrophin-releasing hormone*), and have similar physiological properties in response to ON light stimuli (Jacoby et al., 2015; Park et al., 2018). The CRH-IRES-Cre line used in these studies labels at least three different AC subtypes, which can be distinguished based on their morphological differences. An intersectional approach pairing the $Gbx2^{CreERT2\text{-}IRES\text{-}EGFP}$ with a recently developed *Crh-IRES-FlpO* line (Jackson Labs strain #031559) and a dual-recombinase reporter line should selectively label S5-Gbx2+ ACs and allow the direct testing of whether they are the same subtype as CRH-1 ACs.

Dendrite morphology and Gbx2+ AC function

The receptive field properties of ACs are dependent on the morphologies of their dendritic arbors. By using a combination of genetically labeling and electrophysiological recordings, we show that the morphologies and the spatial receptive field properties of the S3- and S5-Gbx2+ ACs are quite different from one another (Figure 3.6A-B). Although both cells display a center-surround organization, with fairly similar center diameters, the extent of the surround is much smaller for the S3 than the S5 cells. For S3-Gbx2+ ACs, responses during both the On and Off phase of the stimulus were strongly suppressed by the surround, with space constants around ~350 µm (Figure 3.6B). The S5-Gbx2+ ACs showed much weaker surround suppression, with a space constant exceeding 650µm. With stronger surround suppression, activated with a shorter space-constant, the S3 cells will be tuned to higher spatial frequencies than the S5 cells. It seems likely that the narrow surround inhibition of the S3 cells arises in the IPL, while the broader surround of the S5 ACs probably reflects, at least in part, the center-surround organization of the cone photoreceptor output, generated by horizontal cell feedback in the OPL. The lack of any surround suppression during the Off-phase of the response (Figure 3.6B) is expected if the response were produced by turning off presynaptic On bipolar cells that provide a tonic excitatory input to the S5 ACs. The disparity in the center size estimates for the On and Off phases of the stimulus might be explained by inputs from two populations of On-bipolar cells with different spatial distributions across the dendritic arbor. Further work will be required to test this hypothesis. Unlike S5 ACs, CRH-1 ACs have been shown to lack of any surround suppression during the On-phase of the response (compare fig. 3 of (Park et al., 2018), with Figure 3.6A). This discrepancy probably reflects differences in the physiological conditions of the preparations rather than evidence that S5 Gbx2+ ACs and CRH-1 ACs are different subtypes.

Unlike the S5-Gbx2+ ACs , the dendritic arbors of the S3-Gbx2+ ACs are asymmetric along the dorsal-temporal axis, with the soma offset relative to the dendritic arbor. Such asymmetries can influence the response properties of neurons. For example, J-RGCs display a similar asymmetry, which appears to enhance directional responses to ventral motion (Kim et al., 2008; Liu and Sanes, 2017). Examples of functional asymmetry are also found outside of the retina, such as in *Drosophila* proprioceptors, which are spatially tuned for the direction of muscle movement (He et al., 2019). It remains to be determined whether the asymmetric dendrites of S3-Gbx2+ ACs result in anisotropic physiological receptive field structure. The developmental mechanisms that instruct dendrite asymmetry and orientation are poorly understood, but likely involve a combination of selective directional growth and pruning of developing arbors (Liu and Sanes, 2017).

As a transcription factor, *Gbx2* is poised to regulate the cellular identity and development of Gbx2+ ACs. Subtype-specific transcription factors in retinal neurons have an important role establishing correct cell body location, dendrite morphology, and synaptic connectivity (Kay et al., 2011; Liu et al., 2018; Peng et al., 2020; Peng et al., 2017; Whitney et al., 2014). *Gbx2* regulates the specification, migration, and axon guidance of several neuronal populations in the brain and spinal cord (Chatterjee et al., 2012; Chen et al., 2010; Luu et al., 2011; Mallika et al., 2015). Therefore, *Gbx2* may potentially regulate development of Gbx2+ ACs through regulation of effector genes specific to this AC subtype, but its exact function in AC identity and development remains to be determined.

Modes of neurotransmission in S3-Gbx2+ ACs

Without GABA, glycine, and other chemical neurotransmitters, how do S3-Gbx2+ ACs communicate with other neurons? One possibility is that these neurons are in fact GABAergic, and the very low levels of *Gad1* and *Gad2* in these cells is sufficient for low levels of GABA synthesis. There are also non-canonical pathways for GABA synthesis, although S3-Gbx2+ ACs do not express appreciable levels of *Abat* (*GABA transaminase*) or *Aldh1a1* (*aldehyde dehydrogenase 1a1*), the enzymes required for these pathways (Kim et al., 2015; Tritsch et al., 2012; Tritsch et al., 2014). Alternatively, S3-Gbx2+ ACs could release GABA without *de novo* synthesis. Midbrain dopaminergic lack expression of *Gad1* and *Gad2* expression, yet release GABA that is taken up from the extracellular environment by plasma membrane GABA transporters (Tritsch et al., 2014). S3-Gbx2+ ACs express relatively high levels of *Slc6a1*, which encodes the plasma membrane GABA transporter Gat1 (Figure 3.2C).

In addition to chemical neurotransmitters, many retinal neurons also express neuromodulators and neuropeptides. Our RNA-seq results revealed that the S3-Gbx2+ ACs highly express the neuropeptide gene *Tachykinin 1 (Tac1)*, that encodes several neuropeptides, the most common one being Substance P (Figure 3.2C). Release of substance P from ACs can modulate the excitability of downstream retinal ganglion cells, however at a slower time scale than most neurotransmitters (Zalutsky and Miller, 1990). The genetic identity of Substance P releasing ACs in the mouse retina is unknown, and several other AC subtypes also express *Tac1* in addition to S3-Gbx2+ ACs (Yan et al., 2020). Ultimately, directly testing whether S3-Gbx2+ ACs use standard chemical neurotransmitters and/or neuromodulators will require identifying their downstream synaptic partners.

Many ACs exhibit homotypic coupling with neighboring ACs of the same subtype as seen with AII and NOS2 AC subtypes (Jacoby and Schwartz, 2018; Vaney, 1991). Coupling can spread signals laterally and may serve a "signal averaging" function in coupled cells. However, such signal averaging seems unlikely in S3-Gbx2+ ACs, because we never observed homotypic coupling despite significant overlap in their dendritic arbors (Figure 3.7C). Rather, S3-Gbx2+ ACs are heterotypically coupled with neighboring bipolar cells (BCs). Heterotypic coupling between ACs and bipolar cells has been previously observed in glycinergic AII and A8 ACs with cone BCs (Vaney, 1991; Yadav et al., 2019). The spatial pattern of the S3-Gbx2+ AC:BC tracer coupling is unusual, as it never extends beyond the central 80% of the dendritic arbor of the S3-Gbx2+ AC. Although the physiological recordings (Figure 3.7B), indicate that electrical synapses contribute minimal excitatory input to S3-Gbx2+ ACs at photopic light levels, it remains possible that signaling between S3-Gbx2+ ACs and cone BCs through electrical synapses could become prominent under specific conditions. Indeed, tracer coupling to BCs increased in a subset of S3-Gbx2+ ACs during application of a D1 receptor antagonist, which mimics low dopamine release that occurs under scotopic conditions (Figure 3.5D-F, I). These results demonstrate that tracer coupling can be modulated, and suggest that the physiological role of gap-junctions may depend on adaptation level. It is also possible that gap junction connections may mediate S3-Gbx2+ AC to excite ganglion cells indirectly by depolarizing BCs. In this situation, electrical synapses could amplify local signaling between S3-Gbx2+ ACs and BCs. While the BC subtype coupled to S3-Gbx2+ ACs is unknown, based on the stratification of coupled-BC axon terminals in the IPL it is likely to include Type 5 and possibly Types 6 and 7a BCs (Ghosh et al. 2004). Futures studies should be able to determine this connectivity with a combination of immunohistochemistry or genetic markers for BC subtypes. In addition, the identity of the connexins that mediate coupling between S3-Gbx2+ ACs and BC remains unknown. Our RNAseq data, *Gjd2* (Cx36), *Gjc1* (Cx45), and *Gje1* (Cx23) are all expressed in S3-Gbx2+ ACs, implicate a number of potential targets.

Potential visual modalities requiring Gbx2+ ACs

What are the functions of Gbx2+ ACs in the retina? While this remains an open question, the stratification pattern of Gbx2+ AC dendrites to specific lamina in the IPL restricts their potential synaptic partners and allows for some speculation. Each sublamina in the IPL contains the dendrites of a specific subset of RGC subtypes and responds to a specific set of visual modalities (Roska and Werblin, 2001). If S5-Gbx2 ACs are the CRH-1 subtype as hypothesized above, we would expect that they provide inhibition onto "sustained" Suppressed-by-Contrast (SbC) RGCs and ON αRGCs (also known as the M4 subtype of intrinsically-photosensitive RGCs (ipRGCs)) (Estevez et al., 2012; Jacoby and Schwartz, 2018; Jacoby et al., 2015; Park et al., 2018). Sublamina 5 also contains the dendrites of M2, M3, and M5 subtypes of ipRGCs, which are involved in visual modalities involved in light avoidance, pupillary reflex, and circadian rhythm behaviors (Schmidt et al., 2011; Sonoda et al., 2020).

In contrast to the S5-Gbx2+ ACs, the S3-Gbx2+ ACs do not resemble any previously described AC subtype. With dendrites that ramify in sublamina 3 of the IPL (Figure 3.1), the S3-Gbx2+ ACs could be connected to W3B RGCs that are involved in object motion detection (Krishnaswamy et al., 2015; Zhang et al., 2012), or other small-field RGCs involved in spatial vision (Jacoby and Schwartz, 2018). However, it is important to note that not all ACs and RGCs that co-stratify in an IPL sublamina are synaptically connected (Krishnaswamy et al., 2015). Furthermore, we currently lack a complete accounting of the dendritic stratification of the 40+ RGC subtypes that have been defined molecularly, suggesting there are other potential synaptic partners (Rheaume et al., 2018; Tran et al., 2019). Ultimately, the presence of functional connections between S3- and S5-Gbx2+ ACs and their potential postsynaptic targets will require paired recordings, which should be feasible now that we have genetic tools to prospectively identify Gbx2+ ACs.

Over the past few years, single-cell transcriptomics has greatly increased the cellular inventory of molecularly distinct neuronal subtypes. Going forward we will need genetic tools to interrogate specific neuronal subtypes within a given neural circuit, as we have done in this study. The $Gbx2^{CreERT2\text{-}IRES\text{-}EGFP}$ line has allowed us to define the molecular, morphological, and physiological properties of two AC subtypes. In particular, the unusual properties of the S3-Gbx2+ AC subtype raise a number of intriguing questions about their form and function within the retina for future studies.

SUPPLEMENTAL FIGURES

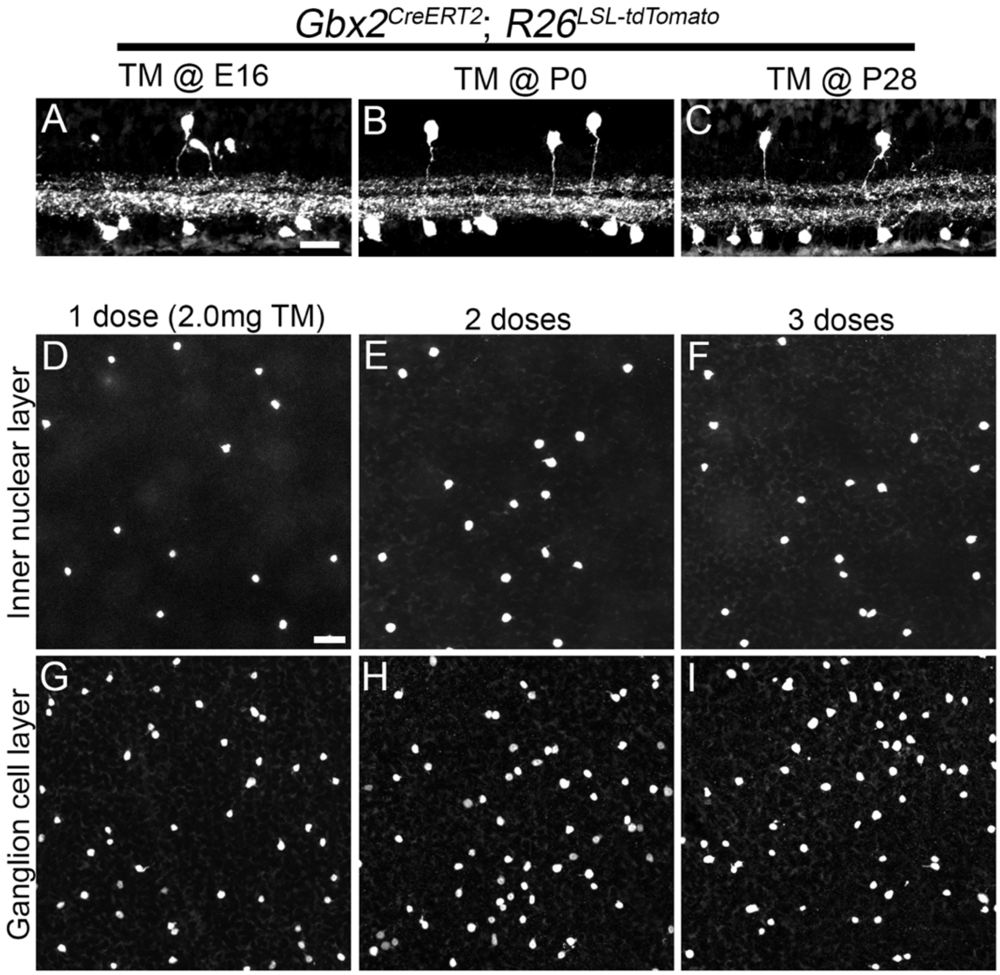

FIGURE 3.S1 Gbx2$^{CreERT2\text{-}IRES\text{-}EGFP}$ expression is consistent throughout the mouse development and adulthood. Related to Figure 3.1

(A-C) Adult (P35) Retinal cross-sections from *Gbx2*$^{CreERT2\text{-}IRES\text{-}EGFP}$*; R26*$^{LSL\text{-}tdTom}$ mice dosed with of Tamoxifen (60mg/kg) at (A) E16, (B) P0, (C) P28. (D-I) Z-projections through the cell bodies of the inner nuclear layer (D-F) and ganglion cell layer (G-I) from retinal flat mounts of *Gbx2*$^{CreERT2\text{-}IRES\text{-}EGFP}$*; R26*$^{LSL\text{-}tdTom}$ mice administered 2.0mg/day tamoxifen for (D, G) 1 day (dose), (E, H) 2 days, (F-I) 3 days. Scale bar, 25µm in (A) and (D).

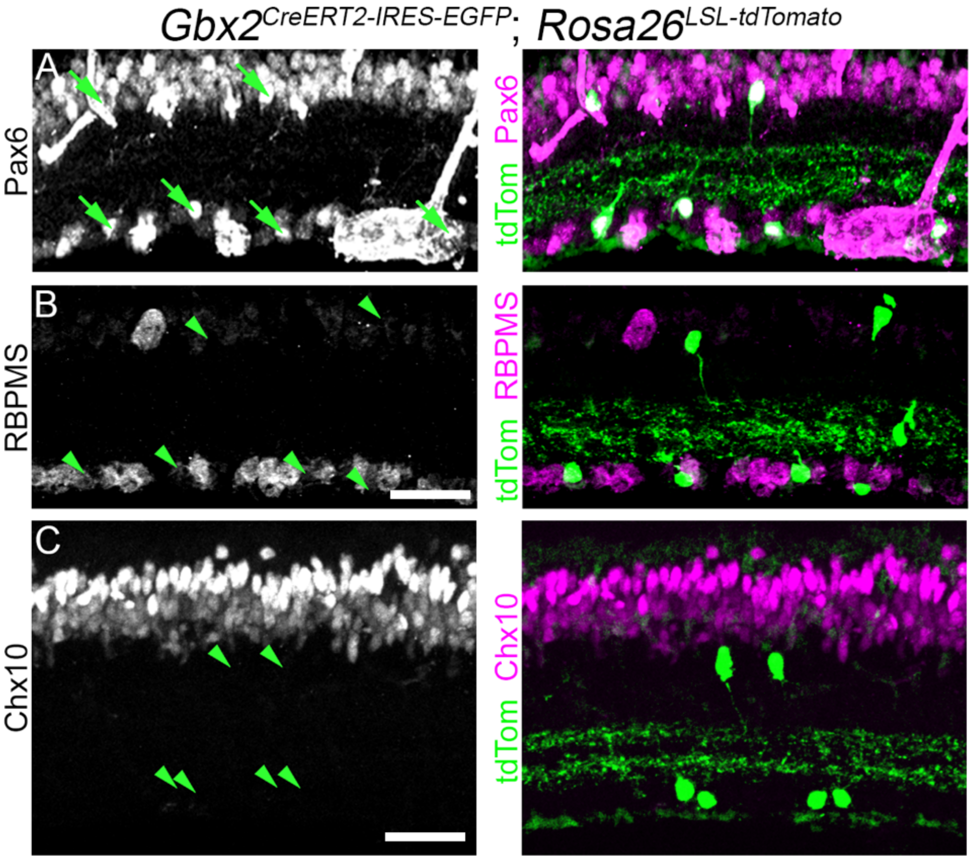

FIGURE 3.S2 Gbx2+ retinal neurons are amacrine cells. Related to Fig. 3.1.

Cross-sections of an adult retina from a *Gbx2*$^{CreERT2\text{-}IRES\text{-}EGFP}$; *Rosa26*$^{LSL\text{-}tdTom}$ mouse labeling the total Gbx2+ AC population. Left: Neurotransmitter markers, (A) Pax6, (B) RBPMS, and (C) Chx10, label amacrine cells, retinal ganglion cells, and bipolar cells in the inner nuclear layer and ganglion cell layer, respectively. Right: Merged images showing both the select neurotransmitter marker (magenta) and Gbx2+ ACs (green). Arrows denote colocalization between the cell marker and Gbx2+ ACs, and arrowheads denote Gbx2+ ACs that do not colocalize with the specific cell marker. Scale bar, 25 µm.

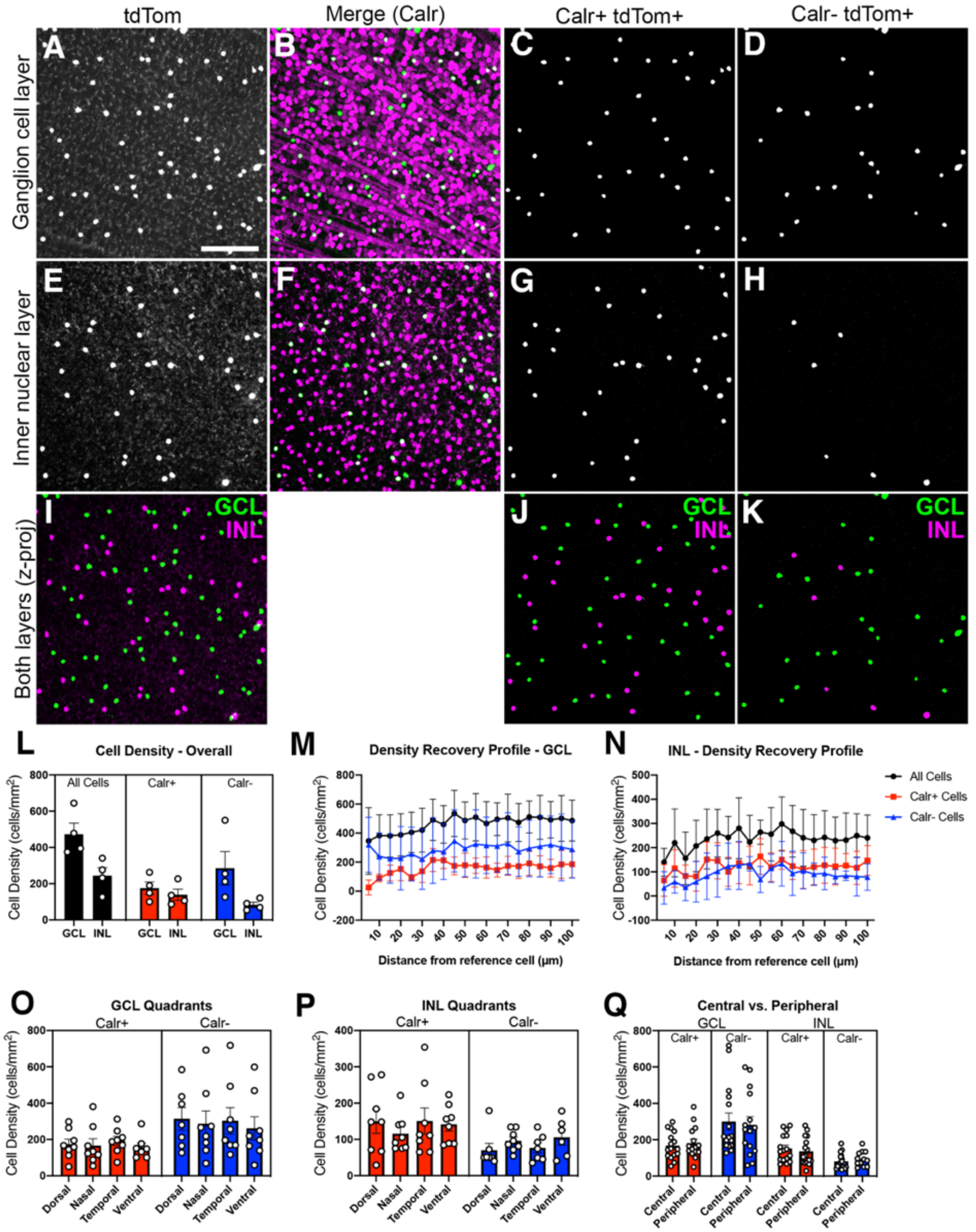

Figure Legend on next page

FIGURE 3.S3 Gbx2+ AC subpopulations have consistent density and spacing across the retina. Related to Fig. 3.1.

(A) Tdtomato expressing Gbx2+ ACs in the ganglion cell layer (GCL) in a retina flatmount from a *Gbx2*^{CreER}; *R26*$^{LSL\text{-}tdTomato}$ mouse. (B) Gbx2+ ACs (green) immunolabeled for calretinin (Calr, magenta) in the GCL. (C-D) Masked image of cell bodies of Gbx2+ neurons (C) Calretinin+ and (D) Calretinin- from the image in (B). (E) TdTomato expressing Gbx2+ ACs in the inner nuclear layer (INL). (F) Gbx2+ ACs (green) immunolabeled for calretinin (magenta) in the INL. (G-H) Masked image of cell bodies of Gbx2+ neurons (C) Calr+ and (D) Calr- from the image in (F). (I-K) Z-projection through the GCL and INL (pseudocolored green and magenta, respectively) for (I) all Gbx2+ ACs, (J) Calr+ Gbx2+ ACs, and (K) Calr- Gbx2+ ACs. (l) Quantification of the cell density of Calr+ and Calr- Gbx2+ ACs in the GCL and INL (n= 24 measurements from 4 mice). (M-N) The density recovery profile (DRP) of Calr+ and Calr- Gbx2 ACs in the (M) GCL and (N) INL (n= 32 measurements from 4 mice, respectively). (O-Q) The cell densities in the four quadrants of the retina of Gbx2+ AC in the (O) GCL and (P) INL (n= 32 measurements from 4 mice, respectively). (Q The cell density of Gbx2+ AC populations in the central and peripheral retina (n= 32 measurements from 4 mice, respectively). Data represented as mean ± SEM. Scale bar, 50 μm in (A).

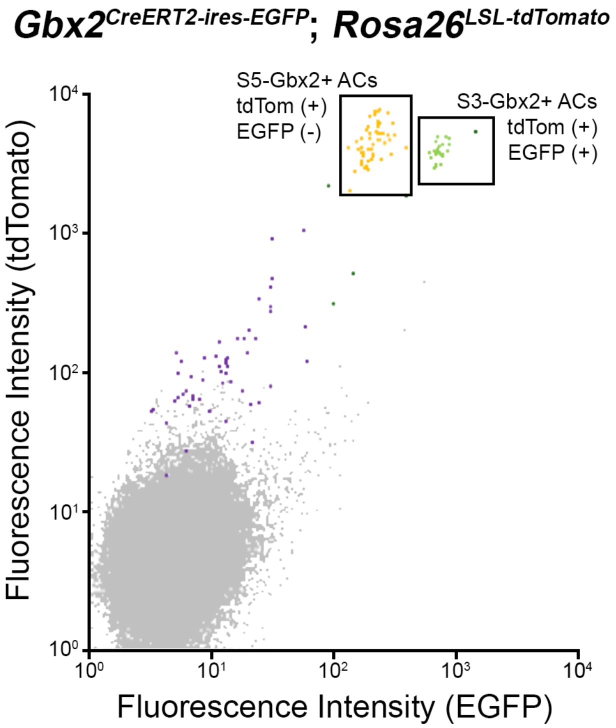

FIGURE 3.S4 Flow cytometry plot of dissociated retinal neurons isolated from a Gbx2$^{CreERT2\text{-}IRES\text{-}EGFP}$; Rosa26$^{LSL\text{-}tdTomato}$ mouse. Related to Figure 3.2

Using fluorescence-activated cell sorting, Gbx2+ ACs (tdTomato+) from P8 retina were isolated and separated into the S5-Gbx2+ ACs (tdTomato+, EGFP^{low}) and the S3- Gbx2+ ACs (tdTomato+, EGFP^{high}) groups for bulk RNA sequencing.

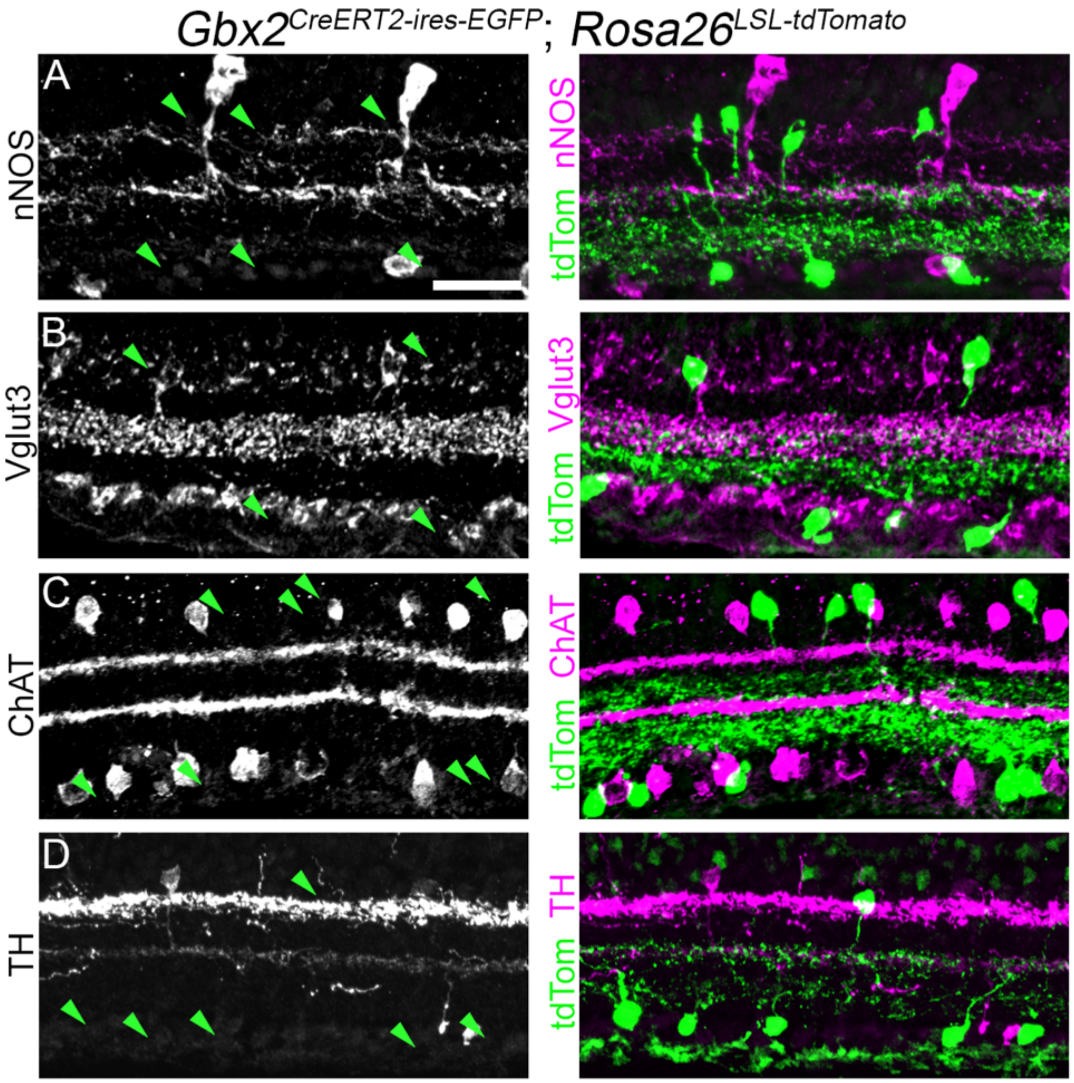

FIGURE 3.S5 Gbx2+ ACs do not colocalize with many canonical neurotransmitter cell markers. Related to Figures 3.2 and 3.3

Cross-sections of an adult retina from a *Gbx2*$^{CreERT2\text{-}IRES\text{-}EGFP}$; *Rosa26*$^{LSL\text{-}tdTom}$ mouse labeling the total Gbx2+ AC population (high-TM, 2.0mg tamoxifen). Left: Left, retinal sections from a *Gbx2*$^{CreERT2\text{-}IRES\text{-}EGFP}$; *Rosa26*$^{LSL\text{-}tdTom}$ mouse immunolabeled with (A) neuronal nitric oxide synthase (nNOS), (B) vesicular glutamate transporter 3 (Vglut3), (C) choline acetyl transferase transporter (ChAT), and (D) tyrosine hydroxylase (TH). Right: Merged images of Gbx2+ ACs (green) and the neurotransmitter marker (magenta). Arrows denote colocalization between the cell marker and Gbx2+ ACs, and arrowheads denote Gbx2+ ACs that do not colocalize with the specific cell marker. Scale bar, 25 µm.

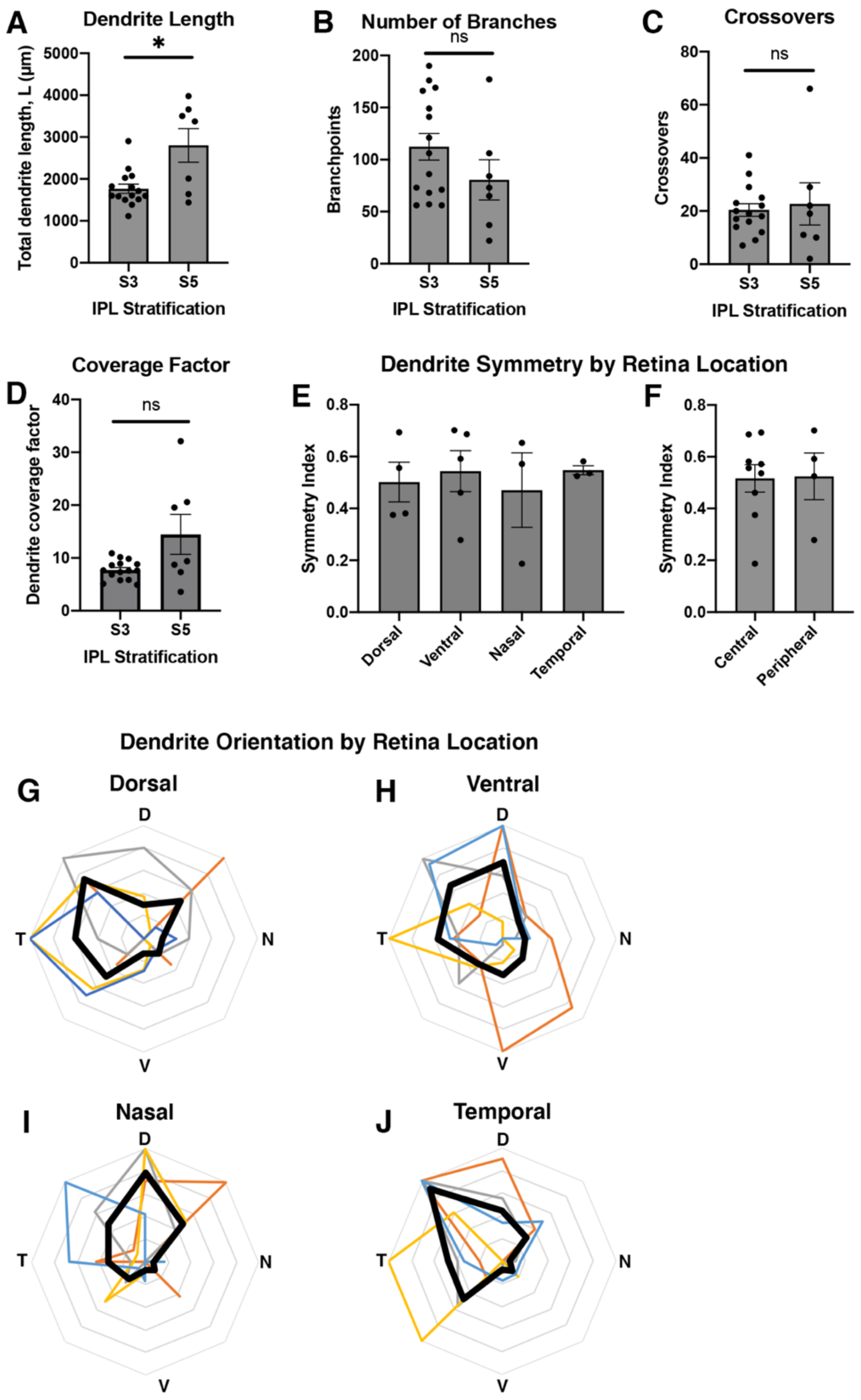

Figure Legend on next page

FIGURE 3.S6 Dendritic morphology and orientation of Gbx2+ ACs by retina location. Related to Figure 3.4

(A-C) S3- and S5-Gbx2+ AC morphology in (A) total dendrite length, (B) number of branches, (C) dendrite branch self-crossover. n=15, 7 cells for S3 and S5 respectively. (D, E) S3-stratifying Gbx2+ ACs show a similar dendrite asymmetry in (D) each retinal quadrant (n=3-5 retinas per quadrant) and (E) between central and peripheral retina (n=4, 9 retinas respectively). (F-I) A polar plot of dendrite orientation of S3-targeting Gbx2+ ACs in each retinal quadrant; black trace represents the mean and colored traces represent neurons quantified from a single retina (n >20 neurons per retina, n= 4 retinas). D, dorsal; V, ventral; N, nasal; T, temporal. Data represented as mean ± SEM. *p<0.05 by an unpaired t-test with a Welch's correction.

Methods

Animals and Animal Procedures

Gbx2$^{CreERT2\text{-}IRES\text{-}EGFP}$ (Chen et al., 2009), *NeuroD6*^{Cre} (NEX^{Cre}) (Schwab et al., 2000), *Ai9/Rosa26*$^{LSL\text{-}tdTomato}$ (Madisen et al., 2010), and *Ai140D/TIGRE*$^{TRE2\text{-}LSL\text{-}GFP,\ CAG\text{-}LSL\text{-}tTA2}$ (Daigle et al., 2018) mice were maintained on a C57BL/6J background. Mice of both sexes were used for all experiments. Tamoxifen was administered at E16, P0, and adults (>P28) ages. For E16 timepoints, 200µL of 5mg/mL tamoxifen and 2.5mg/mL progesterone dissolved in sunflower seed oil was administered to pregnant dam by oral gavage. Pregnancies were timed by the presence of a vaginal plug marked as E0.5. At P0 timepoints, 50 µL of 0.5mg/mL tamoxifen was injected with into the milk pouch of the mouse pups, as previously described (Pitulescu et al., 2010). At adult ages, 200µL of 5mg/mL tamoxifen was administered by oral gavage for at least two consecutive days to ensure complete recombination of the *Cre*-dependent reporter (Figure S1). All animal procedures were approved by Oregon Health & Science University Institutional Animal Care and Use Committee, the Institutional Animal Care and Use Committee of University of California (Berkeley, CA)**,** and conformed to the National Institutes of Health's *Guide for the Care and Use of Laboratory Animals*.

Immunohistochemistry

Adult retinas were prepared for immunolabeling by removing the eyes from the head of a recently euthanized mouse. The cornea was removed and the eyes were fixed in 4% EM-grade paraformaldehyde (PFA) for 30 minutes at room temperature. Eyes were washed in PBS for 30 minutes post-fixation. Tissue for cryosections was cryo-protected in 10% and then 20% sucrose in PBS for 1 hour each at 4 ºC. The lenses were removed and the eye cups were placed in cryomold with Optimal Cutting Temperature media and frozen. Retinas were sectioned at 20µm using a cryostat. Slide mounted retinal sections were washed for 10 mins in PBS and blocked with 2% normal donkey serum, 0.2% TritonX-100 in PBS for 30 mins. Sections were incubated in primary antibody in blocking buffer overnight at 4 °C. Primary antibodies were used at the dilutions listed in the Key Resources Table. Sections were washed 3 times for 10 mins in PBS and incubated in secondary antibodies in blocking buffer for 2 hrs at room temperature. All secondary antibodies were used at a 1:500 dilution. Retinal sections were washed three times in PBS for 10 mins with DAPI (1:5000) included in the first wash step. Tissue was mounted in Fluoromount-G (Southern Biotech) and cover slipped for imaging.

Retina flat-mounts were fixed and washed as described above. The retinas were isolated from the eye cup and flattened by making 3-4 equally spaced incisions from the edge of the retina. Retina flat-mounts were post-fixed in 4% PFA in PBS for 10 minutes to help maintain their shape. Retinas were washed in blocking buffer (4% normal donkey serum, 0.2% TritonX-100) 3 times for 30 minutes. Retinas were incubated in primary antibody in blocking buffer for 3 days at room temperature. Following incubation of primary antibody, retinas were washed 3 times for 30 minutes in blocking buffer. Retinas were then incubated in secondary antibody overnight at room temperature. Next, retinas were washed in PBS three times for 30 minutes, flattened on slides, and cover slipped in Fluoromount-G for imaging.

Fluorescence Image Acquisition

All retinal sections were imaged on a Zeiss Axio Imager M2 upright microscope equipped with an ApoTome2 using a 20X objective. Retinal flatmounts for mosaic analysis, single-cell morphology, and tracer coupling experiments were imaged on a Zeiss LSM 880 confocal microscope using a 40X objective. Images were acquired using the Zeiss Zen Imaging software for both microscopes.

Electrophysiology

Adult mice of either sex were dark adapted for 1-2 hours. Animals were anesthetized with isoflurane before being euthanized via cervical dislocation. Subsequent to enucleation, all procedures were performed under infrared illumination. The retina and attached pigment epithelium were dissected free from the sclera and placed in a recording chamber under a microscope and continuously perfused (5ml/min) with Ames medium maintained at 34°C. Cells were visualized though a 40x water-immersion objective and Dodt contrast illumination. Fluorescent Gbx2+ ACs were targeted under 2-photon guidance (excitation wavelength: 920 nm) with a Ti:sapphire laser (Chameleon ultra II; Coherent). Correct targeting was confirmed by visualizing the Alexa dye in intracellular solution fill the soma and processes of the target cell. Patch electrodes were pulled from borosilicate glass to a final resistance of 8-12 MΩ. For voltage-clamp recordings, pipettes were filled with an intracellular solution containing the following (in mM): 125 Cs-methanesulphonate, 7 CsCl, 10 Na-HEPES, 3 phosphocreatine-Na_2, 1 EGTA, 2 Mg-ATP, 1 Na-GTP, 0.1 Alexa Fluor 488 hydrazide, and 3 QX-314 chloride. The solution was adjusted to pH 7.35 using CsOH. Cesium was included in place of potassium to block voltage-gated potassium currents, thereby improving the voltage clamp at positive potentials. QX-314 was included to block voltage-gated sodium channels. For current-clamp recordings, all solution components were the same except potassium was used in place of cesium, and QX-314 was not included. Currents were sampled at 10 kHz and filtered at 2 kHz through the four-pole Bessel filter in an EPC-10 patch clamp amplifier (HEKA). Voltages were corrected for a liquid junction potential of -10mV.

Visual stimuli were produced using custom software based on PsychoPy routines (Peirce, 2007). The stimuli, generated on a Texas Instruments digital light projector (DLP; Lightcrafter 4500), were projected onto the photoreceptor layer through a 10x water immersion objective (0.3 NA, Olympus). The DLP intensity was linearized using a calibrated lookup table. DLP intensity was attenuated using neutral density filters to produce a grey adapting background flux of ~3.4x10^{5} photons/µm^{2}/s. Stimuli were first aligned to the receptive field center of each cell using a series of 100 x 1000 µm vertical and horizontal bars to locate the cell's maximal response. All subsequent stimuli were centered on the coordinate of maximum response. Receptive field sizes were estimated from area-response data and fit to a difference of Gaussians function:

$$\boxed{R = K_c e^{-(d/\sigma_c)^2} - K_s e^{-(d/\sigma_s)^2}}$$

where R is the peak response evoked by a stimulus of diameter d, K_c and K_s are the amplitudes of the excitatory and inhibitory components, respectively, and σ_c and σ_s are their space constants.

Pharmacological agents

Drugs were added to the perfusion solution. The following agents were used: L-(+)-2-amino-4-phophonobutyric acid (L-AP4; 20µM; Tocris Bioscience, catalog #0103), D-(-)-2-amino-5-phophonopentanoic acid (D-AP5; 50µM; Abcam Biochemicals, catalog #120003), 1-(4-aminophenyl)-3-methylcarbamyl-4-methyl-3,4-dihydro-7,8-meth- ylenedioxy-5H-2,3-benzodiazepine hydrochloride [GYKI-53655 (GYKI); 50µM;Tocris Bioscience catalog #2555), (*S*)-1-(2-Amino-2-carboxyethyl)-3-(2-carboxy-5-phenylthiophene-3-yl-methyl)-5-methylpyrimidine-2,4-dione (ACET; 1µM; Tocris Bioscience, catalog #2728).

Data analysis

Light-evoked synaptic conductance was calculated as described previously (Taylor and Vaney, 2002). Briefly, current–voltage (I–V) relations were measured at 10 ms intervals over a range of voltage steps from -90 +50 mV in 20mV increments. The total light-evoked conductance was calculated as the difference between the I–V relation at each time point and the "leak" I–V relation measured just before the onset of the light stimulus. To avoid errors in calculating the net light-evoked currents due to a sloping baseline during positive voltage steps, a single exponential trend was subtracted from the current traces for each voltage step before t. he leak subtraction. The excitatory and inhibitory conductance could then be calculated at each time point using the observed I–V reversal potential along with the cation and chloride reversal potentials.

Tracer coupling

Gbx2$^{CreERT2\text{-}IRES\text{-}EGFP}$; *Rosa26*$^{LSL\text{-}tdTomato}$ mice were used to target tdTomato positive neurons in the GCL for electroporation of Neurobiotin, as previously described (Kanjhan and Vaney, 2008; Sivyer and Vaney, 2010) . In isolated preparations of retina bathed in Ames medium at room temperature, tdTomato positive neurons were lose seal patched with an intracellular solution containing (in mM): 120 K-gluconoate; 6 KCl;10 HEPES Na;10 Phosphocreatine-Na_2; 60 Neurobiotin-Cl; 2 ATP; 0.5 GTP pH balanced to 7.2 with KOH. Once a seal was established the HEKA EPC-800 amplifier was switched to current clamp mode and ACs were electroporated by applying 0.5-1nA pulses for 0.5 s at 1 Hz. Following electroporation, retinae were incubated in Ames medium for 45 mins at 35 C before being transferred to room temperature Ames, mounted on nitrocellulose filter paper and fixed in cold paraformaldehyde in PBS for 30 mins. Retinas were then wash twice with 0.2% Triton in 1X PBS and incubated with

10 μg/mL Streptavidin Alexa Fluor 488 (Thermo Fisher) at room temperature overnight. Before imaging, stained retinas were washed three times in 1X PBS before being mounted on a glass coverslip.

Retina Dissociation and FACS

Retinas from P6 or P7 mouse pups were dissected and isolated in 1X Hank's Balanced Salt Solution (HBSS). Cells were dissociated into a single-cell suspension by incubating the retinas in 1mL of HBSS containing 10U of papain (Roche) and 200μM cysteine. Retinal tissue was incubated at 37 °C for 30 mins. After papain incubation, the tissue was pelleted using a bench top microfuge and washed twice with 1mL of HBSS. Cells were gently dissociated in 500μL of HBSS by flicking the tube. Dissociated cells were passed through a cell strainer (35μm nylon mesh) to remove any cell aggregates. DNase was added to the solution and the samples were placed on ice until sorted. Gbx2+ amacrine cells were sorted into two groups S3-cells that were both GFP+ and tdTomato+ and S5-cells that were only tdTomato+. All fluorescence activated cell sorting (FACS) was completed in the OHSU Flow Cytometry Core using a BD InFlux equipped with 488nm and 561nm laser lines. All cells were sorted directly into cell lysis buffer and RNA was isolated with Agilent Absolutely RNA Nanoprep Kit.

RNAseq library preparation and sequencing

The cDNA libraries for used for sequencing of 4 total RNA samples were synthesized using a SMART-Seq Ultra Low Input RNA kit (Takara) in the OHSU Massively Parallel Sequencing Shared Resource Core Facility. Two of the cDNA libraries contained tdTomato+/GFP+ cells (S3-Gbx2+ ACs) and two samples contained the cDNA libraries for tdTomato+ only cells (S5-Gbx2+ ACs). Quality and quantity of the cDNA libraries was determined on a Bioanalyzer. For multiplex sequencing, all four cDNA sample libraries were loaded on a single lane on a HiSeq 2500 sequencer (Illumina). Libraries were sequenced to a depth of 45-55 million reads per sample. Alignment rate of total reads was >97% across all samples.

Co-localization analysis

All co-localization experiments used retinal sections from the *Gbx2*$^{CreERT2\text{-}IRES\text{-}EGFP}$; *Rosa26*$^{LSL\text{-}tdTomato}$ mouse line. Co-localization was determined by antibody labeling within the soma of the Gbx2+ amacrine cell bodies. Images were collected and analyzed as z-stacks to confirm the antibody labeling was within the soma of the correct z-depth. Offline analysis was completed using FIJI (Schindelin et al., 2012).

Mosaic cell spacing analysis

To analyze cell density and mosaic cell spacing, we used a 500µm x 500µm area of tissue from 4-8 locations within a single retina. Retina orientation was maintained to make spatial measurements in dorsal, ventral, temporal, and nasal areas of the retina. In addition, measurements in the peripheral and central regions of the retina made in ROIs ~200µm from the peripheral edge or optic nerve head respectively. Cell counts and X-Y coordinates were measured offline in FIJI (Schindelin et al., 2012) and density recovery profiles were obtained by analysis completed in WinDRP (Rodieck, 1991).

Neuron morphology analysis

For analysis of dendrite stratification in cross-section, we made measurements of fluorescent intensity along IPL depth using FIJI. These values were binned into 5% increments along the IPL depth using the FIJI plugin, IPLaminator (Li et al., 2016). For analysis of dendritic arbor morphology in retinal flatmounts we analyzed isolated single cells labeled using either sparse expression in *Gbx2*$^{CreERT2\text{-}IRES\text{-}EGFP}$; *Tigre*$^{LSL\text{-}GFP}$ mice or by targeted cell fills using Alexa

Fluor 488 hydrazide (Fisher Scientific). Offline tracing and analysis of dendritic arbors were made using the Filaments plugin in Imaris (Bitplane). Dendrite density (L/A) was calculated by dividing dendrite length (L) over dendrite area (A). Coverage factor was calculated by dividing the dendrite area over the cell density of Gbx2+ ACs in the INL and GCL for each subtype. Symmetry Index was calculated by subtracting the sums of missing dendrite coverage from 360 and then divided by 360, as previously described (Sun et al. 2013). Dendrite orientation was determined by the direction of the longest dendritic branch of a single cell and values were binned into 8 different groups based on the cardinal directions.

RNAseq analysis

Differential expression analysis was performed by the ONPRC Bioinformatics & Biostatistics Core. The quality of the raw sequencing files was evaluated using FastQC combined with MultiQC (http://multiqc.info/) (Ewels et al., 2016). Trimmomatic was used to remove any remaining Illumina adapters (Bolger et al., 2014). Reads were aligned to Ensembl's GRCm38 along with its corresponding annotation, release 99. The program STAR (v2.7.3a) was used to align the reads to the genome (Dobin et al., 2013). STAR has been shown to perform well compared to other RNA-seq aligners (Engstrom et al., 2013). Since STAR utilizes the gene annotation file, it also calculated the number of reads aligned to each gene. RNA-SeQC (DeLuca et al., 2012) and another round of MultiQC were utilized to ensure alignments were of sufficient quality.

Gene-level differential expression analysis was performed in open source software R (R Core Team, 2017). Gene-level raw counts were filtered to remove genes with extremely low counts in many samples following the published guidelines (Chen et al., 2016), normalized using the trimmed mean of M-values method (TMM) (Robinson and Oshlack 2010), and transformed to log-counts per million with associated sample wise quality weight and observational precision weights using voom method (Law et al., 2014). Gene-wise linear models comparing the cell types (tdTom+ vs. GFP+/tdTom+) were employed for differential expression analyses using limma with empirical Bayes moderation (Ritchie et al., 2015) and false discovery rate (FDR) adjustment (Benjamini and Hochberg, 1995).

RNAseq datasets were organized and displayed into gene families with R Studio and the START app (Nelson et al., 2017); and using the reference gene groups determined by the *HUGO Gene Nomenclature Committee at the European Bioinformatics Institute* (www.genenames.org). All graphs displaying RNAseq data were made using the Prism 8 Software (Graphpad Software, Inc.). RNA-sequencing data generated in this manuscript are available at Gene Expression Omnibus (https://www.ncbi.nlm.nih.gov/geo/), GEO accession number: GSE157271.

Statistics

For each experiment and time point a minimum of 3 retinas from three different mice were analyzed. For analysis of neuron morphology and tracer coupling, at least 5 neurons were analyzed from at least 3 animals. For all data sets, the variance was reported as mean ± SEM. Each data set was first tested for normality. Analysis between two groups was completed by using unpaired Student's t-test (parametric) or Mann-Whitney U test (nonparametric). For analysis between more than two groups, we used either a one-way analysis of variance (ANOVA) with Tukey's multiple comparison test (parametric) or Kruskal-Wallis with Dunn's multiple comparison test (nonparametric). All statistical significance tests were completed using Prism 8 Software (Graphpad Software, Inc.) and Igor Pro 8.02 (WaveMetrics, Inc.) for electrophysiological analyses.

ADDENDUM

The study presented thus far in Chapter 3 was a collaborative project among the Wright, Sivyer, and Taylor labs. My contribution was mainly to the electrophysiology components (Figures 3.6 and 3.7). However, since publication of this project in Cell reports in 2020, as well as previous work that did not comprise initial descriptive functional data that fit with the goals of this publication, we have made considerable progress in describing and analyzing S3 and S5 stratifying Gbx2+ ACs, particularly regarding the pharmacological makeup of the inhibitory mechanisms comprising both cell types' surround receptive fields. I hope that by expanding on this data here, a future researcher can continue work on these cell types that have a considerable dearth of understanding, particularly regarding what role they play in shaping retinal output.

Spatial mapping of excitatory and inhibitory inputs to S3 and S5-Gbx2+ ACs

To more precisely address spatial extent of pre and postsynaptic excitatory and inhibitory inputs to either Gbx2+ AC-type we first measured their excitatory and inhibitory postsynaptic currents (E/IPSCs) by holding Gbx2+ ACs at either -70 mV to isolate excitatory inputs, or 0 mV to isolate inhibitory inputs. At those holding potentials we presented a of 2 Hz flickering spot stimuli from 25 to 1200 μm in diameter. This allowed us to precisely measure the spatial extent of each pre and postsynaptic inhibitory input that shapes the surround suppression we observed in both cell types' voltage responses in figure 3.6 A-B. (86 and 53% suppression respectively for S3 and S5 cells.)

S3-Gbx2+ ACs display ON and OFF pathway PSCs shown in Figure 3.8 A, lower traces and negative polarity markers in B, with a maximum EPSC amplitude of -37 ± 3 (ON) and IPSC amplitude of 33 ± 3 pA (ON) at 250 μm, and modest reduction of 30 (ON) and 33% (OFF) to -26 ± 2 (ON) and 22 ± 2 pA (OFF) at 1200 μm diameter spot sizes. The fact that the reduction in absolute EPSC amplitude does not generate the entirety of the 86% membrane suppression we observed in S3-Gbx2+ AC voltage responses in Figure 3.6 A-B suggests postsynaptic inhibition is adding considerably to their inhibitory surrounds. This is in line with the inhibitory conductance we measured in figure 3.6 E in which we observed both a decrease in G_{EXC} and an increase in G_{INH}. This however, was only measured at two stimulus diameters (250 and 1200 μm).

When we measured IPSCs in the same S3-Gbx2+ ACs across a wider range of diameters, we found ON and OFF pathway IPSCs shown in Figure 3.8 A, left, upper traces and positive polarity markers in B, left, with a maximum of 86 ± 7.5 (OFF) and 90 ± 7.6 pA (ON) at 1200 μm. The amplitudes as a function of spot diameter are described by a single Gaussian function with a center width of 459 ± 12 μm (ON) and 422 ± 21 μm (OFF). This reflects a wide-field inhibitory input with a roughly 900 μm diameter (suggested by 2x the center Gaussian width). This input could be an individual ON-OFF wide-field AC or two separate populations, one ON, one OFF. There was a 76% (ON) and 82% (OFF) increase in IPSCs from the measured EPSC peak size (250 μm) to the IPSC peak at 1200 μm, suggesting the total voltage suppression of S3-Gbx2+ ACs is a combination of their pre and postsynaptic inhibitory surrounds. Narrow-field excitatory input that is suppressed at larger spot diameters combined with wide-field postsynaptic inhibition is a common arrangement among ganglion cell types that signal about small diameter stimuli. It bears a resemblance to the LMD GC inhibitory and excitatory inputs in Figures 2.4D-F and 2.5C-D. The similarities in PSC arrangement between S3-Gbx2+ ACs and LMD GCs suggest the S3-Gbx2+ ACs are signaling potentially to their gap junction coupled bipolar cells in response to some particular small feature in the visual scene. S-Gbx2+ACs on the other hand showed less surround suppression (53%) and only showed evidence of a strong pre-synaptic inhibitory mechanism via the suppression of G_{EXC} but no added G_{INH} at 1200 µm compared to 250 µm stimulus diameters (Figure 3.6 E, right panel). Notably, there is clear postsynaptic inhibition present, though it is not significantly different between center and full-

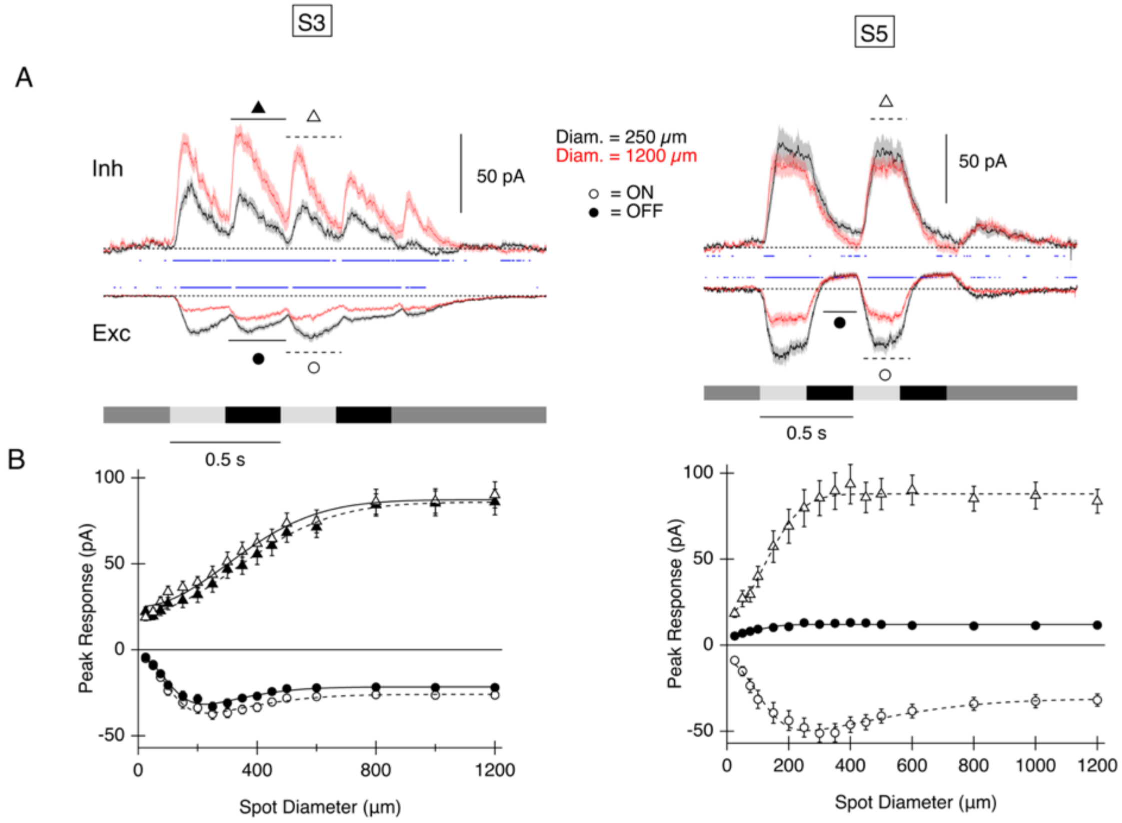

C

Response		Center (σ_1 in µm)	Surround (σ_2 in µm)	Center	Surround
△	ON	459 ± 12	--	169 ± 7	424 ± 41
▲	OFF	422 ± 21	--	--	--
○	ON	123 ± 9	408 ± 55	135 ± 11	574 ± 99
●	OFF	128 ± 11	347 ± 49	120 ± 16	--

FIGURE 3.8 Spatial mapping of excitatory and inhibitory inputs to S3 and S5-Gbx2+ ACs

(A) average E/IPSCs at indicated spot sizes in response to 2 Hz square-wave flicker in n= 57 S3 (left) and n=40 S5 (right) Gbx2+ ACs. Blue lines indicate significant differences between spot diameter responses ($p < 0.01$ Student's t test) (B) Area response function from above S3 and S5-Gbx2+ ACs E/IPSCs with absolute maximum and minimum amplitude measurements within the indicated time windows (solid-OFF, and dashed-ON lines) in B fit by a single a single Gaussian or Difference of Gaussian function with indicated widths ± one standard deviation in C.

field stimulus diameters, arguing against it being necessary to suppress S5-Gbx2+ AC voltage responses at larger stimulus diameters.

To study the pre-synaptic inhibitory inputs to S5 cells, we plotted the area response functions for EPSCs and IPSCs during the ON phase of the flicker response. The amplitudes of the EPSCs were fit with a DOG function with center and surround widths of 135 ± 11 and 571 ± 99 µm respectively. The center width of 135 µm suggests the bipolar cell inputs providing excitatory drive to this cell extend out to approximately 270 µm in diameter, which is in line with the dendritic diameter which averaged 258 ± 12 µm (Figure 3.4 E). It is interesting that the 220 µm center size of S5-Gbx2+ ACs measured in current clamp (Figure 3.6 B right panel), was considerably narrower than that of its EPSCs. This 50 µm difference is potentially due to the K^+ based intracellular solution used in current clamp recordings, which was replaced with a Cs^+ based solution in voltage clamp. This may lead to higher K^+ channel leak (because Cs^+ is too large to pass through K^+ channels).This may result in bipolar cell inputs at distal dendrites not being recorded accurately at the level of the soma. Whereas in voltage clamp they would have been. Subsequently we may expect an under-estimate of the distal inputs to S5-Gbx2+ ACs in current clamp.

We found no significant difference between IPSCs at 250 and 1200 µm (Figure 3.8 A upper traces, right panel) It is notable that the S5-Gbx2+ ACs receive such narrow field inhibition. The single Gaussian used to fit the IPSC area response function in Figure 3.8 B, right panel, has a center width of 169 ± 7 µm. This is only ~ 30 µm wider than the excitatory center Gaussian width, suggesting IPSCs are well matched to excitatory inputs. This pattern of balanced inhibition and excitation may be serving to keep the S5 Gbx2 cell in an efficient encoding range.

Many central circuits operate in this manner, with inhibition providing a buffer to cancel out noisy inputs that do not reach above a particular threshold.

GABA receptor mediated inhibition generates S3 and S5-Gbx2+ AC surrounds.

The spatial scale of pre and postsynaptic inhibition summarized in Figure 3.8 C shows that presynaptic inhibition of both S3 and S5-Gbx2+ ACs was fairly wide-field in diameters, while postsynaptic input was narrower for S5 than S3 cells. This led us to ask if the source of pre and postsynaptic inhibition for either cell type was originating from different pharmacologic mechanisms. WFACs are thought to be GABAergic, while narrow-field inhibition tends to be mediated by glycinergic ACs. Furthermore, the two types of ionotropic GABA receptors ($GABA_A$ and $GABA_C$) are thought to be expressed differentially pre and postsynaptically. $GABA_A$ receptors have been found both pre and postsynaptically, on both bipolar cell terminals and on ganglion cell dendrites, while $GABA_C$ receptors are thought to be expressed preferentially on presynaptic bipolar cell terminals. (Vigh and von Gersdorff 2005; Dong and Werblin 1998; Zhang and Slaughter 1995) However, less is known about GABA receptor subtype expression on AC types.

To test if either Gbx2+ AC was receiving $GABA_A$ mediated inhibition, we patched S3 and S5-Gbx2+ ACs isolating inhibitory and excitatory conductance in the same manner as in Figure 3.6 while presenting full-field 2 Hz flickering spot stimuli to maximally activate lateral inhibition. We then then blocked $GABA_A$ receptors with a specific antagonist (20 µM SR-95531) (Figure 3.9 A). In S3-Gbx2+ ACs G_{INH} was completely suppressed by $GABA_A$ receptor block (upper red traces compared to control, Figure 3.9 A_I), indicating S3-Gbx2+ AC express dendritic $GABA_A$ receptors and receive wide-field inhibition. G_{EXC} displayed a bi-phasic response in both S3 and S5-Gbx2+ ACs. We observed that the initial half each stimulus cycle after each contrast transition showed no difference between $GABA_A$ receptor block and control, but in the second half of each stimulus cycle the $GABA_A$ receptor block condition showed suppressed G_{EXC} (Lower traces, Figure 3.9A_{I-II}). To quantify this difference, we averaged the amplitude of the early and late phases of each contrast response, measuring over the first or second 125ms window of G_{EXC} or G_{INH}. Corresponding empty (ON) and filled (OFF) circle (early) or triangle (late) markers are shown in summary plots below the average conductance traces. Blue lines on conductance traces indicate areas of statistical difference ($p < 0.05$) between control and drug conditions, as do *s on summary plots.

One explanation for this late suppression of G_{EXC} is that delayed pre-synaptic inhibition suppresses the sustained component of the bipolar cell response and produces more transient excitation of the S3 and S5-Gbx2+ AC. The sustained BC input that has become more transient under $GABA_A$ block could be expressing $GABA_C$ or Glycine receptors. If this is the case, then blocking $GABA_A$ could increase the presynaptic inhibition of the BC through those $GABA_C$ or Glycine receptors. For that to happen, the source of the $GABA_C$ or Glycine mediated inhibition would itself need to be expressing $GABA_A$ receptors. This type of di-synaptic inhibition is a circuit motif that has been shown to regulate temporal tuning in the retina, and may be helping tune the kinetics of bipolar cell inputs to S3 and S5-Gbx2+ ACs. These pre and postsynaptic mechanisms are illustrated in the proposed minimal circuit diagram in Figure 3.10.

The top traces in Figure 3.9 A_{II} show that blocking $GABA_A$ receptors while recording from S5-Gbx2+ ACs completely suppressed ON pathway inhibition by blocking postsynaptic receptors directly on S5 dendrites. The small OFF phase of G_{INH} was not reduced, suggesting it comes from a non $GABA_A$ mediated source, likely either a glycinergic AC or $GABA_C$ receptor mediated inhibitory input.

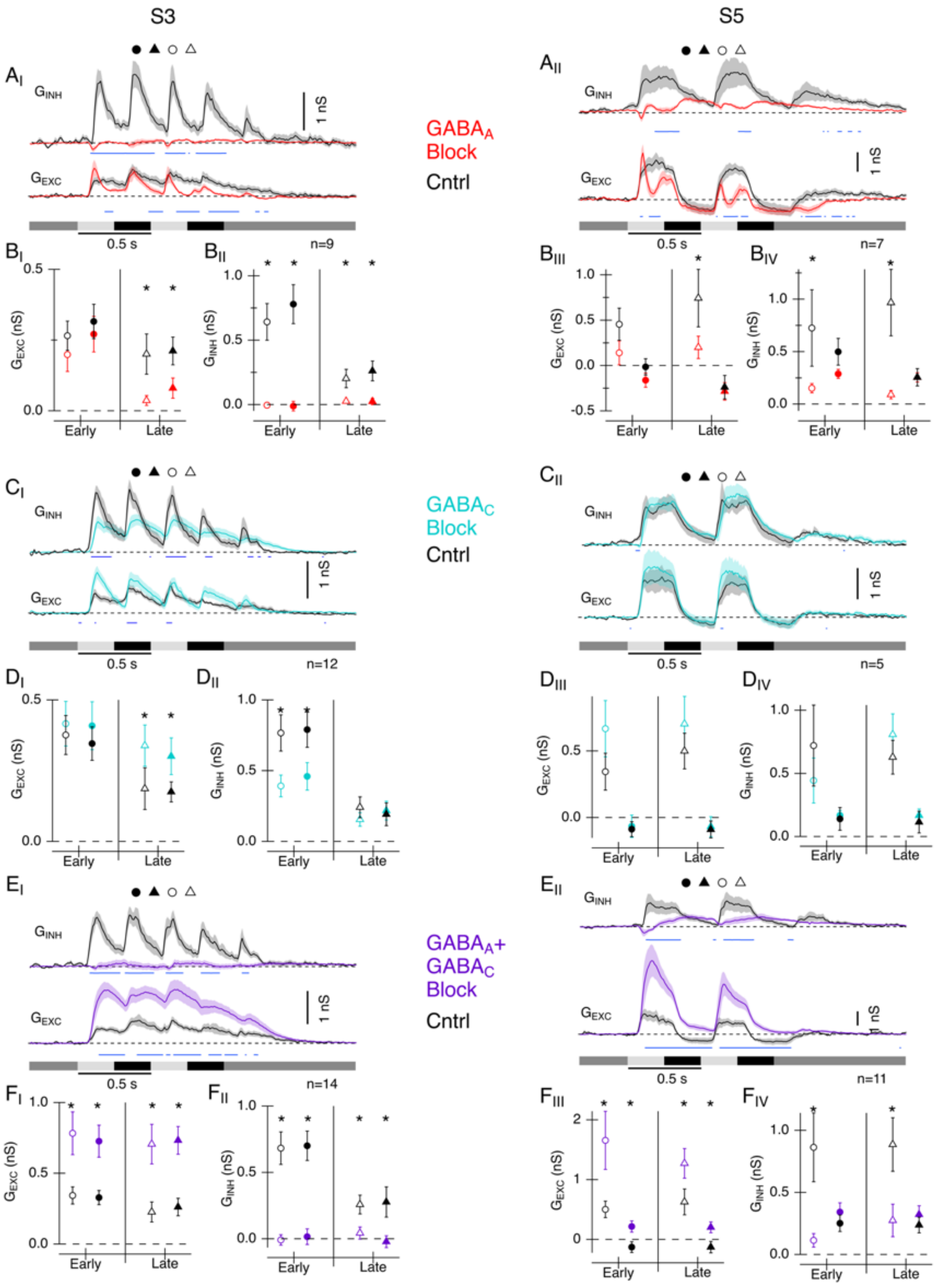

FIGURE 3.9 GABA$_A$ and GABA$_C$ mediated inhibition generates S3 and S5-Gbx2+ AC surrounds

A. Average excitatory (G$_{EXC}$) and inhibitory (G$_{INH}$) conductance during 2Hz flickering full-field stimulus presentation to S3 (A$_I$) and S5 (A$_{II}$) Gbx2+ ACs. Before (black traces) and after (red traces) application of GABA$_A$ receptor block with SR-95531.Blue lines below traces indicate significant differences between control and drug conditions ($p < 0.05$) B$_I$ (S3 cells) and B$_{III}$ (S5 cells): Average amplitude of G$_{EXC}$ during the first 125 ms of light-evoked response (circle markers on left of plot labeled "early") and second 125 ms of light response (triangle markers on right of plot labeled "late") during ON (open markers) and OFF (filled markers) components of the visual stimulus. *'s indicate significant differences between drug and control conditions ($p < 0.05$). C-D and E-F follow same conventions as A-B for conductance traces and amplitude, but the drug condition differs: GABA$_C$ receptor antagonist 50 µM TPMPA used in C-D, 20 µM SR-95531 and 50 µM TPMPA used in E-F to block both GABA$_A$ and GABA$_C$ receptors.

$GABA_C$ receptors have been shown to be present on bipolar cell axon terminals (Vigh and von Gersdorff 2005; Dong and Werblin 1998; Zhang and Slaughter 1995) but we see blocking $GABA_C$ receptors with the specific antagonist 50 μM TPMPA did not significantly increase G_{EXC} in S5-Gbx2+ ACs (Cyan compared to black traces in Figure 3.9, right column). It is possible that the already sustained nature of S5-Gbx2+ AC responses occludes further broadening of their temporal tuning, or $GABA_C$ signaling is blocked by GABAergic ACs under control conditions so there is no effect of $GABA_C$ block.

We did observe a slight increase in presynaptic inhibition (G_{EXC}) in S3-Gbx2+ ACs (Figure 3.9 B_I), particularly in the latter half of each stimulus cycle. This is in line with the late suppression of G_{EXC} observed by blocking $GABA_A$ receptors. If a sustained pre-synaptic bipolar cell input expresses $GABA_C$ receptors and is inhibited under control conditions by a wide-field GABAergic AC, then blocking $GABA_C$ receptors would relieve that BC population of its inhibition. Thus allowing it to increase the sustained excitation of the S3-Gbx2+ cell. Blocking $GABA_A$ and $GABA_C$ receptors individually reveals a complex circuit level regulation of both S3 and S5-Gbx2+ AC responses, particularly with regard to the temporal tuning of the excitatory inputs to these cell types. The different stratification depths of either cell type is also informative here. It is generally thought bipolar cell inputs closer to the middle of the IPL respond in a more transient manner while more peripherally stratifying (closer to S1 and S5) bipolar cells have more sustained kinetics. The result we see in S3 and S5-stratifying Gbx2+ ACs is in line with this notion, and the ability for GABA receptor block to alter how sustained or transient an AC is, means the temporal tuning of bipolar cell inputs to ACs is dependent on GABAergic feedback (Awatramani and Slaughter, 2000; Eggers and Lukasiewicz 2010; Green et al., 2016).

We also wanted to test the combinatorial effects of blocking both receptor subtypes together to identify any glycinergic effects that may be masked by GABAergic inhibition, or if blocking both $GABA_A$ and $GABA_C$ receptors had a combinatorial effect not apparent when blocking them individually. Blocking both $GABA_A$ and $GABA_C$ receptors together resulted in a strong potentiation of the excitatory input to both S3 and S5 cells (Figure 3.9 E-F). Additionally, $GABA_{A+C}$ block did not alter the OFF phase of G_{INH} indicating a potential role for another, non-GABAergic, likely glycinergic diffusely stratifying AC providing inhibition to the S5-Gbx2+ AC. Many glycinergic ACs adhere to this diffuse stratification pattern signaling between vertical strata within the IPL. The proposed glycinergic AC in the S5-Gbx2+ AC circuit (AC3 in the illustration in Figure 3.10) would need to receive input from OFF BCs and form synapses with the S5 cell in ON lamina, thus it is depicted in the model circuit as a bi-stratified cell.

The additive effect of blocking both $GABA_{A+C}$ receptors indicates some degree of circuit interaction between them, with either type impacting S3 and S5-Gbx2+ AC lateral inhibition in distinct manners. There was a clear bias of $GABA_A$ receptors on S3 and S5 Gbx2+ AC dendrites—blocking $GABA_A$ receptors alone eliminated all S3-Gbx2+ AC G_{INH}, and all ON-pathway S5-Gbx2+ AC $G_{INH.}$ These pharmacology experiments also revealed a role for di-synaptic inhibition in regulating the temporal tuning of both cell type's excitatory inputs.

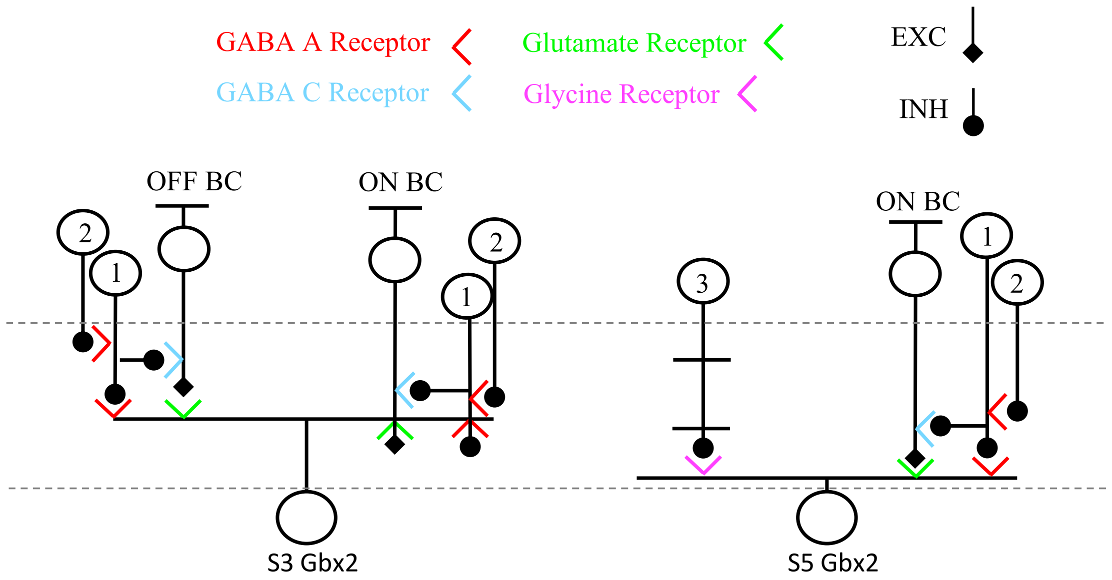

FIGURE 3.10 Proposed minimal circuit diagram that can account for the effects that the GABAergic antagonists have on G_{EXC} and G_{INH}. AC1 provides post-synaptic inhibition to Gbx2+ ACs and pre-synaptic inhibition to AC2 both via GABAA mediated inhibition. AC2 provides pre-synaptic inhibition to BC inputs to Gbx2+ ACs. From the Gbx2 cells' perspective: When GABAA is blocked, direct post-synaptic inhibition is suppressed. AC2 is dis-inhibited and provides stronger pre-synaptic inhibition to Gbx2+ ACs, particularly S3 cells, making them more sustained. S5 cells already respond in a sustained manner, suggesting they cannot become more sustained through GABA$_C$ receptor block. S5 cells also receive additional post-synaptic glycinergic input from an ON-OFF OFF AC (3). Receptor type and neurotransmitters indicated on figure.

Chapter 4: Discussion and Future Directions

The work I presented in this dissertation focusses largely on the presynaptic inputs to genetically identified amacrine cells, and what role these understudied populations may have in shaping retinal output. In Chapter 1 I provided background and context on retinal circuits, with an emphasis on the motifs generating feature selectivity in ganglion cell output channels and how those patterns are more broadly important in signal processing in sensory systems. In Chapter 2 I I used a combination of transgenic mouse lines to target and activate nNOS+ cells and whole-cell electrophysiology to identify the presynaptic inputs that generate the specific postsynaptic output from the NOS2 wide-field amacrine cell. I identified a novel connection to a local motion detecting output channel and provided evidence for the importance of the NOS2 cell in generating this output channel's feature selective spiking pattern. In Chapter 3, I presented a collaborative project alongside the Wright and Sivyer labs that characterized for the first time, the S3 and S5 stratifying Gbx2+ ACs. This project used a combination of genetic labeling strategies, immunofluorescence, RNA sequencing and electrophysiology to isolate and study these populations of interneurons. The data generated from this study establishes a solid foundation for future experiments that will isolate the post-synaptic and gap-junctional output of these interneurons with the goal of identifying their role in vision. Overall, the two projects I presented reveal the complex mechanisms of receptive field structures leveraged by ACs that rely on pre and postsynaptic inhibition. Each cell type, when studied at the single cell level, reveals unique mechanisms that generate their distinct responses. For the remainder of this discussion I will address some of the remaining questions and unanswered aspects of these projects which can hopefully be addressed in future studies.

What is the presynaptic mechanism generating the NOS2 AC's motion preference?

The current study presented in Chapter 2 on NOS+ ACs, particularly with regard to the NOS2 AC's role in LMD GC inhibition, has several interesting next steps to hone in on the role of NOS2 ACs in vision. The current study showed that an inhibitory connection exists between NOS2 ACs and LMD GCs, yet several outstanding questions remain. First, and most readily approachable, is the question of what might the mechanism be to allow the NOS2 AC to respond strongly to global and differential motion, but remain silent during local motion?

The response of NOS2 AC to static spot stimuli gives us two predictions to test. We observed a local inhibitory input to NOS2 ACs that was suppressed at larger stimulus sizes (IPSCs in Figure 2.6 A-B, and G_{INH} in 2.6 F). This inhibitory input may be acting to suppress the response of NOS2 ACs during local motion. Alternately the lack strong excitatory input to NOS2 ACs at small diameter stimuli could be responsible for their lack of strong depolarization seen during local motion (Figure 2.10, magenta trace).

Recording from NOS2 ACs in voltage clamp and presenting the same drifting grating stimuli as were presented to LMD GCs could distinguish between an inhibitory or excitatory mechanism generating the local motion suppression we observed in Figure 2.10. If we observe increased inhibition during local drift that is then suppressed during global or differential motion, then the local inhibitory input we observed with static spot stimuli is likely generating local motion suppression in NOS2 ACs. If excitation increases during global or differential motion, then the larger EPSCs we measured during wide-field stimuli are likely the source of global motion preference in NOS2 ACs. It is also possible these mechanisms are acting additively.

Blocking inhibitory receptors while recording voltage or current responses from NOS2 ACs during local drift could also help address the importance of the local inhibitory input we observed in Figure 2.6. If blocking narrow-field glycinergic inhibition results in increased NOS2 depolarization during local drift, then that local inhibitory input is likely generating local motion suppression. Again, there may be additive effects of inhibitory and excitatory mechanisms, so blocking inhibition may only partially relieve local motion suppression in NOS2 ACs.

Are NOS2 ACs sufficient to generate global motion suppression in LMD GCs?

An open question is to what degree the observed NOS2 AC inhibition found using the NOS-ChR2 optogenetic activation experiment in Figure 2.3 is necessary or sufficient to generate the feature responsive property of global or differential motion suppression in LMD GCs? Based on the known overlapping inhibitory mechanisms observed in the literature, this question is not the most straightforward to address experimentally. As was seen when rendering TH-2 cells unable to package GABA into presynaptic vesicles, inactivating a cell type that was found to provide GABAergic inhibition to the genetically identified W3 GC population only partially reduced the total inhibition to these cells and had a variable effect on motion sensitivity. (Kim et al., 2017) It is possible that even with a perfect inactivating technique to remove NOS2 ACs from the OMS circuit, there still could be redundant mechanisms allowing OMS to still function. Additionally, it is unlikely that we have only targeted a single population of GCs in our study or that the W3 GC line only labels one group of GCs.

An initial study characterizing the W3 genetic label showed a high degree of dendritic overlap such that in total, the brightly labeled cells in the W3-GFP mouse line had a 4x coverage factor such that every area of the retina was contacted by an average of four W3 GCs. (Zhang et al., 2012) This is in line with the 2018 study by Jacoby and Schwartz that found four types of high definition ganglion cells that shared many, but not all, morphological and functional characteristics, notably only two of the four populations showed strong responses during differential motion, the other two were equally suppressed by global and differential motion. This study used a white noise stimulus in which spatial correlations between adjacent pixels in their visual stimulus were removed, so their stimuli did not contain the same information as the vertical or horizontal gratings used in the NOS2 study, leading to potential differences in findings. It is possible that the particular LMD GCs we found a ChR2 evoked NOS2 inhibitory input to represent only a subset of the total high definition cells from the 2018 Jacoby and Schwartz study. Further experiments could replace gratings with white noise to more closely match that study, and a careful tracking of more NOS2-LMD pairs could be mapped onto the functional and morphological data from a large group of cells to see if subdivisions in cell types could be more readily made.

A more high-throughput experimental approach could be attempted in the future to identify functional effects on many GCs at once, or potential pre-synaptic effects of NOS2 AC function which the ChR2 approach used here would miss due to the pharmacological block of photoreceptor driven responses leveraged to identify mono-synaptic events. Using a chemo-genetic (DREADD) or genetically encoded diphtheria toxin receptor (DTR) expressed in NOS+ ACs, we could inactivate these WFACs with moderate temporal precision and monitor BC or GC activity using a genetically encoded calcium indicator line (GCaMP), a bulk loaded calcium indicator (Cal520 or 590-AM), or a glutamate-sensitive fluorescent reporter (iGluSnFR). Each of these readouts have upsides and downsides, but now that an inhibitory connection between NOS2 ACs and LMD GCs has been identified, these would be good next steps towards further defining the functional role of this inhibitory input, all of which could also probe other potential outputs of the NOS2 and NOS1 ACs, the latter of which has only recently had an identified postsynaptic partner of the AII AC. (Park et al., 2020).

Do NOS2 ACs contribute to local motion detection at the behavioral level?

Ultimately, the goal of studying a particular neuron's role at the circuit level is to extrapolate what function it serves at the behavioral level. The cell-specific modulations mentioned above could be used to test if NOS+ ACs have a functionally relevant role in behavior. DREADDs in particular are well suited for behavioral studies in that their agonist (CNO) when applied systemically can inactivate a genetically pre-defined population for a known amount of time, during which a local motion contingent task could be assayed. A recent study used a prey-capture task in which a mouse's natural cricket-hunting behavior was used to assess the role of ipsilaterally projecting GCs in binocularly driven prey-capture. (Johnson et al. 2021) The latency to capture a cricket as well as stereotyped approach, grasp, and biting motions were all measurable components of the behavior that could be assessed before and after NOS+ AC ablation or inactivation. The Johnson et al. 2021 study ablated a subset of ipsi-projecting GCs and found that hunting behavior was impaired. The ablation technique they used was not reversible, so within-group comparisons were not possible. However, using a DREADD based approach they could have been. One would predict if NOS2 ACs have a significant impact on suppressing global motion responses, then their inactivation would lead to impairments in prey detection and capture.

Are S5-Gbx2 ACs the same as CRH-1 ACs?

The S5 laminating GX2+ cells should first be directly compared to the CRH-1 AC (Jacoby et al 2015; Park et al., 2018, Zhu et al., 2014). This could be done using an intersectional approach in which Gbx2 CreERT2-IRES-EGFP mice could be crossed with a Crh-IRES-FlpO line and a dual-recombinase reporter line would selectively label the S5 Gbx2+ AC allowing the direct test of whether they are the same subtype as the CRH-1 ACs. If indeed they are, there are still many unanswered questions as to these CRH-1/Gbx2-S5 cell's function, and the dual recombinase approach would allow selective ablation or functional activation of just these cells, where previous studies of CRH-1 ACs and the current Gbx2+ line alone could not manipulate only one population. It was shown that the CRH-1 AC has a role in providing lateral inhibition to the Suppressed-by-Contrast (SbC) and ON αRGCs (also known as the M4 subtype of intrinsically-photosensitive RGCs (ipRGCs)) (Estevez et al., 2012; Jacoby and Schwartz, 2018; Jacoby et al., 2015; Park et al., 2018). Sublamina 5 also contains the dendrites of M2, M3, and M5 subtypes of ipRGCs, which are involved in visual modalities involved in light avoidance, pupillary reflex, and circadian rhythm behaviors (Schmidt et al., 2011; Sonoda et al., 2020). Having a genetic foothold to manipulate just one population of Gbx2+ ACs with this dual recombinase approach could begin to answer questions about what role these S5 stratifying Gbx2+ cells may have in melanopsin sensing GC circuitry.

Determining the possible role of S3-Gbx2 gap junction mediated output

As the addendum to Chapter 3 suggests, both Gbx2+ ACs have a well-regulated receptive field structure, particularly in the spatial domain. This suggests they are reporting specific spatial information to downstream cells. SbC and on αRGCs in the case of S5 cells, and particular bipolar cell types through gap-junctions or other means in the case of the S3 cells. However, what the nature of this input is and what function it is serving in shaping retinal output is an open question. A first pass at identifying the functional role of the S3 cells could be done using fairly simple, if technically challenging, techniques. Recording pairs of directly apposing bipolar cells and S3 Gbx2+ cells using the same genetic labeling strategy used in Chapter 3, we could probe for potential gap junction by injecting current into either the bipolar cell or S3 Gbx2 and monitoring gap junction mediated voltage changes. Modifying retinal adaptation state (dark vs light adapted retina), or by pre-incubating with a D1R antagonist as in figure 3.5 could allow for improved likelihood of encountering junction coupled cells.

If this approach either fails to find functionally coupled bipolar cells, or even if it does succeed, this does not address if that gap junction mediated output from S3-Gbx2 cells impacts overall retinal output. Genetically encoding a Gbx2 line that does not have functional gap junctions would be a more difficult, but higher throughput approach to identifying the functional impact of S3-Gbx2 gap junctions. Similar approaches have found success in studying the role of connexin 36 (Cx36) in Rod-Cone gap junction mediated signaling, finding removal of these connexins from Cones resulted in altered photoreceptor function. Removing the specific Cx expressed by S3 cells would first involve identifying which Cx is present and then generating a conditional KO would additionally be challenging, but this would allow an overall assessment of GC function with and without gap junctions between BCs and S3-Gbx2 cells present.

Do S3-Gbx2 ACs release neuropeptides?

As was noted in the discussion in Chapter 3, many ACs express neuromodulators and neuropeptides in addition to traditional neurotransmitters. The RNS-seq results from Figure 3.2 showed the S3-Gbx2+ ACs express *Tachykinin 1 (Tac 1)* which encodes substance P, NKA (neurokinin A), neuropeptide K (NPK) and nerupeptide γ (NPγ). While neuropeptides can impact downstream GCs, they are thought to do so on a slower timescale than GABA or glutamate which would make identifying a postsynaptic role for substance P or other neuropeptides a more difficult experimental question. Initially identifying the location of neuropeptide receptors within the IPL would be a start, to see if sublamina 3 is the right location to look for S3-Gbx2+ AC substance P release effects. If a receptor location was found on a particular subset of GCs, using an immunohistochemical approach combined with a sparse ganglion cell labeling strategy to find colocalization, we could proceed to use similar genetic ablation or modification techniques to remove S3-Gbx2+ cells and look for broad scale changes in the subtypes of GCs that express substance P or other neuropeptide receptors. Lastly, recently developed for drosophila, Neuropeptide Release Reporters (NPRRs) could be developed to directly report the location and release of substance P from S3-Gbx2+ ACs. (Ding et al., 2019)

Summary and Conclusions

The retina is tasked with a difficult balancing act. It must transmit a large volume of visual information from moment to moment through the bottleneck of the optic nerve. It does this with a digital signal of action potential trains through the 60,000 ganglion cell axons in mouse, 1 million in primates. The retina attempts to solve this predicament through a division of labor, sorting light into feature specific channels so it can transmit information in roughly 40 parallel output pathways. The mechanism underlying this decorrelation of homogenous input falls largely on the diverse population of amacrine cells providing mostly inhibitory, but also neuropeptide and gap junctional input through feedback and feedforward input to other circuit components within the retina. It is by understanding the distinct receptive field properties of amacrine cells, several of which I have studied in detail in this dissertation, that we can appreciate their critical roles in determining the feature selectivity of the specific ganglion channel outputs in the retina.

REFERENCES

Awatramani, G. B., and Slaughter, M. M. (2000). Origin of transient and sustained responses in ganglion cells of the retina. J. Neurosci. 20(18), 7087–7095.

Baccus S.A., Olveczky B.P., Manu M, and Meister M. (2008). A retinal circuit that computes object motion. J. Neurosci. 28(27), 6807–6817.

Badea, T.C. and Nathans, J. (2004). Quantitative analysis of neuronal morphologies in the mouse retina visualized by using a genetically directed reporter. J. Comp. Neurol. 480(4), 331-351.

Baden, T., Berens, P., Franke, K., Román Rosón, M., Bethge, M., and Euler, T. (2016). The functional diversity of retinal ganglion cells in the mouse. Nature, 529(7586), 345–350.

Barlow, H. B., Hill, R. M., and Levick, W. R. (1964). Retinal ganglion cells responding selectively to direction and speed of image motion in the rabbit. J. Physiol. 173(3), 377–407.

Barlow, H. B., and Levick, W. R. (1965). The mechanism of directionally selective units in rabbit's retina. J. Physiol. 178(3), 477–504.

Bastian, J., Chacron, M. J., and Maler, L. (2002). Receptive field organization determines pyramidal cell stimulus-encoding capability and spatial stimulus selectivity. J. Neurosci. 22(11), 4577–4590.

Battaglini, P. P., Galletti, C., Aicardi, G., Squatrito, S., and Maioli, M. G. (1986). Effect of fast moving stimuli and saccadic eye movements on cell activity in visual areas V1 and V2 of behaving monkeys. Arch. Ital. Biol. 124(2), 111-119.

Benjamini, Y., and Hochberg, Y. (1995). Controlling the False Discovery Rate: A Practical and Powerful Approach to Multiple Testing. Journal of the Royal Statistical Society Series B (Methodological) 57, 289-300.

Bloomfield, S.A., and Volgyi, B. (2009). The diverse functional roles and regulation of neuronal gap junctions in the retina. Nat Rev Neurosci 10(7), 495-506.

Bolger, A.M., Lohse, M., and Usadel, B. (2014). Trimmomatic: a flexible trimmer for Illumina sequence data. Bioinformatics 30(15), 2114-2120.

Brecha, N., Johnson, D., Peichl, L., and Wassle, H. (1988). Cholinergic amacrine cells of the rabbit retina contain glutamate decarboxylase and gamma-aminobutyrate immunoreactivity. Proc Natl Acad Sci USA 85(16), 6187-6191.

Bridgeman B. (1972). Visual receptive fields sensitive to absolute and relative motion during tracking. Science 178, 1106–1108 (1972).

Brüggen, B., Meyer, A., Boven, F., Weiler, R., & Dedek, K. (2015). Type 2 wide-field amacrine cells in TH::GFP mice show a homogenous synapse distribution and contact small ganglion cells. The European journal of neuroscience, 41(6), 734–747.

Chatterjee, M., Li, K., Chen, L., Maisano, X., Guo, Q., Gan, L., and Li, J.Y. (2012). Gbx2 regulates thalamocortical axon guidance by modifying the LIM and Robo codes. Development 139, 4633-4643.

Chen, L., Chatterjee, M., and Li, J.Y. (2010). The mouse homeobox gene Gbx2 is required for the development of cholinergic interneurons in the striatum. J Neurosci 30, 14824-14834.

Chen, L., Guo, Q., and Li, J.Y. (2009). Transcription factor Gbx2 acts cell-nonautonomously to regulate the formation of lineage-restriction boundaries of the thalamus. Development 136, 1317-1326.

Chen, Y., Lun, A.T., and Smyth, G.K. (2016). From reads to genes to pathways: differential expression analysis of RNA-Seq experiments using Rsubread and the edgeR quasi-likelihood pipeline. F1000Res 5, 1438.

Cherry, T.J., Trimarchi, J.M., Stadler, M.B., and Cepko, C.L. (2009). Development and diversification of retinal amacrine interneurons at single cell resolution. Proc Natl Acad Sci USA 106, 9495-9500.

Dacey, D.M. (1999). Primate retina: cell types, circuits and color opponency. Progress in Retinal and Eye Research 18(6), 737–763.

Daigle, T.L., Madisen, L., Hage, T.A., Valley, M.T., Knoblich, U., Larsen, R.S., Takeno, M.M., Huang, L., Gu, H., Larsen, R., et al. (2018). A Suite of Transgenic Driver and Reporter Mouse Lines with Enhanced Brain-Cell-Type Targeting and Functionality. Cell 174, 465-480 e422.

DeLuca, D.S., Levin, J.Z., Sivachenko, A., Fennell, T., Nazaire, M.D., Williams, C., Reich, M., Winckler, W., and Getz, G. (2012). RNA-SeQC: RNA-seq metrics for quality control and process optimization. Bioinformatics 28(11), 1530-1532.

Demb, J. B., and Singer, J. H. (2012). Intrinsic properties and functional circuitry of the AII amacrine cell. Visual neuroscience, 29(1), 51–60.

DeVries, S.H., and Baylor, D.A. (1997). Mosaic arrangement of ganglion cell receptive fields in rabbit retina. J. Neurophysiol. 78(4), 2048–2060

DeVries, S.E., Baccus, S.A., and Meister, M. (2011) The projective field of a retinal Amacrine cell. Journal of Neuroscience, 31(23) 8595-8604

Diamond, J.S. (2017). Inhibitory Interneurons in the Retina: Types, Circuitry, and Function. Annu Rev Vis Sci 3, 1-24.

Ding, K., Han, Y., Seid, T. W., Buser, C., Karigo, T., Zhang, S., Dickman, D. K., and Anderson, D. J. (2019). Imaging neuropeptide release at synapses with a genetically engineered reporter. eLife, 8, e46421.

Dobin, A., Davis, C.A., Schlesinger, F., Drenkow, J., Zaleski, C., Jha, S., Batut, P., Chaisson, M., and Gingeras, T.R. (2013). STAR: ultrafast universal RNA-seq aligner. Bioinformatics 29, 15-21.

Eccles, J.C.; Fatt P.; Koketsu K. (1954). Cholinergic and inhibitory synapses in a pathway from motor-axon collaterals to motoneurones. J Physiol. 126(3): 524–62.

Eggers, E. D., and Lukasiewicz, P. D. (2011). Multiple pathways of inhibition shape bipolar cell responses in the retina. Visual neuroscience, 28(1), 95–108.

Eggers E.D., McCall M.A. and Lukasiewicz P.D. (2007). Presynaptic inhibition differentially shapes transmission in distinct circuits in the mouse retina. J Physiol. 582(2), 569–582.

Engstrom, P.G., Steijger, T., Sipos, B., Grant, G.R., Kahles, A., Ratsch, G., Goldman, N., Hubbard, T.J., Harrow, J., Guigo, R., et al. (2013). Systematic evaluation of spliced alignment programs for RNA-seq data. Nat Methods 10, 1185-1191.

Estevez, M.E., Fogerson, P.M., Ilardi, M.C., Borghuis, B.G., Chan, E., Weng, S., Auferkorte, O.N., Demb, J.B., and Berson, D.M. (2012). Form and function of the M4 cell, an intrinsically photosensitive retinal ganglion cell type contributing to geniculocortical vision. J Neurosci 32, 13608-13620.

Ewels, P., Magnusson, M., Lundin, S., and Kaller, M. (2016). MultiQC: summarize analysis results for multiple tools and samples in a single report. Bioinformatics 32, 3047-3048.

Famiglietti E.V., Kolb H. (1975). A bistratified amacrine cell and synaptic circuitry in the inner plexiform layer of the retina. Brain Res. 1975; 84(2), 293–300.

Fischer, B., Boch, R., and Bach, M. (1981). Stimulus versus eye movements: comparison of neural activity in the striate and prelunate visual cortex (A17 and A19) of trained rhesus monkey. Experimental brain research, 43(1), 69–77.

Fried, S. I., Munch, T. A. and Werblin, F. S. (2002) Mechanisms and circuitry underlying directional selectivity in the retina. Nature 420, 411–414.

Galletti, C., Squatrito, S., Battaglini, P. P., and Grazia Maioli, M. (1984). 'Real-motion' cells in the primary visual cortex of macaque monkeys. Brain research, 301(1), 95–110.

Goldstein, I. M., Ostwald, P., and Roth, S. (1996). Nitric oxide: a review of its role in retinal function and disease. Vision research, 36(18), 2979–2994.

Graydon, C. W., Lieberman, E. E., Rho, N., Briggman, K. L., Singer, J. H., and Diamond, J. S. (2018). Synaptic Transfer between Rod and Cone Pathways Mediated by AII Amacrine Cells in the Mouse Retina. Current biology : CB, 28(17), 2739–2751.e3.

Greene, M. J., Kim, J. S., Seung, H. S., and EyeWirers (2016). Analogous Convergence of Sustained and Transient Inputs in Parallel On and Off Pathways for Retinal Motion Computation. Cell reports, 14(8), 1892–1900.

Grimes, W. N., Seal, R. P., Oesch, N., Edwards, R. H., and Diamond, J. S. (2011). Genetic targeting and physiological features of VGLUT3+ amacrine cells. Visual neuroscience, 28(5), 381–392.

Grimes, W. N., Zhang, J., Graydon, C. W., Kachar, B., and Diamond, J. S. (2010). Retinal parallel processors: more than 100 independent microcircuits operate within a single interneuron. Neuron, 65(6), 873–885.

Hampson, E.C., Vaney, D.I., and Weiler, R. (1992). Dopaminergic modulation of gap junction permeability between amacrine cells in mammalian retina. J Neurosci 12(12), 4911-4922.

Haverkamp, S., and Wassle, H. (2004). Characterization of an amacrine cell type of the mammalian retina immunoreactive for vesicular glutamate transporter 3. J Comp Neurol 468, 251-263.

He, L., Gulyanon, S., Mihovilovic Skanata, M., Karagyozov, D., Heckscher, E.S., Krieg, M., Tsechpenakis, G., Gershow, M., and Tracey, W.D., Jr. (2019). Direction Selectivity in Drosophila Proprioceptors Requires the Mechanosensory Channel Tmc. Curr Biol 29, 945-956 e943.

Helmstaedter, M., Briggman, K.L., Turaga, S.C., Jain, V., Seung, H.S. and Denk, W. (2013) Connectomic reconstruction of the inner plexiform layer in the mouse retina. Nature, 500, 168-174

Hoggarth, A., McLaughlin, A. J., Ronellenfitch, K., Trenholm, S., Vasandani, R., Sethuramanujam, S., Schwab, D., Briggman, K. L., and Awatramani, G. B. (2015). Specific wiring of distinct amacrine cells in the directionally selective retinal circuit permits independent coding of direction and size. Neuron, 86(1), 276–291.

Hu E.H. and Bloomfield S.A. (2003) Gap junctional coupling underlies the short-latency spike synchrony of retinal alpha ganglion cells. J Neurosci 23(17), 6768–6777.

Huang X., Rangel M., Briggman K.L., and Wei W. (2019) Neural mechanisms of contextual modulation in the retinal direction selective circuit. Nat Commun. 10(1):2431.

Hubel, D.H., and Wiesel, T.N. (1962). Receptive fields, binocular interaction and functional architecture in the cat's visual cortex. The Journal of Physiology 160(1), 106–154.

Jackman, S. L., Choi, S. Y., Thoreson, W. B., Rabl, K., Bartoletti, T. M., and Kramer, R. H. (2009). Role of the synaptic ribbon in transmitting the cone light response. Nature neuroscience, 12(3), 303–310.

Jacoby, J., Nath, A., Jessen, Z.F., and Schwartz, G.W. (2018). A Self-Regulating Gap Junction Network of Amacrine Cells Controls Nitric Oxide Release in the Retina. Neuron 100, 1149-1162.e5.

Jacoby, J., and Schwartz, G.W. (2018). Typology and Circuitry of Suppressed-by-Contrast Retinal Ganglion Cells. Front Cell Neurosci 12, 269.

Jacoby, J., Zhu, Y., DeVries, S.H., and Schwartz, G.W. (2015). An Amacrine Cell Circuit for Signaling Steady Illumination in the Retina. Cell Rep 13, 2663-2670.

Johnson, J., Sherry, D.M., Liu, X., Fremeau, R.T., Jr., Seal, R.P., Edwards, R.H., and Copenhagen, D.R. (2004). Vesicular glutamate transporter 3 expression identifies glutamatergic amacrine cells in the rodent retina. J Comp Neurol 477, 386-398.

Johnson, K. P., Fitzpatrick, M. J., Zhao, L., Wang, B., McCracken, S., Williams, P. R., and Kerschensteiner, D. (2021). Cell-type-specific binocular vision guides predation in mice. Neuron, 109(9), 1527–1539.e4.

Kaneko, A. (1970). Physiological and morphological identification of horizontal, bipolar and amacrine cells in goldfish retina. J. Physiol. 207, 623-633.

Kanjhan, R., and Vaney, D.I. (2008). Semi-loose seal Neurobiotin electroporation for combined structural and functional analysis of neurons. Pflugers Arch 457, 561-568.

Kay, J.N., Voinescu, P.E., Chu, M.W., and Sanes, J.R. (2011). Neurod6 expression defines new retinal amacrine cell subtypes and regulates their fate. Nat Neurosci 14, 965-972.

Keeley, P. W., Eglen, S. J., and Reese, B. E. (2020). From random to regular: Variation in the patterning of retinal mosaics. The Journal of comparative neurology, 528(13), 2135–2160.

Kenyon GT, Marshak DW (1998) Gap junctions with amacrine cells provide a feedback pathway for ganglion cells within the retina. Proc Biol Sci 265:919–925.

Kim, I.J., Zhang, Y., Yamagata, M., Meister, M., and Sanes, J.R. (2008). Molecular identification of a retinal cell type that responds to upward motion. Nature 452, 478-482.

Kim, J.I., Ganesan, S., Luo, S.X., Wu, Y.W., Park, E., Huang, E.J., Chen, L., and Ding, J.B. (2015). Aldehyde dehydrogenase 1a1 mediates a GABA synthesis pathway in midbrain dopaminergic neurons. Science 350, 102-106.

Kim, T. and Kerschensteiner, D. (2017), Inhibitory Control of Feature Selectivity in an Object Motion Sensitive Circuit of the Retina. Cell Reports 19*,* 1343-1350.

Kim, T., Shen, N., Hsiang, J. C., Johnson, K. P., and Kerschensteiner, D. (2020). Dendritic and parallel processing of visual threats in the retina control defensive responses. Science advances, 6 (47), 9920.

Knop, G. C., Feigenspan, A., Weiler, R., and Dedek, K. (2011). Inputs underlying the ON-OFF light responses of type 2 wide-field amacrine cells in TH::GFP mice. J Neurosci. 32(13), 4780-4791.

Knudsen, E.I, and Konishi, M. (1978). Center-surround organization of auditory receptive fields in the owl. Science 202, 778–780.

Koike, C., Obara, T., Uriu, Y., Numata, T., Sanuki, R., Miyata, K., Koyasu, T., Ueno, S., Funabiki, K., Tani, A., Ueda, H., Kondo, M., Mori, Y., Tachibana, M., & Furukawa, T. (2010). TRPM1 is a component of the retinal ON bipolar cell transduction channel in the mGluR6 cascade. Proc Natl Acad Sci USA, 107(1), 332–337.

Kolb, H., and Famiglietti, E. V. (1974). Rod and cone pathways in the inner plexiform layer of cat retina. Science 186(4158), 47–49.

Krishnaswamy, A., Yamagata, M., Duan, X., Hong, Y.K. and Sanes, J.R. (2015) Sidekick 2 directs formation of a retinal circuit that detects differential motion. Nature, 524, 466-470.

Law, C.W., Chen, Y., Shi, W., and Smyth, G.K. (2014). voom: Precision weights unlock linear model analysis tools for RNA-seq read counts. Genome Biol 15, R29.

Lee, S., Chen, L., Chen, M., Ye, M., Seal, R.P., and Zhou, Z.J. (2014). An unconventional glutamatergic circuit in the retina formed by vGluT3 amacrine cells. Neuron 84, 708-715.

Lefebvre, J.L., Sanes, J.R., and Kay, J.N. (2015). Development of dendritic form and function. Annu Rev Cell Dev Biol 31, 741-777.

Li, S., Woodfin, M., Long, S.S., and Fuerst, P.G. (2016). IPLaminator: an ImageJ plugin for automated binning and quantification of retinal lamination. BMC Bioinformatics 17, 36.

Lin, B. and Masland, R.H. (2006) Populations of wide-field amacrine cells in the mouse retina. J Comp Neurol, 499, 797-809

Liu, J., Reggiani, J.D.S., Laboulaye, M.A., Pandey, S., Chen, B., Rubenstein, J.L.R., Krishnaswamy, A., and Sanes, J.R. (2018). Tbr1 instructs laminar patterning of retinal ganglion cell dendrites. Nat Neurosci 21, 659-670.

Liu, J., and Sanes, J.R. (2017). Cellular and Molecular Analysis of Dendritic Morphogenesis in a Retinal Cell Type That Senses Color Contrast and Ventral Motion. J Neurosci 37, 12247-12262.

Luu, B., Ellisor, D., and Zervas, M. (2011). The lineage contribution and role of Gbx2 in spinal cord development. PLoS One 6, e20940.

MacNeil, M.A., Heussy, J.K., Dacheux, R.F., Raviola, E., and Masland, R.H. (1999). The shapes and numbers of amacrine cells: matching of photofilled with Golgi-stained cells in the rabbit retina and comparison with other mammalian species. J Comp Neurol 413, 305-326.

MacNeil, M.A., and Masland, R.H. (1998). Extreme diversity among amacrine cells: implications for function. Neuron 20, 971-982.

Macosko, E. Z., Basu, A., Satija, R., Nemesh, J., Shekhar, K., Goldman, M., Tirosh, I., Bialas, A. R., Kamitaki, N., Martersteck, E. M., Trombetta, J. J., Weitz, D. A., Sanes, J. R., Shalek, A. K., Regev, A., and McCarroll, S. A. (2015). Highly Parallel Genome-wide Expression Profiling of Individual Cells Using Nanoliter Droplets. Cell, 161(5), 1202–1214.

Madisen, L., Zwingman, T.A., Sunkin, S.M., Oh, S.W., Zariwala, H.A., Gu, H., Ng, L.L., Palmiter, R.D., Hawrylycz, M.J., Jones, A.R., et al. (2010). A robust and high-throughput Cre reporting and characterization system for the whole mouse brain. Nat Neurosci 13, 133-140.

Mallika, C., Guo, Q., and Li, J.Y. (2015). Gbx2 is essential for maintaining thalamic neuron identity and repressing habenular characters in the developing thalamus. Dev Biol 407, 26-39.

Manookin, M. B., Beaudoin, D. L., Ernst, Z. R., Flagel, L. J., and Demb, J. B. (2008). Disinhibition combines with excitation to extend the operating range of the OFF visual pathway in daylight.J Neurosci. 28(16), 4136-50.

Marr, D., and Hildreth, E. (1980). Theory of edge detection. Proceedings of the Royal Society of London. Series B, Biological sciences, 207(1167), 187–217.

Masland R. H. (2001). The fundamental plan of the retina. Nature neuroscience, 4(9), 877-886.

McGuire, B. A., Stevens, J. K., and Sterling, P. (1984). Microcircuitry of bipolar cells in cat retina. The Journal of neuroscience, 4(12), 2920–2938.

McLaughlin, A. J., Percival, K. A., Gayet-Primo, J., and Puthussery, T. (2021). Glycinergic Inhibition Targets Specific Off Cone Bipolar Cells in Primate Retina. eNeuro, 8(1), ENEURO.0432-20.2020.

Morgans, C. W., Brown, R. L., & Duvoisin, R. M. (2010). TRPM1: the endpoint of the mGluR6 signal transduction cascade in retinal ON-bipolar cells. Bioessays, 32(7) 609-614.

Morgans, C. W., Zhang, J., Jeffrey, B. G., Nelson, S. M., Burke, N. S., Duvoisin, R. M., & Brown, R. L. (2009). TRPM1 is required for the depolarizing light response in retinal ON-bipolar cells. Proc Natl Acad Sci USA, 106(45), 19174–19178.

Morrie, R. D., and Feller, M. B. (2018). A Dense Starburst Plexus Is Critical for Generating Direction Selectivity. Current biology : CB, 28(8), 1204–1212.e5.

Murphy, G. J., and Rieke, F. (2008). Signals and noise in an inhibitory interneuron diverge to control activity in nearby retinal ganglion cells. Nature neuroscience, 11(3), 318–326.

Nelson, J.W., Sklenar, J., Barnes, A.P., and Minnier, J. (2017). The START App: a web-based RNAseq analysis and visualization resource. Bioinformatics 33, 447-449.

Newkirk, G.S., Hoon, M., Wong, R.O., and Detwiler, P.B. (2013). Inhibitory inputs tune the light response properties of dopaminergic amacrine cells in mouse retina. J Neurophysiol 110, 536-552.

O'Brien, J., and Bloomfield, S.A. (2018). Plasticity of Retinal Gap Junctions: Roles in Synaptic Physiology and Disease. Annu Rev Vis Sci 4, 79-100.

Olveczky, B. P., Baccus, S. A., & Meister, M. (2007). Retinal adaptation to object motion. Neuron, 56 (4), 689–700.

Olveczky, B. P., Baccus, S. A., & Meister, M. (2003). Segregation of object and background motion in the retina. Nature, 423 (6938), 401–408

Park, S.J.H., Lieberman, E.E., Ke, J. Bin, Rho, N., Ghorbani, P., Rahmani, P., Jun, N.Y., Lee, H.L., Kim, I.J., Briggman, K.L. (2020). Connectomic analysis reveals an interneuron with an integral role in the retinal circuit for night vision. Elife 9, 1–27.

Park, S.J.H., Pottackal, J., Ke, J.-B., Jun, N.Y., Rahmani, P., Kim, I.-J., Singer, J.H., and Demb, J.B. (2018). Convergence and Divergence of CRH Amacrine Cells in Mouse Retinal Circuitry. J. Neurosci. 38, 3753–3766.

Peirce, J.W. (2007). PsychoPy–Psychophysics software in Python. J. Neurosci. Methods 162, 8–13.

Peng, Y.R., James, R.E., Yan, W., Kay, J.N., Kolodkin, A.L., and Sanes, J.R. (2020). Binary Fate Choice between Closely Related Interneuronal Types Is Determined by a Fezf1-Dependent Postmitotic Transcriptional Switch. Neuron 105, 464-474 e466.

Peng, Y.R., Shekhar, K., Yan, W., Herrmann, D., Sappington, A., Bryman, G.S., van Zyl, T., Do, M.T.H., Regev, A., and Sanes, J.R. (2019). Molecular Classification and Comparative Taxonomics of Foveal and Peripheral Cells in Primate Retina. Cell 176, 1222-1237 e1222.

Peng, Y.R., Tran, N.M., Krishnaswamy, A., Kostadinov, D., Martersteck, E.M., and Sanes, J.R. (2017). Satb1 Regulates Contactin 5 to Pattern Dendrites of a Mammalian Retinal Ganglion Cell. Neuron 95, 869-883 e866.

Pitulescu, M.E., Schmidt, I., Benedito, R., and Adams, R.H. (2010). Inducible gene targeting in the neonatal vasculature and analysis of retinal angiogenesis in mice. Nat Protoc 5, 1518-1534.

Ramón y Cajal, S. (1893) La Cellule 9, 119-257 English translation (1972) by S. A. Thorpe and M. Glickstein in The Structure of the Retina C. Thomas

Ravello, C.R., Perrinet, L.U., Escobar, MJ. and Placios, AG. (2019). Speed-Selectivity in Retinal Ganglion Cells is Sharpened by Broad Spatial Frequency, Naturalistic Stimuli. Sci Rep 9, 456.

Roy, K., Kumar, S., and Bloomfield, S. A. (2017). Gap junctional coupling between retinal amacrine and ganglion cells underlies coherent activity integral to global object perception. Proc. Natl. Acad. Sci. U.S.A. 114, E10484–E10493.

Rheaume, B.A., Jereen, A., Bolisetty, M., Sajid, M.S., Yang, Y., Renna, K., Sun, L., Robson, P., and Trakhtenberg, E.F. (2018). Single cell transcriptome profiling of retinal ganglion cells identifies cellular subtypes. Nat Commun 9, 2759.

Ritchie, M.E., Phipson, B., Wu, D., Hu, Y., Law, C.W., Shi, W., and Smyth, G.K. (2015). limma powers differential expression analyses for RNA-sequencing and microarray studies. Nucleic Acids Res 43, e47.

Rockhill, R.L., Euler, T., and Masland, R.H. (2000). Spatial order within but not between types of retinal neurons. Proc. Natl. Acad. Sci. USA 97(5), 2303–2307

Rodieck, R.W. (1991). The density recovery profile: a method for the analysis of points in the plane applicable to retinal studies. Vis Neurosci 6, 95-111.

Rosa JM, Morrie RD, Baertsch HC, Feller MB. (2016) Contributions of Rod and Cone Pathways to Retinal Direction Selectivity Through Development. J Neurosci. Sep 14;36(37)

Roska, B., and Werblin, F. (2001). Vertical interactions across ten parallel, stacked representations in the mammalian retina. Nature 410, 583-587.

Sanes, J. R., and Masland, R. H. (2015). The types of retinal ganglion cells: current status and implications for neuronal classification. Annual review of neuroscience, 38, 221–246.

Saunders, A., Macosko, E.Z., Wysoker, A., Goldman, M., Krienen, F.M., de Rivera, H., Bien, E., Baum, M., Bortolin, L., Wang, S., et al. (2018). Molecular Diversity and Specializations among the Cells of the Adult Mouse Brain. Cell 174, 1015-1030 e1016.

Schindelin, J., Arganda-Carreras, I., Frise, E., Kaynig, V., Longair, M., Pietzsch, T., Preibisch, S., Rueden, C., Saalfeld, S., Schmid, B., et al. (2012). Fiji: an open-source platform for biological-image analysis. Nat Methods 9, 676-682.

Schmidt, T.M., Chen, S.K., and Hattar, S. (2011). Intrinsically photosensitive retinal ganglion cells: many subtypes, diverse functions. Trends Neurosci 34, 572-580.

Schneeweis, D. M., and Schnapf, J. L. (2000). Noise and light adaptation in rods of the macaque monkey. Visual neuroscience, 17(5), 659–666.

Schwab, M.H., Bartholomae, A., Heimrich, B., Feldmeyer, D., Druffel-Augustin, S., Goebbels, S., Naya, F.J., Zhao, S., Frotscher, M., Tsai, M.J., et al. (2000). Neuronal basic helix-loop-helix proteins (NEX and BETA2/Neuro D) regulate terminal granule cell differentiation in the hippocampus. J Neurosci 20, 3714-3724.

Sharpe LT, Fach C, Nordby K, Stockman A (1989b) The incremental threshold of the rod visual system and Weber's law. Science 244, 354-356

Shekhar, K., Lapan, S.W., Whitney, I.E., Tran, N.M., Macosko, E.Z., Kowalczyk, M., Adiconis, X., Levin, J.Z., Nemesh, J., Goldman, M., et al. (2016). Comprehensive Classification of Retinal Bipolar Neurons by Single-Cell Transcriptomics. Cell 166, 1308-1323 e1330.

Siegert, S., Scherf, B.G., Del Punta, K., Didkovsky, N., Heintz, N., and Roska, B. (2009). Genetic address book for retinal cell types. Nat Neurosci 12, 1197-1204.

Sivyer, B., and Vaney, D.I. (2010). Dendritic morphology and tracer-coupling pattern of physiologically identified transient uniformity detector ganglion cells in rabbit retina. Vis Neurosci 27, 159-170.

Sonoda, T., Okabe, Y., and Schmidt, T.M. (2020). Overlapping morphological and functional properties between M4 and M5 intrinsically photosensitive retinal ganglion cells. J Comp Neurol 528, 1028-1040.

Soto, F., Tien, N.W., Goel, A., Zhao, L., Ruzycki, P.A. and Kerschensteiner, D. (2019) AMIGO2 Scales Dendrite Arbors in the Retina. *Cell Rep*, **29**, 1568-1578 e1564.PMC6871773

Sun, L.O., Jiang, Z., Rivlin-Etzion, M., Hand, R., Brady, C.M., Matsuoka, R.L., Yau, K.W., Feller, M.B. and Kolodkin, A.L. (2013) On and off retinal circuit assembly by divergent molecular mechanisms. Science, 342, 1241974.PMC3863450

Szikra, T., Trenholm, S., Drinnenberg, A., Jüttner, J., Raics, Z., Farrow, K., Biel, M., Awatramani, G., Clark, D. A., Sahel, J. A., da Silveira, R. A., and Roska, B. (2014). Rods in daylight act as relay cells for cone-driven horizontal cell-mediated surround inhibition. Nature neuroscience, 17(12), 1728–1735.

Tasic, B., Yao, Z., Graybuck, L.T., Smith, K.A., Nguyen, T.N., Bertagnolli, D., Goldy, J., Garren, E., Economo, M.N., Viswanathan, S., et al. (2018). Shared and distinct transcriptomic cell types across neocortical areas. Nature 563, 72-78.

Taylor, W. R., and Vaney, D. I. (2002). Diverse synaptic mechanisms generate direction selectivity in the rabbit retina. J. Neurosci. 22(17), 7712–7720.

Tien NW, Pearson JT, Heller CR, Demas J, Kerschensteiner D (2015) Genetically identified suppressed-by-contrast retinal ganglion cells reliably signal self-generated visual stimuli. J Neurosci 35:10815–10820.

Tien, N. W., Kim, T., and Kerschensteiner, D. (2016). Target-Specific Glycinergic Transmission from VGluT3-Expressing Amacrine Cells Shapes Suppressive Contrast Responses in the Retina. Cell reports, 15(7), 1369–1375.

Tikidji-Hamburyan, A., Reinhard, K., Storchi, R., Dietter, J., Seitter, H., Davis, K. E., Idrees, S., Mutter, M., Walmsley, L., Bedford, R. A., Ueffing, M., Ala-Laurila, P., Brown, T. M., Lucas, R. J., and Münch, T. A. (2017). Rods progressively escape saturation to drive visual responses in daylight conditions. Nature communications, 8(1), 1813.

Tran, N.M., Shekhar, K., Whitney, I.E., Jacobi, A., Benhar, I., Hong, G., Yan, W., Adiconis, X., Arnold, M.E., Lee, J.M., Levin, J.Z., Lin, D., Wang, C., Lieber, C.M., Regev, A., He, Z. and Sanes, J.R. (2019) Single-Cell Profiles of Retinal Ganglion Cells Differing in Resilience to Injury Reveal Neuroprotective Genes. Neuron, 104, 1039-1055 e1012.PMC6923571

Tritsch, N.X., Ding, J.B., and Sabatini, B.L. (2012). Dopaminergic neurons inhibit striatal output through non-canonical release of GABA. Nature 490, 262-266.

Tritsch, N.X., Oh, W.J., Gu, C., and Sabatini, B.L. (2014). Midbrain dopamine neurons sustain inhibitory transmission using plasma membrane uptake of GABA, not synthesis. Elife 3, e01936.

Tsukamoto, Y., and Omi, N. (2017). Classification of Mouse Retinal Bipolar Cells: Type-Specific Connectivity with Special Reference to Rod-Driven AII Amacrine Pathways. Frontiers in neuroanatomy, 11, 92.

Whitney, I.E., Keeley, P.W., St John, A.J., Kautzman, A.G., Kay, J.N., and Reese, B.E. (2014). Sox2 regulates cholinergic amacrine cell positioning and dendritic stratification in the retina. J Neurosci 34, 10109-10121.

Usrey, W.M., and Alitto, H.J. (2015). Visual functions of the thalamus. Annual Review of Vision Science 1, 351–371.

van Wyk, M., Taylor, W.R., Vaney, D.I. (2006). Local edge detectors: a substrate for fine spatial vision at low temporal frequencies in rabbit retina. J Neurosci 26, 13250-13263.

van Wyk M, Wässle H & Taylor WR (2009). Receptive field properties of ON- and OFF-ganglion cells in the mouse retina. Vis Neurosci 26, 297–308.

Vaney D. I. (1991). Many diverse types of retinal neurons show tracer coupling when injected with biocytin or Neurobiotin. Neuroscience letters, 125(2), 187–190.

Vaney, D. I., and Weiler, R. (2000). Gap junctions in the eye: evidence for heteromeric, heterotypic and mixed-homotypic interactions. Brain research. Brain research reviews, 32(1), 115–120.

Vaney, D. I., and Young, H. M. (1988). GABA-like immunoreactivity in cholinergic amacrine cells of the rabbit retina. Brain research, 438(1-2), 369–373.

Veruki, M. L., and Hartveit, E. (2002). AII (Rod) amacrine cells form a network of electrically coupled interneurons in the mammalian retina. Neuron, 33(6), 935–946.

von Gersdorff, H., and Matthews, G. (1997). Depletion and replenishment of vesicle pools at a ribbon-type synaptic terminal. J. Neurosci. 17(6), 1919–1927.

Wässle, H. (2004). Parallel processing in the mammalian retina. Nat Rev Neurosci 5, 747-757.

Werblin, F.S., and Dowling, J.E. (1969). Organization of the retina of the mudpuppy, Necturus maculosus. II. Intracellular recording. J. Neurophysiol. 32, 339-355.

Wei W. (2018). Neural Mechanisms of Motion Processing in the Mammalian Retina. Annual review of vision science, 4, 165–192.

Whitney, I.E., Keeley, P.W., St John, A.J., Kautzman, A.G., Kay, J.N., and Reese, B.E. (2014). Sox2 regulates cholinergic amacrine cell positioning and dendritic stratification in the retina. J Neurosci 34, 10109-10121.

Wurtz R. H. (1968). Visual cortex neurons: response to stimuli during rapid eye movements. Science, 162(3858), 1148–1150.

Wurtz R. H. (1969). Comparison of effects of eye movements and stimulus movements on striate cortex neurons of the monkey. Journal of neurophysiology, 32(6), 987–994.

Wurtz R. H. (1969). Response of striate cortex neurons to stimuli during rapid eye movements in the monkey. Journal of neurophysiology, 32(6), 975–986.

Yadav, S.C., Tetenborg, S., and Dedek, K. (2019). Gap Junctions in A8 Amacrine Cells Are Made of Connexin36 but Are Differently Regulated Than Gap Junctions in AII Amacrine Cells. Front Mol Neurosci 12, 99.

Yan , W., Laboulaye, M. A., Tran, N. M., Whitney, I. E., Benhar, I., and Sanes, J. R. (2020). Mouse Retinal Cell Atlas: Molecular Identification of over Sixty Amacrine Cell Types. J. Neurosci. 40(27), 5177–5195.

Yokoi, M., Mori, K., and Nakanishi, S. (1995). Refinement of odor molecule tuning by dendrodendritic synaptic inhibition in the olfactory bulb. Proceedings of the National Academy of Sciences of the United States of America, 92(8), 3371–3375.

Yoshida, K., Watanabe, D., Ishikane, H., Tachibana, M., Pastan, I., and Nakanishi, S. (2001). A key role of starburst amacrine cells in originating retinal directional selectivity and optokinetic eye movement. Neuron, 30(3), 771–780.Zeng, H., and Sanes, J.R. (2017). Neuronal cell-type classification: challenges, opportunities and the path forward. Nat Rev Neurosci 18, 530-546.

Zalutsky, R.A., and Miller, R.F. (1990). The physiology of substance P in the rabbit retina. J Neurosci 10, 394-402.

Zhang, J., & Slaughter, M. M. (1995). Preferential suppression of the ON pathway by GABAC receptors in the amphibian retina. Journal of neurophysiology, 74(4), 1583–1592.

Zhang, Y., Kim, I. J., Sanes, J. R., and Meister, M. (2012). The most numerous ganglion cell type of the mouse retina is a selective feature detector. Proceedings of the National Academy of Sciences of the United States of America, 109(36), E2391–E2398.

Zeng, H., & Sanes, J. R. (2017). Neuronal cell-type classification: challenges, opportunities and the path forward. Nature reviews. Neuroscience, 18(9), 530–546.

Zhu, Y., Xu, J., Hauswirth, W.W., and DeVries, S.H. (2014). Genetically Targeted Binary Labeling of Retinal Neurons. J. Neurosci. 34, 7845–7861.